NASA CR-
WRL 30410-19-F

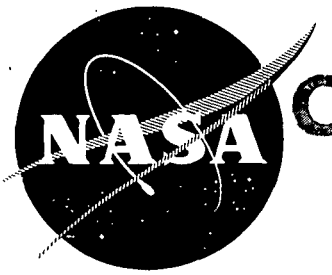

MEASUREMENT OF TEMPERATURE PROFILES IN FLAMES BY EMISSION-ABSORPTION SPECTROSCOPY

by

F. S. Simmons, C. B. Arnold, and G. H. Lindquist

INFRARED AND OPTICS LABORATORY
WILLOW RUN LABORATORIES
INSTITUTE OF SCIENCE AND TECHNOLOGY
THE UNIVERSITY OF MICHIGAN

February 1972

prepared for

NATIONAL AERONAUTICS AND SPACE ADMINISTRATION

NASA Lewis Research Center
Contract NAS 3-13037
D. R. Buchele, Project Manager

NOTICES

Sponsorship. The work reported herein was conducted by the Willow Run Laboratories of the Institute of Science and Technology for the National Aeronautics and Space Administration, Lewis Research Center, under Contract No. NAS 3-13037, with D. R. Buchele as Project Manager. Contracts and grants to The University of Michigan for the support of sponsored research are administered through the Office of the Vice-President for Research.

Availability Notice. Requests for copies of this report should be referred to:

National Aeronautics and Space Administration
Scientific and Technical Information Facility
P. O. Box 33
College Park, Md. 20740

NASA CR-
WRL 30410-19-F

FINAL REPORT

MEASUREMENT OF TEMPERATURE PROFILES IN FLAMES BY EMISSION-ABSORPTION SPECTROSCOPY

by

F. S. Simmons, C. B. Arnold, and G. H. Lindquist

INFRARED AND OPTICS LABORATORY
WILLOW RUN LABORATORIES
INSTITUTE OF SCIENCE AND TECHNOLOGY
THE UNIVERSITY OF MICHIGAN

prepared for

NATIONAL AERONAUTICS AND SPACE ADMINISTRATION

February 1972

Contract NAS 3-13037

NASA Lewis Research Center
Cleveland, Ohio
D. R. Buchele, Project Manager

FOREWORD

The research described herein was conducted by Willow Run Laboratories, a unit of The University of Michigan's Institute of Science and Technology, under Contract No. NAS 3-13037, sponsored by Lewis Research Center, National Aeronautics and Space Administration. Project Manager for this contract was D. R. Buchele. F. S. Simmons was Principal Investigator. This final report covers the period from June 1969 through April 1971. The Willow Run Laboratories' report number is 30410-19-F.

ACKNOWLEDGMENTS

Appreciation is expressed to Mrs. Carol Green Carrara for her efforts in the programming of the computer code for the isolated line radiances and to Mr. F. G. Smith for the modifications of the low-temperature band-model parameters.

ABSTRACT

An investigation was conducted to explore the use of infrared and ultraviolet emission-absorption spectroscopy for determination of temperature profiles in flames. Spectral radiances and absorptances were measured in the 2.7-μm H_2O band and the 3064-Å OH band in H_2/O_2 flames for several temperature profiles which were directly measured by a sodium line-reversal technique. The temperature profiles, determined by inversion of the infrared and ultraviolet spectra, showed an average disagreement with line-reversal measurements of 50°K for the infrared and 200°K for the ultraviolet at a temperature of 2600°K. The reasons for these discrepancies are discussed in some detail.

CONTENTS

FIGURES

TABLES

SYMBOLS

a	Ratio of Lorentz to Doppler half-width
A_1, A_2, A_3, A_4, A_5	Constants used in analytic form for η
B, D, A	Rotational constants for OH
c	Velocity of light
e	Electronic charge
E_e	Electronic energy
E_r	Rotational energy
E_v	Vibrational energy
$f_{J'J''}$	Oscillator strength
f(x)	Ladenburg-Reiche function
F	Function providing interpolation between nearly-weak and nearly-strong approximations
F'	Empirically determined constant
g_e	Statistical weight for electronic state
g_r	Statistical weight for rotational state
g_v	Statistical weight for vibrational state
$g(\nu' - \nu)$	Spectrometer slit function
J_0, J_1	Zero-th and 1st order Bessel functions
J, J', J''	Total angular momentum quantum number
K	Rotational quantum number when electron spin is neglected
k	Absorption coefficient
$\bar{k}$	Averaged absorption coefficient for band model
L	Integrated line radiance
L_ν	Spectral radiance (W/cm^2-sr-cm^{-1})
L^*_ν	Blackbody spectral radiance (W/cm^2-sr-cm^{-1})
$\bar{L}_\nu$	Spectral radiance computed with a band model
m	Electronic mass
N	Total number density of absorbing species (cm^{-3})
$N_{J''}$	Number density of the lower level (cm^{-3})
P	Pressure
Q_e	Electronic partition function
Q_r	Rotational partition function
Q_v	Vibrational partition function
r_c/R	Dimensionless core radius

$R_{J''J'}$	Relative magnitude of matrix element
S	Line strength
S_e	Equivalent line strength
T	Temperature
T_c	Core temperature
T*	Apparent temperature
$T_{J''J'}$	Vibration-rotation interaction factor
v	Vibrational quantum number
W	Equivalent width (cm^{-1})
x	Dimensionless optical depth for Curtis-Godson approximation
$\bar{x}$	Dimensionless optical depth for nearly-weak and nearly-strong approximation
$\bar{x}_L$	Dimensionless optical depth for entire path
X	Optical depth coordinate, $gm(cm^{-2})$
X_L	Optical depth for entire path, $gm(cm^{-2})$
α	Average spectral absorptance
β	Line-overlap parameter, $\frac{2\pi\gamma}{d}$
$\beta_e(x)$	Line-overlap parameter averaged over the path extending from the observer to optical depth **X**
β_{eL}	Line-overlap parameter averaged over the whole optical depth of interest
γ	Line width, cm^{-1}
$\gamma_e(x)$	Line width averaged over the path extending from the observer to optical depth **X**
γ_{eL}	Line width averaged over the whole optical depth of interest
δ	Average line spacing
ΔL_j	Geometrical path increment
ΔX_j	Optical depth increment
$\Delta\nu$	$\nu - \nu_o$ (cm^{-1})
η	Interpolation parameter between nearly-weak and nearly-strong approximation
κ	Boltzmann's constant
ν	Spectral frequency (cm^{-1})
ν_o	Line-center frequency (cm^{-1})
τ	Transmittance
$\bar{\tau}$	Average transmittance computed with a band model
$\bar{\tau}_n$	Average transmittance of equivalent nonoverlapping lines

MEASUREMENT OF TEMPERATURE PROFILES IN FLAMES BY EMISSION-ABSORPTION SPECTROSCOPY

SUMMARY

An experimental study was conducted to explore the use of infrared and ultraviolet emission-absorption spectroscopy in the 2.7-μm and 3064-Å bands of H_2O and OH respectively, for the determination of temperature profiles in nonuniform flames.

A rectangular multiple-diffusion burner with a number of unique features was designed and constructed for this study. A single manifold supplied oxidizer gas to the entire flame; the fuel manifold was divided into seven, isolated compartments. This permitted the establishment of temperature profiles along the length of the burner by throttling the fuel flow to each burner segment; thus, the local fuel/oxidizer ratio was varied. To color only the central portion of flame, a method was developed to introduce sodium into the fuel gas supplying the central portion of flame, thus permitting a direct determination of the temperature profile by line-reversal measurements.

A variation of the traditional line-reversal method was introduced for the temperature-profile measurement. The brightness temperature of a carbon arc was varied by an optical attenuator (designed and constructed for this purpose) consisting of a pair of counter-rotating, circular-disc, neutral density filters. With the attenuator set for the desired temperature, the line reversal was obtained by adjustment of the fuel-flow control valve, always keeping the mixture-ratio on the fuel-rich side of stoichiometric.

The burner was successfully operated with H_2/O_2, CH_4/O_2, and CO/O_2 as reactants. It was also operated in an isothermal mode, in which a central H_2/O_2 flame was shielded by CO/O_2 flames at either end to obviate the cooling and dilution of the combustion product, H_2O, mixing with ambient air. A 1.8-m Rowland circle spectrograph was converted into a scanning spectrometer by incorporation of an exit-slit assembly, which was designed and constructed for this study. A calibration procedure, which incorporated an NBS-certified tungsten lamp and a xenon arc, was developed for the reduction of the ultraviolet emission spectra into absolute spectral radiances.

Spectral radiances and absorptances were measured in the infrared and ultraviolet for four temperature profiles in H_2/O_2 flames: linear (viewed from either

direction); triangular, with a hot center; and triangular, with a cool center. The data are presented in complete detail, along with the sodium line-reversal temperatures.

The molecular band model used for the inversion of the infrared spectra was modified to handle more accurately nonisothermal radiation calculations for hot, gaseous sources exhibiting large gradients in temperature. The improved band model was checked by a comparison of predicted and measured values for a small, methane-oxygen flame viewed through 10 m of ambient air.

A computer code was written for use in inverting the OH spectra. It incorporated a parametric approach similar to that used for the infrared. However, instead of using a band model, the spectral radiances were calculated for isolated spectral lines by integrating the exact equation of transfer over both the optical path and the contour of the spectral line. An analysis was made to determine the relative importance of pressure and Doppler broadening; the results indicated that the former dominates for the optical depths encountered in this study.

The parametric method of inverting infrared emission and absorption spectra has been demonstrated in application to flames. Although the temperature profiles so determined showed disagreement with the profiles determined from the line-reversal observations, the disagreement is only nominal and the approach appears to be basically valid. In particular, the results indicate that a wide range of temperatures can be accommodated in such measurements. On the other hand, the parametric method of inverting ultraviolet emission and absorption spectra appeared, at least in this experiment, to be limited to providing information only over a narrow range of temperatures because of the steep variation of OH concentration with temperatures, especially in the region close to stoichiometric. Furthermore, the OH temperatures obtained were somewhat higher than the infrared and sodium line temperatures. This is tentatively attributed to OH chemiluminescence in and near the reaction zone. Further studies are required to delineate the regions and conditions in which OH chemiluminescence might be expected to affect emission absorption temperatures.

1

INTRODUCTION

In a previous investigation at this laboratory [1], infrared emission-absorption spectroscopy was studied as a means for determining temperature profiles in inhomogeneous hot gases, such as the exhaust jets of advanced air-breathing engines. A computer code, based on a generalized form of the statistical band model, was written for the calculation of molecular radiative transfer in diatomic and polyatomic gases. This code was applied to the determination of temperature profiles in hot gases by a procedure based on prior knowledge of the profile shape. This procedure involved the fitting of band-model predictions to observed spectra. For that previous study, spectral radiances and absorptances were measured in the 2- to 3-μm region for various pressures and temperature profiles along a 60-cm path in furnace-heated samples of H_2O, CO_2, HF, and H_2O, CO_2, N_2 mixtures. In all cases, the temperature profiles so obtained differed by an average value of 25°K from direct measurements by thermocouples on the sample cell.

In the present study, a continuation of this research, emission-absorption spectroscopy is applied to the determination of a higher temperature profile in an inhomogeneous flame to provide a more realistic simulation of actual applications. For this purpose, both infrared measurements in the 2.7-μm H_2O band and ultraviolet measurements in the 3064-Å OH band were investigated.

2

RADIATIVE-TRANSFER FORMULATIONS

2.1. BAND-MODEL

The band-model formulation used in this study is based on Eq. (5) of Ref. [2]; the rationale in the development of this model is reviewed in Ref. [1]. Expressed in terms of the average transmittance ($\bar{\tau}$) in a spectral bandpass encompassing a number of lines, the average spectral radiance at the observer from a given optical path ($\bar{L}_\nu$) is given in approximate form by

$$\bar{L}_\nu = \sum_{i=1}^{n} L_\nu^*(T_i)(\Delta\bar{\tau})_i \tag{1}$$

in which L_ν^* is the Planck function of the temperature, T_i. For this approximation, the optical path has been divided into n layers. The average spectral absorptance (α) of the optical path is given by

$$\alpha(\nu) = 1 - \sum_{i=1}^{n} (\Delta\bar{\tau})_i \tag{2}$$

where ν is the spectral frequency. The apparent (the indicated emission-absorption) temperature (T*) is given by

$$L_\nu^*(T^*) = \frac{\bar{L}_\nu}{\alpha(\nu)} \tag{3}$$

The spectral transmittance difference, $(\Delta\bar{\tau})_i = \bar{\tau}_{i-1} - \bar{\tau}_i$, for a single gas is obtained from $\bar{\tau}_i = \exp\left[-\beta_e f(\bar{x}_i)\right]$, where β is the line-overlap parameter, and for a mixture of m absorbing gases from the relation

$$\bar{\tau} = \prod_{k=1}^{m} \bar{\tau}_{i,k} .$$

The function f(x) is the Ladenburg-Reiche expression or a simple algebraic approximation of it [3]. The argument, $\bar{x}$, is the dimensionless optical depth, defined by

$$\bar{x}_i = \beta_e^{-1} \sum_{j=1}^{i} k(T_j)\left[\frac{\beta(T_j)}{\beta_e}\right]^{\eta} (\Delta X)_j \tag{4}$$

where $\bar{k}(T_j)$ = the local value of the first band-model parameter, the average absorption coefficient (which can be identified with the ratio of average line strength to spacing)

$\beta(T_j)$ = the local value of the second parameter (identifiable as the ratio of average line width to spacing and proportional to the effective broadening pressure)

β_e = the absorption-coefficient weighted average over the entire path

$(\Delta X)_j$ = the optical depth increment

The band-model parameters were extracted from the General Dynamics tabulations [4] and denormalized as indicated in [1].* The optical depth increment is given by $(\Delta X)_j = P_j(\Delta L)_j$, where P_j is the local value of the partial pressure of the radiating species and $(\Delta L)_j$ is the geometrical path increment. The exponent η provides for the interpolation between the nearly-weak and nearly-strong line approximations. For calculations which involve only hot gases and in which the temperature gradient is not too severe, the empirically derived specifications $\bar{x}_L < 1$, $\eta = 0$; $1 \le \bar{x}_L \le 10$, $\eta = (\bar{x}_L - 1)/9$; $\bar{x}_L > 10$, $\eta = 1$, where $\bar{x}_L$ is the optical depth for the entire path, are satisfactory. However, for calculations involving a large variation in temperature, a more complex interpolation procedure is necessary. Such a procedure has been developed and is described in Appendix I. In Appendix II, some comparisons of the band-model predictions with hot gas spectra are shown. A particular application, the calculation of net radiation from hot combustion products viewed through an absorbing atmospheric path, is described in Appendix III. These changes have improved the general performance of the band model [1]. Appendix IV includes a discussion of some adjustments of the band-model parameters for low temperatures.

2.2. ISOLATED LINES

Because of the simpler band structure of diatomic molecules, the rotational lines of OH were well separated and easily resolved by the instrumentation available. Therefore, like the infrared data for HF [1], the ultraviolet emission-absorption data could be handled on a line-by-line basis. However, approximate expressions for integrated line radiances and equivalent widths were avoided. Instead, these quantities were calculated using the exact equations of radiative transfer for a nonscattering source in local thermodynamic equilibrium:

$$L_\nu = \int_0^{X_L} L_\nu^*(X)\, k(\nu, X) \exp\left[- \int_0^X k(\nu, x')\, dX' \right] dX \qquad (5)$$

*In Appendix C, p. 92 of [1], the denormalization factor should read [273/T], not $\sqrt{273/T}$.

and

$$\alpha(\nu) = 1 - \exp\left[-\int_0^{X_L} k(\nu, X)\, dX\right] \tag{5a}$$

where k = the absorption coefficient
X = the optical depth coordinate

The integrated radiance and equivalent width are defined by

$$L = \int_0^{\infty} L_\nu \, d\nu \tag{6}$$

and

$$W = \int_0^{\infty} \alpha(\nu)\, d\nu \tag{7}$$

respectively, and the apparent temperature by

$$L_\nu^*(T^*) = \frac{L}{W} \tag{8}$$

where W = the equivalent width. Equations (5) through (8) were programmed for numerical computations on The University of Michigan's IBM 360 system. These equations require that transition probabilities or oscillator strengths be transformed into the form of the line strengths used in the infrared.

The 3064-Å OH band results from transitions between the $^2\pi^-$ (lower) and the $^2\Sigma^+$ (upper) electronic states. The transitions in this band near 3064 Å correspond to the $v' = v'' = 0$ band, where single and double primes indicate upper and lower levels specified by the vibrational quantum number, v. The rotational structure of this band has been described by Dieke and Crosswhite [6]. The line strength (S) for a particular line within the 3064-Å band is given by

$$S_{J''J'} = \int_0^{\infty} k(\nu)\, d\nu \tag{9}$$

where k is the spectral absorption coefficient of Eq. (5) in $cm^{-1}\ atm^{-1}$, and ν is the wave number in cm^{-1}. The dependence upon the path has been suppressed. J' and J'' indicate the total angular momentum quantum numbers of the upper and lower rota-

tional states. The line strength is related to the oscillator strength $f_{J''J'}$ by [7]:

$$S_{J''J'} = f_{J''J'} N_{J''} \frac{\pi e^2}{mc^2} \tag{10}$$

where $N_{J''}$ is the population of the lower level in cm^{-3}; m and e are the electronic mass and charge; and c is the velocity of light. Because of the small population of the upper state, contributions to the line strength from emission by molecules in the upper state are neglected in this definition. The oscillator strength and rotational matrix element are related by

$$f_{J''J'} = \frac{F' T_{J''J'} R_{J''J'}}{(2J'' + 1)} \tag{11}$$

where $R_{J''J'}$ is the relative magnitude of the matrix element, F' is an empirically determined constant, and $T_{J''J'}$ is a vibration-rotation interaction factor. For the tabulations of $R_{J''J'}$ of Dieke and Crosswhite [6], a value of 2.0×10^{-4} for F' was determined by Golden et al. [7], and values of $T_{J''J'}$ were computed by Learner [8]. A combination of Eqs. (10) and (11) yields

$$S_{J''J'} = \frac{T_{J''J'} R_{J''J'} N_{J''}}{(2J'' + 1)N} \left(\frac{F' \pi e^2 N}{mc^2} \right) \tag{12}$$

where N is the total number density of OH molecules. With the prime notation omitted for convenience, the population factor N_J/N is expressed by the product

$$\frac{N_J}{N} = \left(\frac{g_e}{Q_e} e^{-E_e/\kappa T} \right) \left(\frac{g_v}{Q_v} e^{-E_v/\kappa T} \right) \left(\frac{g_r}{Q_r} e^{-E_r/\kappa T} \right) \tag{13}$$

where E_e, E_v, E_r are the energies for the electronic, vibrational, and rotational states respectively; g_e, g_v, g_r are the corresponding statistical weights; and Q_e, Q_v, Q_r are the electronic, vibrational, and rotational partition functions. The term in Eq. (13) corresponding to the electronic state is essentially unity for all temperatures of interest here.

The vibrational energy levels were computed from the relation

$$E_v(v) = \omega(v + 1/2) - x(v + 1/2)^2 \tag{14}$$

where $\omega = 3735.21\ cm^{-1}$ and $x = 82.21\ cm^{-1}$ [6]. The partition function, Q_v, was computed by a summing of the exponential factors, $\exp[-E_v(v)/\kappa T]$ over v until convergence was obtained. Less than 10 terms were needed for convergence at 3000°K.

The rotational state of an OH molecule is not specified until both K, essentially the rotational quantum number when electron spin is neglected, and J, the total angular momentum ($J = K \pm 1/2$), are specified. Since in this study, only the R_2 branch of the 0-0 band of the $^2\pi$ to $^2\Sigma$ transition is considered, by the Dieke and Crosswhite convention, the relative population of molecules in the "2" state must be computed; that is, those molecules having not only a given value of K but a value of $J = K - 1/2$ as well. (In Dieke and Crosswhite, the line is designated by its K value; hence the $R_2 1$ line has $J = 1/2$, $K = 1$.) Reference [6] gives expressions for the rotational energies of the "1" and "2" state of the lower ($^2\pi$) electronic state as follows:

$$E_{r_1}(K) = B\left\{(K+1)^2 - 1 - \frac{1}{2}\sqrt{4(K+1)^2 + A(A-4)}\right\} - DK^2(K+1)^2$$

"1" state ($J = K + 1/2$)

(15)

$$E_{r_2}(K) = B\left\{K^2 - 1 + \frac{1}{2}\sqrt{4K^2 + A(A-4)}\right\} - DK^2(K+1)^2$$

"2" state ($J = K - 1/2$)

These expressions were used to compute the rotational energies with the following values for the rotational constants (B, D, A) appearing in Equation (15) [6]:

$$B = 18.515\ cm^{-1}$$
$$D = 0.00187\ cm^{-1}$$
$$A = -7.547$$

The statistical weight is $2J + 1$ for either of the two rotational states which corresponds to a given value of J. The rotational partition function was computed by evaluation of the following sum:

$$Q_r = \sum_{K=0}^{K_{max}} \left\{(2K+2)\exp\left[\frac{-E_{r_1}(K)}{\kappa T}\right] + 2K\exp\left[\frac{-E_{r_2}(K)}{\kappa T}\right]\right\} \qquad (16)$$

where κ is Boltzman's constant. The sum was continued until convergence occurred

(i.e., to about $K_{max} = 40$). For $K > 100$, the expressions for the rotational energy Equation (15) began to diverge; however, convergence of the sum in Equation (16) was obtained much before this occurred. Line strengths computed from Equations (12-16) for several lines at various temperatures are shown in Table 1.

Line widths (γ) for OH were taken from the recent work of Nadler and Kaskan [9]. Their results are presented in terms of the ratio of Lorentz to Doppler half-width, $a = \sqrt{\ell n 2}\,\gamma_L/\gamma_D$; typical values are shown in Table 2 for a pressure of one atmosphere and a temperature of 1485°K. In all cases, $a > 0.2$ so that, in accordance with the analysis by Yamada [10], the curve of growth of a Voigt line is indistinguishable from that of a Lorentz line over the entire range of optical depths. Hence, Lorentz line half-widths can be computed from values of a in Table 1 and adjusted to the local temperature and pressure, in accordance with the billiard-ball approximation for collision broadening:

$$\gamma_L(P, T) = \gamma_{L,o}\,\frac{P}{P_o}\,\sqrt{\frac{T_o}{T}} \tag{17}$$

where $P_o = 1$ atm, and $T_o = 1485°K$. Table 1 lists values of γ_L for a number of lines at various temperatures. The values of a determined by Nadler and Kaskan are questionable. Their work shows a sharp increase in a for large J values which is difficult to justify physically. On another contract, Anderson's theory was used to make calculations of the line width of another diatomic molecule, HF, which has a similar rotational constant, B. The results indicate that, if anything, the line widths would be expected to decrease with increasing J value and, at high temperatures, would tend to uniformity over J. Moreover, there is a large amount of scatter in the results of Nadler and Kaskan, and their broadening gas ($N_2 + H_2O$) was not the same as that of the present experiment (H_2O). These factors indicate that a uniform value of a between 0.3 and 0.5 corresponding to 1485°K for all lines might be more realistic for these experiments than the values given in Table 2.

It is possible to determine a rotational temperature of the lower state from the rotational structure of the absorption spectrum from an isothermal flame. In this procedure, the equivalent width of a single isolated line is given by

$$W = 2\pi\gamma f\left(\frac{S_{J''J'}\,X}{2\pi\gamma}\right) \tag{18}$$

where W is the equivalent width of the line having strength $S_{J''J'}$, and half-width γ, and f is again the Ladenburg-Reiche function. X is the physical optical depth, P(OH) x l

TABLE 1. STRENGTHS AND LORENTZ HALF-WIDTHS* OF SEVERAL OH LINES

Line	ν_0 cm^{-1}	Strength (cm^{-2} atm^{-1}) 1600	2000	2400	2800K	Half Width [10] (cm^{-1} atm^{-1}) 1600	2000	2400	2800K
$R_2 1$	32415.51	90.9	71.2	57.3	47.0	0.060	0.054	0.049	0.045
$R_2 3$	32489.49	257.0	207.0	170.0	141.0	0.045	0.040	0.037	0.034
$R_2 4$	32517.58	324.0	268.0	223.0	183.0	0.040	0.036	0.033	0.030
$R_2 7$	32572.59	324.0	317.0	286.0	254.0	0.040	0.036	0.033	0.030
$R_2 14$	32551.72	55.0	84.0	105.3	118.7	0.057	0.051	0.047	0.043
$R_2 15$	32531.76	36.0	60.4	80.8	95.3	0.057	0.051	0.047	0.043
$R_2 20$	32363.49	2.63	7.72	15.0	23.0	0.095	0.085	0.078	0.072

* OH broadened by $H_2O + N_2$

TABLE 2. RATIO OF LORENTZ AND DOPPLER HALF-WIDTHS FOR SEVERAL OH LINES AT ONE ATMOSPHERE AND 1485°K [10]

Line	A
$R_2 1$	0.50
$R_2 3$	0.37
$R_2 4$	0.33
$R_2 7$	0.32
$R_2 14$	0.46
$R_2 15$	0.46
$R_2 20$	0.70

where P(OH) is the partial pressure of OH, and l is the path length in cm reduced to standard temperature and pressure. The line strength $S_{J''J'}$ is a function of the rotational quantum number of the lower state, J'', as given by Equations (12-16). $S_{J''J'}$ can be expressed in the following form, in which the J dependence of $S_{J''J'}$ appears explicitly, but the temperature variation of S is combined into one common factor, K(T):

$$S_{J''J'} = K(T) \cdot T_{J''J'} R_{J''J'} \exp\left(\frac{-E_r(J'')}{\kappa T}\right) \tag{19}$$

After substitution of this expression into Eq. (18) and after the inverse Ladenburg-Reiche function and the natural logarithm of both sides are taken, the following expression is obtained:

$$\ell n \left\{ \frac{f^{-1}\left(\frac{W}{2\pi\gamma}\right) \cdot 2\pi\gamma}{T_{J''J'} R_{J''J'}} \right\} - \ell n \left[K(T) \cdot X \right] = \frac{-E_r(J'')}{\kappa T} \tag{20}$$

In a given measurement, $\ell n [K(T) \cdot X]$ is a constant for all the rotational lines in a band. Thus, if the first term on the left is plotted versus $-E_r(J'')/\kappa$ for a number of rotational lines, the result should be a straight line the slope of which is 1/T where T is a rotational temperature characterizing the distribution of rotational states in the lower electronic state. In general, if this technique is to be applied, values for the line half-widths are required, and these are not accurately known. If the lines, as observed, are optically thin (in the region of linear growth), then the function $f^{-1}(W/2\pi\gamma)2\pi\gamma$ reduces simply to W and the line half-width no longer appears. Unfortunately, in these experiments, the lines were never in the linear growth region.

3

EXPERIMENTAL ARRANGEMENTS

3.1. BURNER CONFIGURATION

The nonisothermal flames studied in this program were created with a seven-section multiple diffusion burner schematically illustrated in Fig. 1. The operation of this burner was similar in principle to one used in previous studies of HF flames [11]. The fuel gas passed through a set of copper tubes from seven compartments in the manifold; the flow into each was controlled by a separate valve. The oxidizer gas flowed between the tubes from a single manifold. Combustion occurred above the tube-end surface in a multiplicity of small diffusion flames; the combustion products rapidly mixed to approximate conditions of a premixed flame. The temperature profiles were created by a throttling of the fuel gas entering each compartment. This caused a variation in the fuel-oxidizer ratio of the combustion above that segment. The controls were set to produce a desired temperature profile, as indicated by the sodium line-reversal temperature measurement described below. The top and side surfaces of the burner were cooled by water flowing through tubes of rectangular cross-section, which were soldered in place.

The burner was constructed so that sodium could be introduced into the fuel gas flowing through the central tube in each segment (see Fig. 2). A line from the burner compartment passed fuel gas through the sodium vaporizer, then back to the compartment into the central tube of that segment of the burner. The vaporizer consisted of an electrically heated graphite boat containing a charge of sodium iodide. When the current through the boat stabilized, sodium-iodide smoke could be produced at a constant rate and would be picked up by the flowing fuel gas. Thus, each segment of the burner could be individually colored by sodium for the line-reversal measurements which were used to set the temperature profiles.

3.2. INFRARED INSTRUMENTATION

The seven-segment burner was installed in the sample beam of a double-beam, infrared spectrometer shown schematically in Fig. 3. The configuration and operation of this spectrometer were described in detail previously [1]. However, a change in the intensity calibration procedure was introduced in the present study. A separate blackbody was placed in the sample beam so that the effective infrared radiance temperature of the blackbody built into the spectrometer could be directly determined. Thus, the differences in mirror reflectances between 0.65 μm, the effective wavelength of the optical pyrometer previously used for calibration, and 2.7 μm, the wavelength of the infrared measurements, were completely accounted for. In a series of

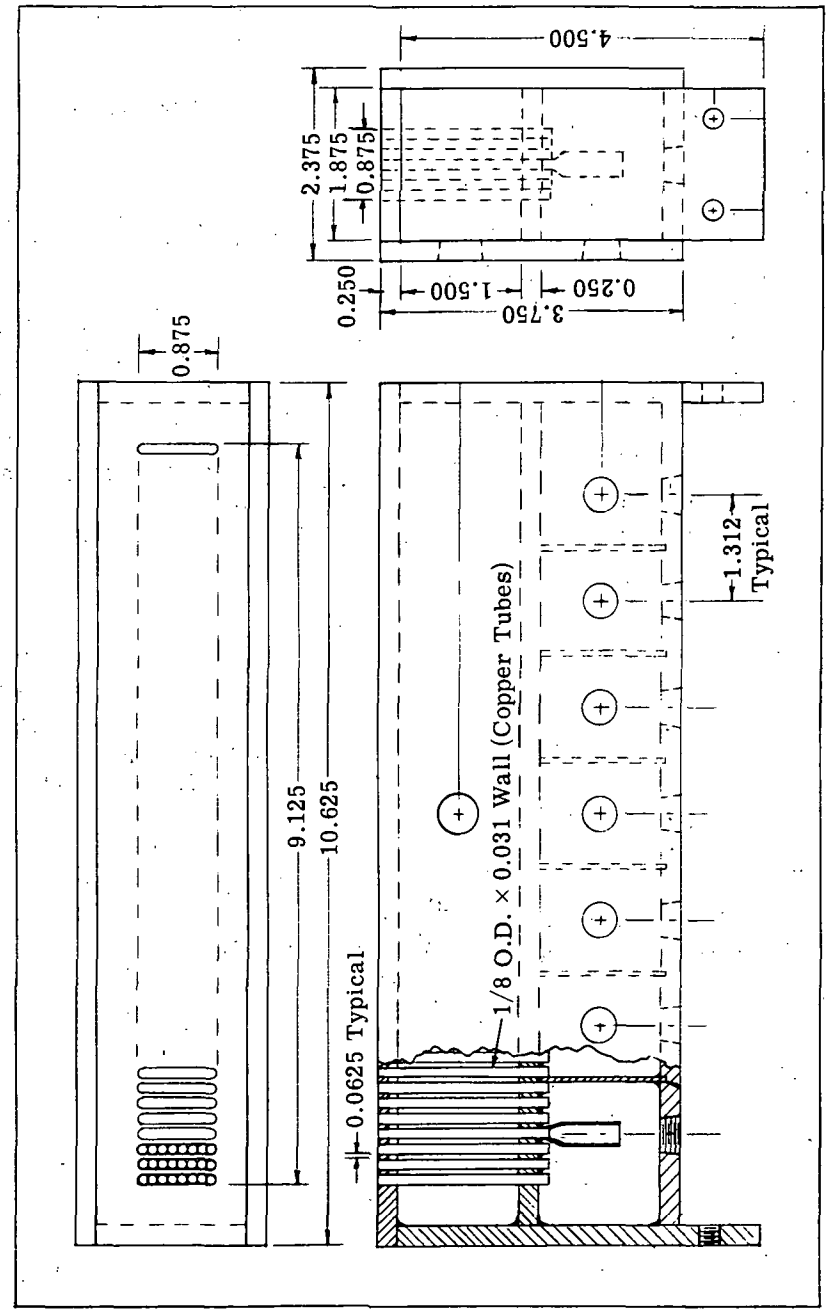

FIGURE 1. SEVEN-SECTION, RECTANGULAR MULTIPLE-DIFFUSION BURNER

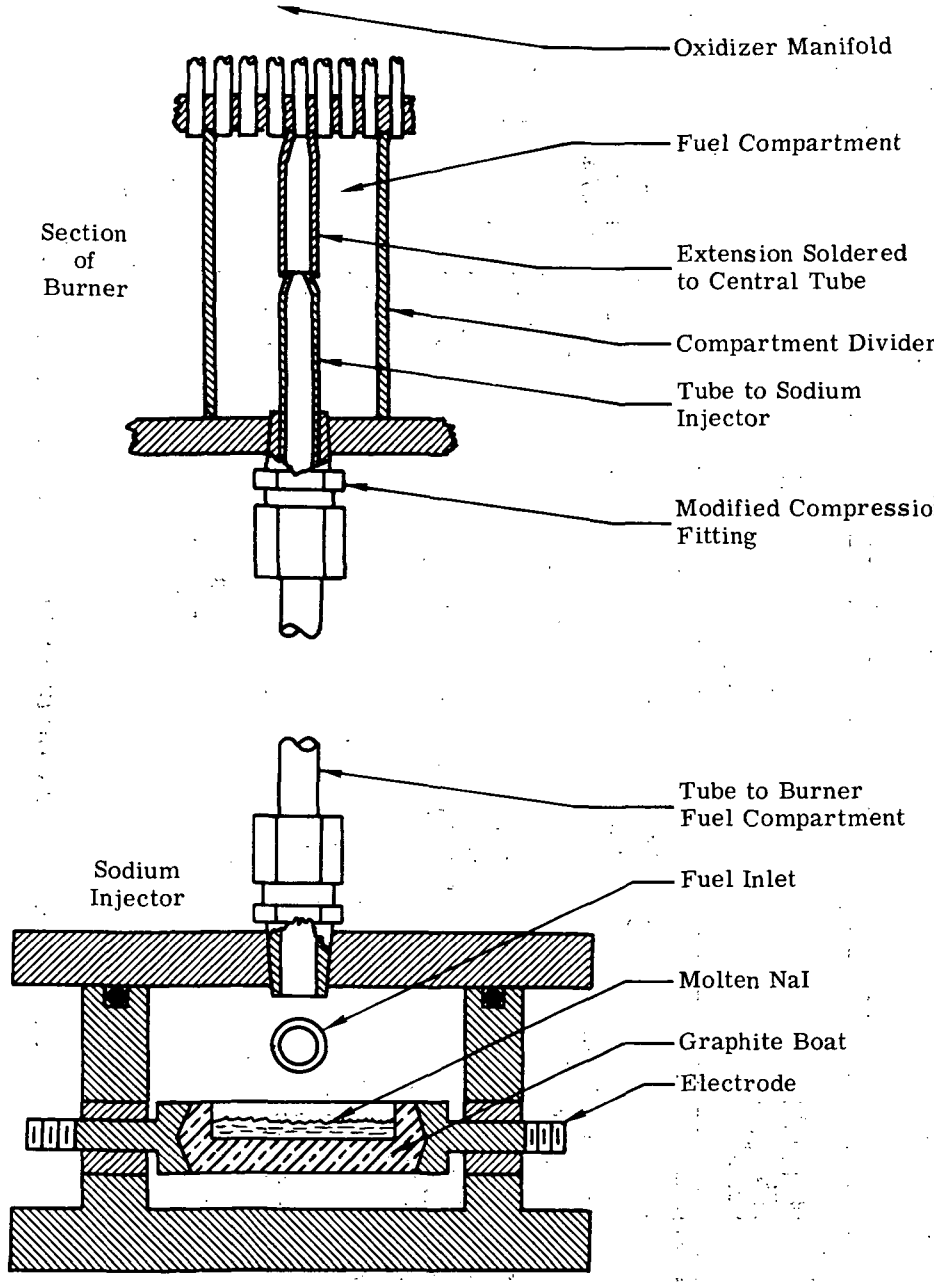

FIGURE 2. SODIUM-INJECTION SCHEME

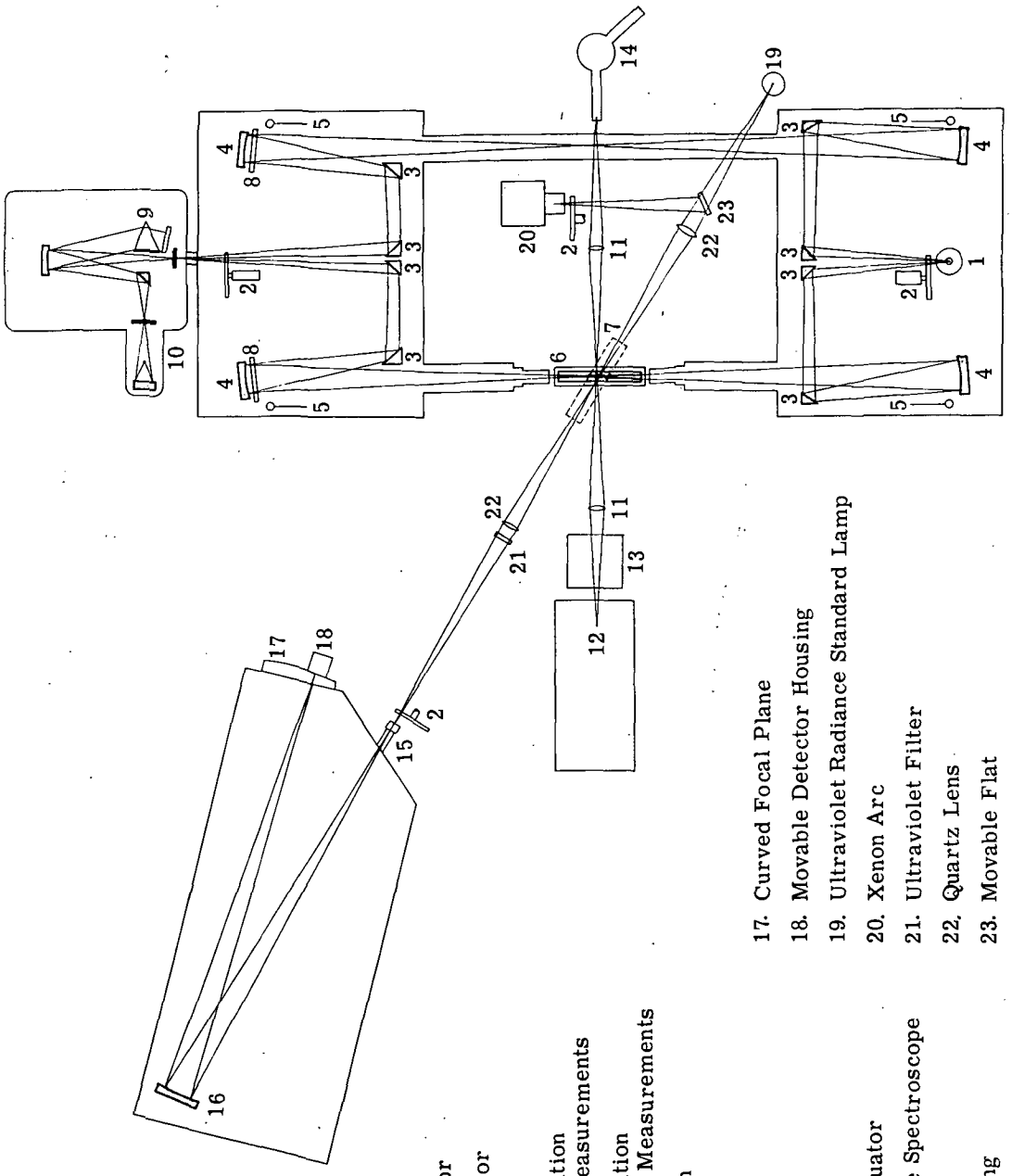

1. Blackbody
2. Chopper
3. Diagonal Mirror
4. Spherical Mirror
5. Shutter
6. Burner in Position for Infrared Measurements
7. Burner in Position for Ultraviolet Measurements
8. Iris Diaphragm
9. LiF Prism
10. PbS Detector
11. Glass Lens
12. Carbon Arc
13. Variable Attenuator
14. Divided-Circle Spectroscope
15. Entrance Slit
16. Concave Grating
17. Curved Focal Plane
18. Movable Detector Housing
19. Ultraviolet Radiance Standard Lamp
20. Xenon Arc
21. Ultraviolet Filter
22. Quartz Lens
23. Movable Flat

FIGURE 3. EXPERIMENTAL ARRANGEMENT

measurements, the optical pyrometer was used to measure the temperature of the external blackbody and to monitor the internal blackbody.

3.3. ULTRAVIOLET INSTRUMENTATION

The ultraviolet measurements were made with a 1.5-m Rowland circle spectrograph constructed some years ago at The University of Michigan's Physics Department. The grating (an original, ruled by Rowland about 40 years ago) had a ruled area 90 × 55 mm in size with 400 grooves/mm. The photographic plate holder was replaced by a movable exit-slit assembly constructed for this study, and a 1P28A photomultiplier tube was used as the detector. The grating was blazed for wavelengths in the visible; accordingly, the measurements of the 3064-Å OH band were made in the second order.

For the emission measurements, a 90 Hz chopper was positioned in front of the entrance slit; a Princeton Applied Research Model HR-8 Lock-in amplifier was used to amplify and rectify the photomultiplier signal for display on the strip-chart recorder. The intensity calibration was made with a National Bureau of Standards radiance standard lamp positioned on the far side of the flame. The tungsten ribbon filament was imaged in the center of the flame and reimaged onto the spectrometer entrance slit by a pair of 250-mm focal-length fused quartz lenses. A Corning #9863 filter was used to eliminate the visible radiation from the standard lamp; the elimination was complete to within the noise level of the resultant measurements, as verified by temporary placement of an ultraviolet absorbing filter in the beam. Thus, the calibration procedure required only one correction factor to account for the reflection losses of the quartz lens behind the flame.

The measurements of spectral absorptance were made with a 150-W xenon-arc source, chopped at a frequency of 2040 Hz and positioned behind the flame. The higher chopping frequency was necessary to discriminate against fluctuations in the flame which generally exhibit an amplitude varying inversely with frequency [12].

3.4. SODIUM LINE-REVERSAL INSTRUMENTATION

Sodium line-reversal temperatures were measured transverse to the longer dimension of the burner by the apparatus shown in Fig. 3. A Mole-Richardson Type 2371 carbon arc was used for the reference source. The arc crater was imaged in the center of the flame and reimaged onto the slit of a divided-circle spectroscope by a pair of lenses. The apparent brightness temperature of the arc source could be continuously varied by an attenuator consisting of a pair of counter rotating, circular disc, neutral density filters calibrated by means of an optical pyrometer.

The temperature profile along the length of the burner was established by the segment-by-segment sodium line-reversal measurements made in the transverse direction. First, the attenuator was set to the desired brightness temperature; then the fuel-flow rate was adjusted (on the fuel-rich side of stoichiometric) until the line reversal was observed.

Unfortunately, the rectangular cross-section cooling tubes on the top of the burner required the transverse line-reversal measurements to be made with the mean height of the optical beam approximately 1 cm above the burner-tube ends. Consequently, the radial diffusion of the sodium from the central tube reached the mixing region of the flame gases with the ambient air at about the height of the optical beam (see Fig. 4). To correct the resultant error caused by absorption in the cooler mixing region, a set of line-reversal measurements were made at various fuel-air ratios, viewing the sodium-colored segment of the burner in both the transverse and longitudinal directions. In the latter case, of course, the uncolored adjacent segments, set at the same temperature, shielded the central segment. Thus, a correction was obtained for the transverse line-reversal measurements with which the temperature profiles along the burner were set; the magnitude of this correction is shown in Fig. 5.

The experiments proceeded in the following sequence. A temperature profile was created and measured by the line-reversal observations. A complete set of infrared and ultraviolet emission, absorption, and calibration spectra were then obtained with the individual fuel-line valves remaining at their set positions. Between scans, the burner was shut off by the two main flow valves, which were always set in the full-open position during burning. Thus, there was no problem in reproducing identical profiles for the emission and absorption scans within a set.

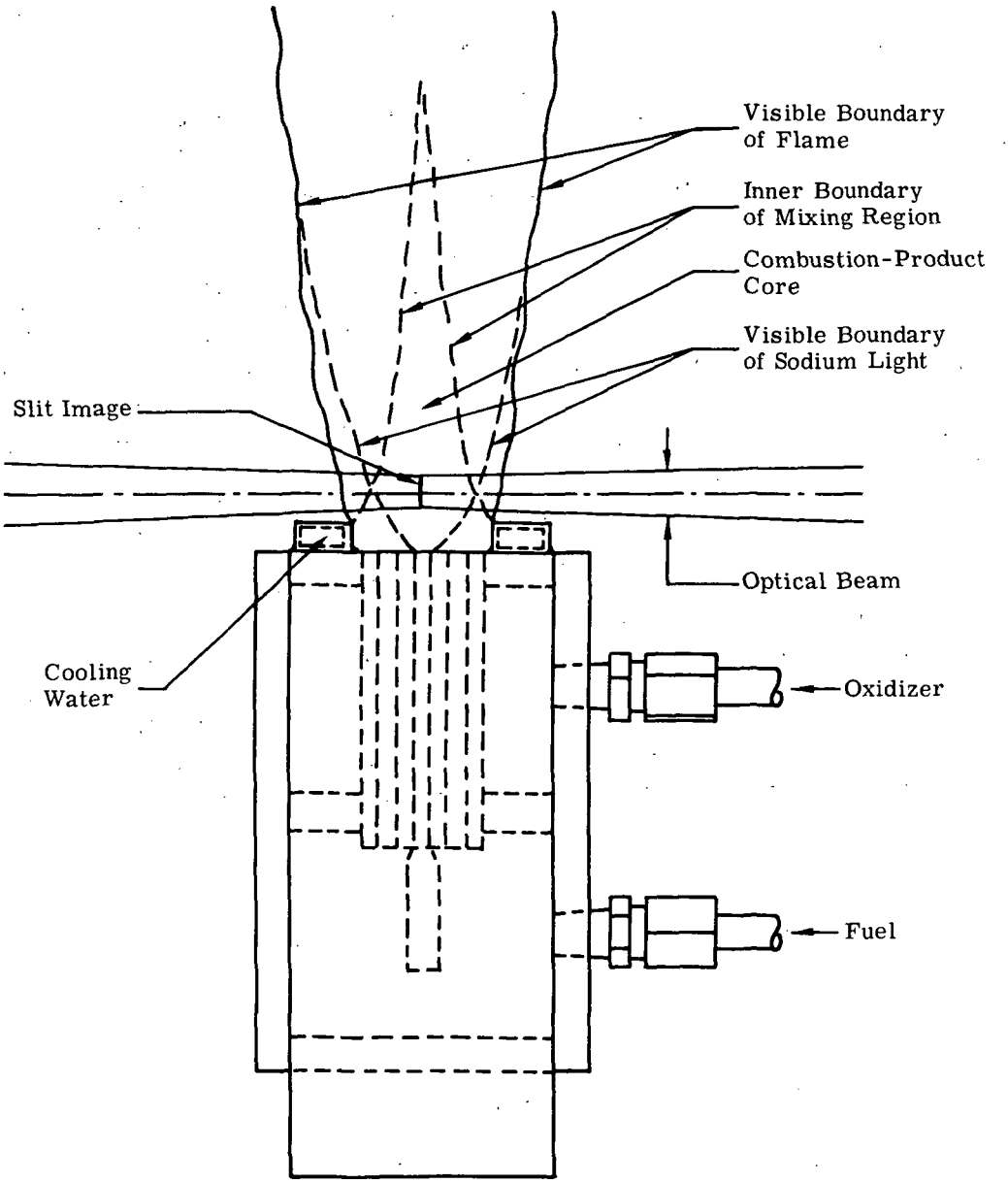

FIGURE 4. DIFFUSION OF SODIUM IN FLAME

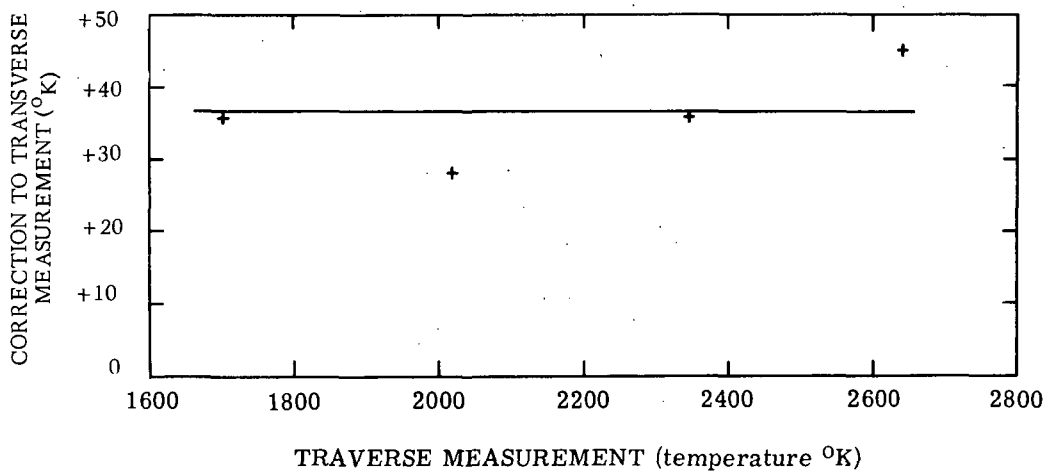

FIGURE 5. CORRECTION FOR LINE-REVERSAL MEASUREMENTS

4

EXPERIMENTAL DATA

4.1. INFRARED SPECTRA

As in the previous study, the infrared spectra were recorded both on a chart and on cards for automatic reduction; for the latter, the sampling rate during scanning was sufficient to provide excellent fidelity of the reduced spectra to the chart recording. Data were obtained in this way for five settings of the burner for hydrogen-oxygen combustion. Linear profiles were created with the high- (profile A) and low- (profile B) temperature ends toward the monochromator. (Actually, a single profile was created, and the burner rotated 180^{o}.) Symmetrical triangular profiles were set with high- (profile C) and low- (profile D) temperatures at the center segment. Finally, for a system operation check, an isothermal flame was produced (profile E) by adjusting the interior segments of the burner to a constant temperature, using H_2 and O_2, while the segments on each end were set to the same indicated temperature using CO and O_2. Thus, the nonisothermal mixing region was eliminated for observations in the 2.7-μm region outside the CO_2 band, but within the H_2O bands. The reduced spectra for the nonisothermal runs (radiance, absorptance, and apparent temperature) are presented in Figs. 6 through 9; the reduced spectra for the isothermal run with the shielded flame are presented in Fig. 10. The corresponding line-reversal temperatures are shown in Figs. 11 through 14; the burner segment designated 1 is closest to the monochromator.

In the isothermal case, the apparent temperature, T*, should correspond to an actual flame temperature and be independent of wavelength. Figure 10 shows this to be the case except in the region of the 2.7-μm CO_2 band where mixing-region effects are noted, and at the extreme wavelengths, where measurement errors become large. Ignoring these regions, the resultant average apparent temperature of $2630^{o}K$ agrees with the corrected sodium line-reversal temperature, $2600^{o}K$, at which the flame was set (Fig. 15) to within the overall experimental uncertainty. The source of the spectral noise in the trace of apparent temperature for the isothermal case (Fig. 10) was not determined; presumably, it is the consequence of imperfect register between the emission and absorption spectra in the data reduction.

The burner was also operated with methane and carbon monoxide as fuels. For CH_4/O_2 operation, data were recorded and reduced; however, the quality of the results was lessened by a subsequent discovery of a procedural error in the setting of the flow rates, and circumstances did not permit repetition of these runs. For CO/O_2 operation, the much lower flame speed caused the flames to lift off the burner at comparable flow rates. For the flame to seat on the burner, a very low flow rate was required, and the small flame height did not adequately accommodate the optical beam. No data were recorded for this case.

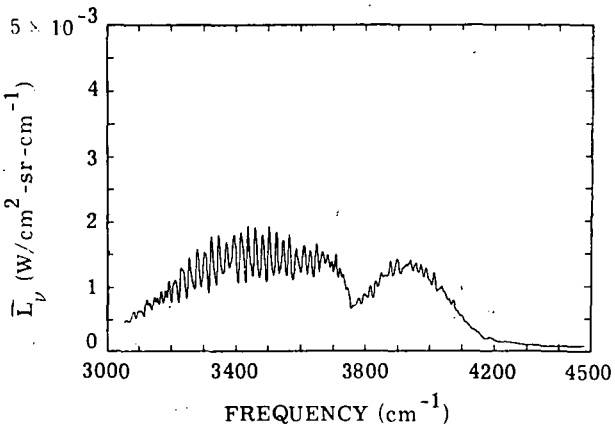

(a) Spectral Radiance

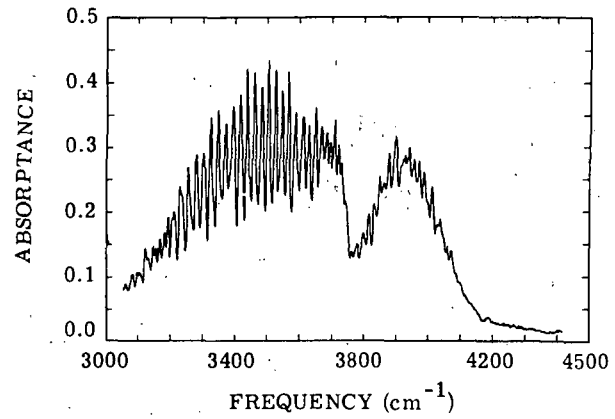

(b) Spectral Absorptance

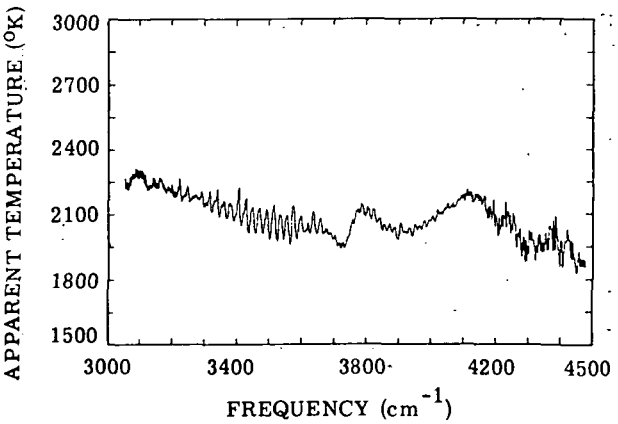

(c) Apparent Temperature

FIGURE 6. REDUCED DATA, PROFILE A: LINEAR (HOT THROUGH COLD)

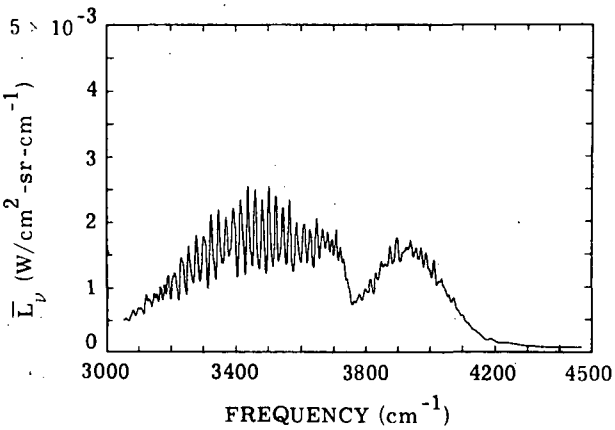

(a) Spectral Radiance

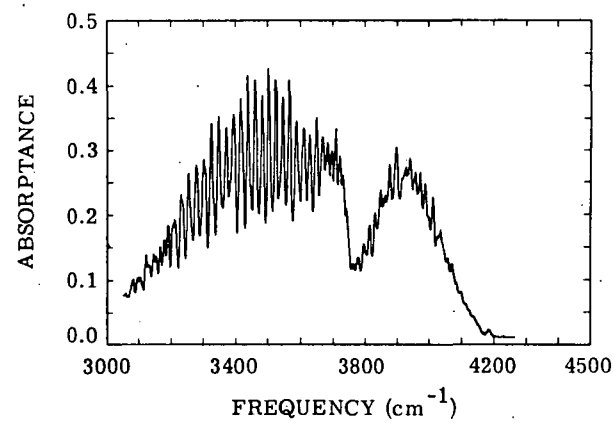

(b) Spectral Absorptance

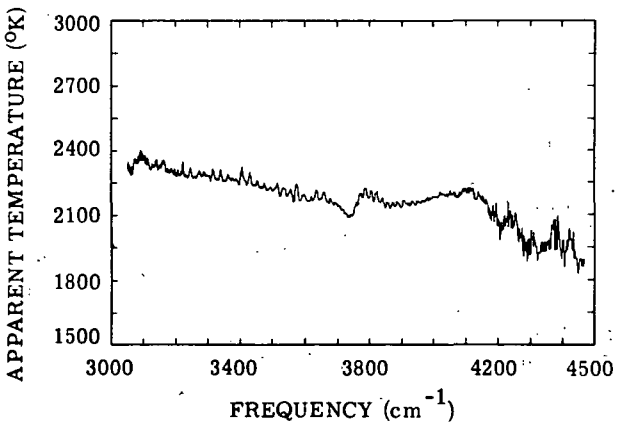

(c) Apparent Temperature

FIGURE 7. REDUCED DATA, PROFILE B: LINEAR (COLD THROUGH HOT)

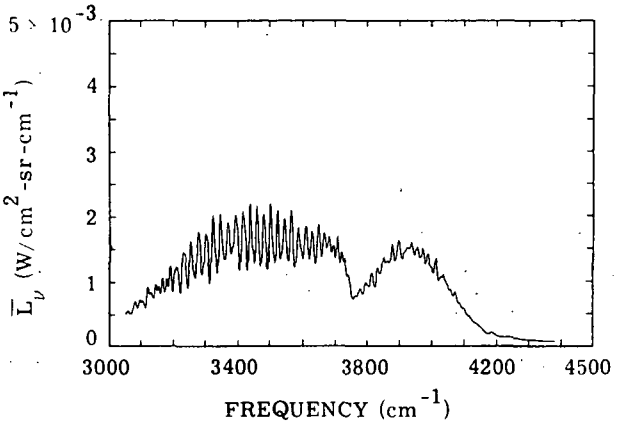

(a) Spectral Radiance

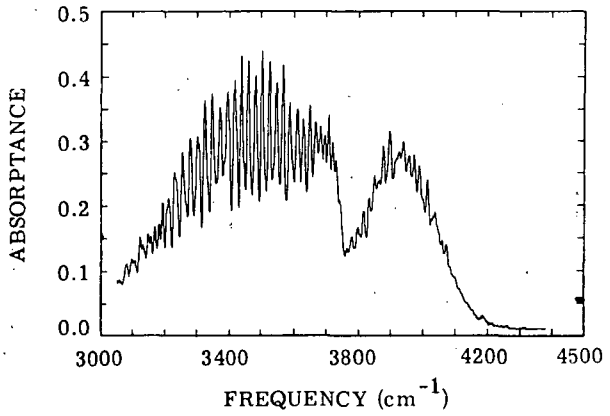

(b) Spectral Absorptance

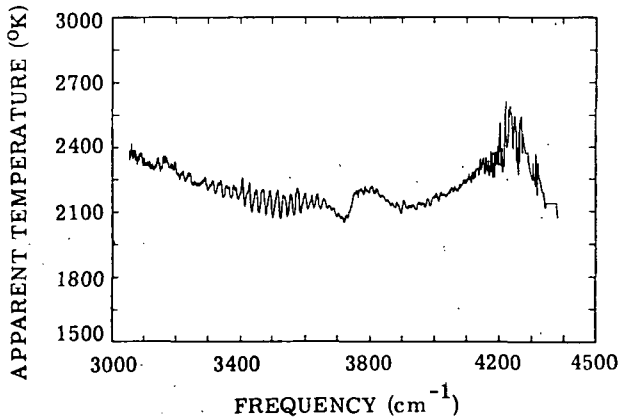

(c) Apparent Temperature

FIGURE 8. REDUCED DATA, PROFILE C: TRIANGULAR (HOT CENTER)

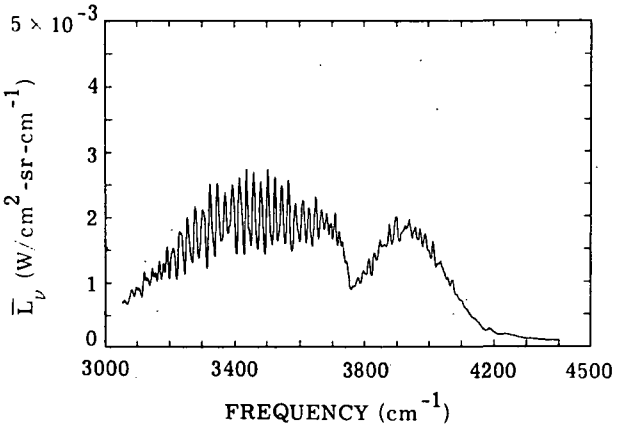

a. Spectral Radiance

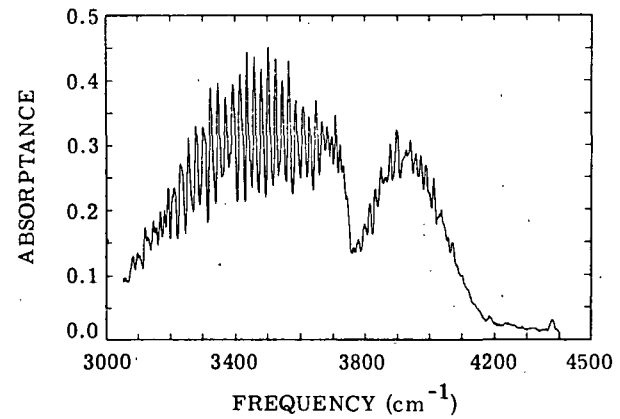

b. Spectral Absorptance

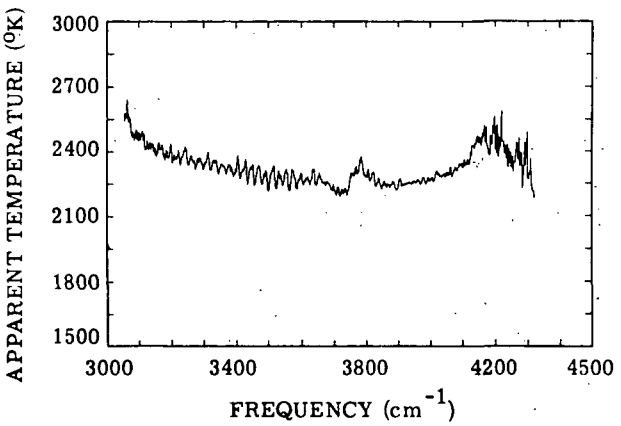

c. Apparent Temperature

FIGURE 9. REDUCED DATA, PROFILE D: TRIANGULAR (COLD CENTER)

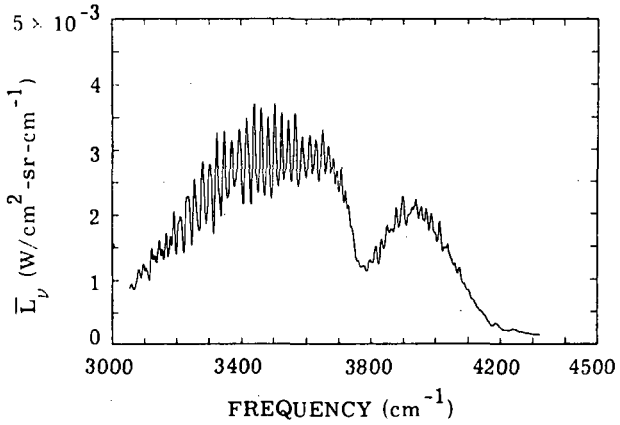

(a) Spectral Radiance

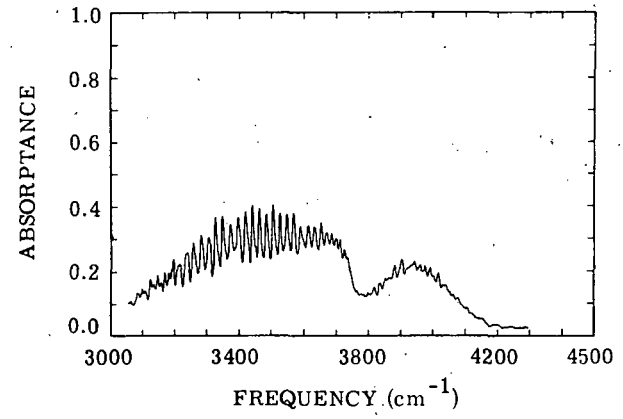

(b) Spectral Absorptance

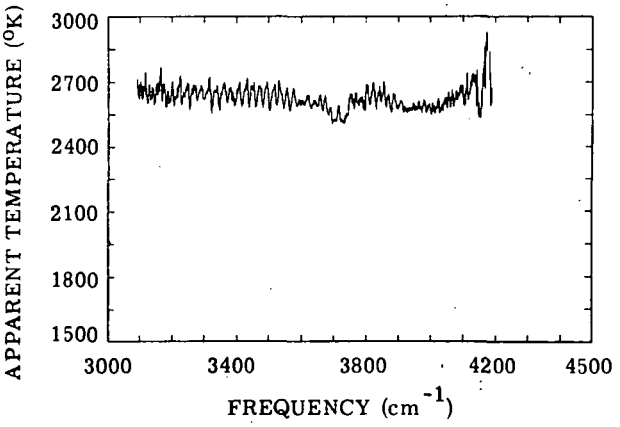

(c) Apparent Temperature

FIGURE 10. REDUCED DATA, PROFILE E: ISOTHERMAL

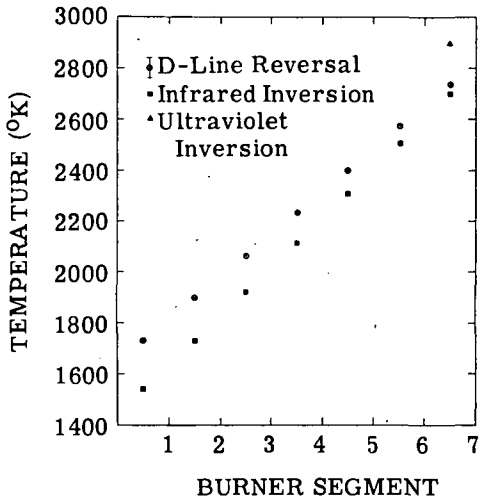

FIGURE 11. TEMPERATURES, PROFILE A, LINEAR (HOT THROUGH COLD) IN H_2/O_2 FLAME

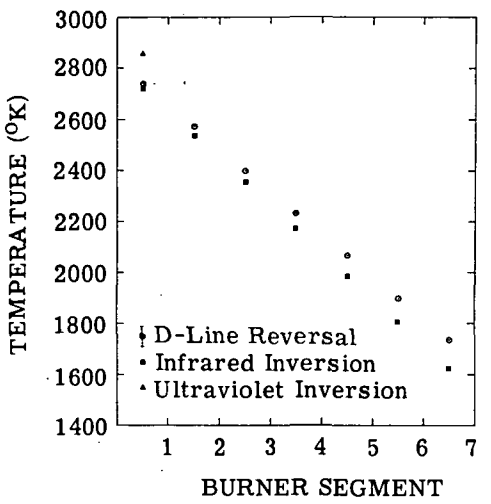

FIGURE 12. TEMPERATURES, PROFILE B, LINEAR (COLD THROUGH HOT) IN H_2/O_2 FLAME

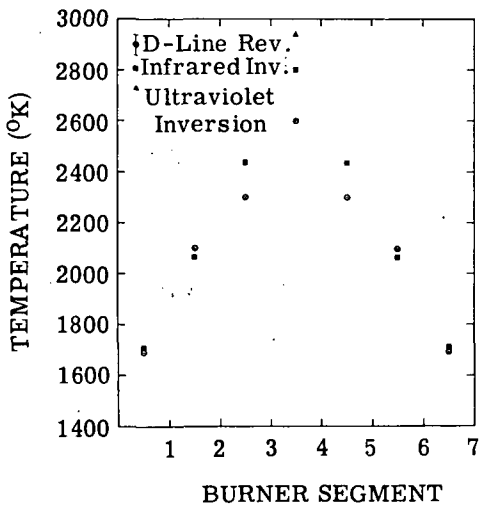

FIGURE 13. TEMPERATURES, PROFILE C, TRIANGULAR (HOT CENTER) IN H_2/O_2 FLAME

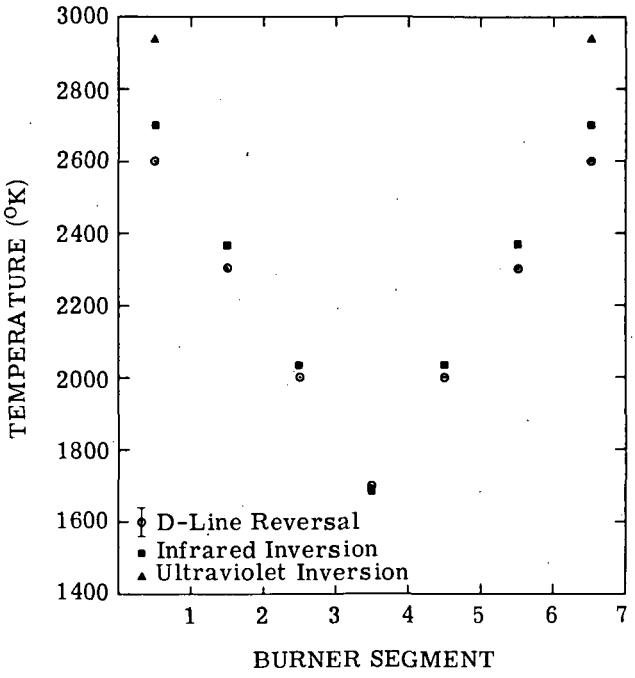

FIGURE 14. TEMPERATURES, PROFILE D, TRIANGULAR (COLD CENTER) IN H_2/O_2 FLAME

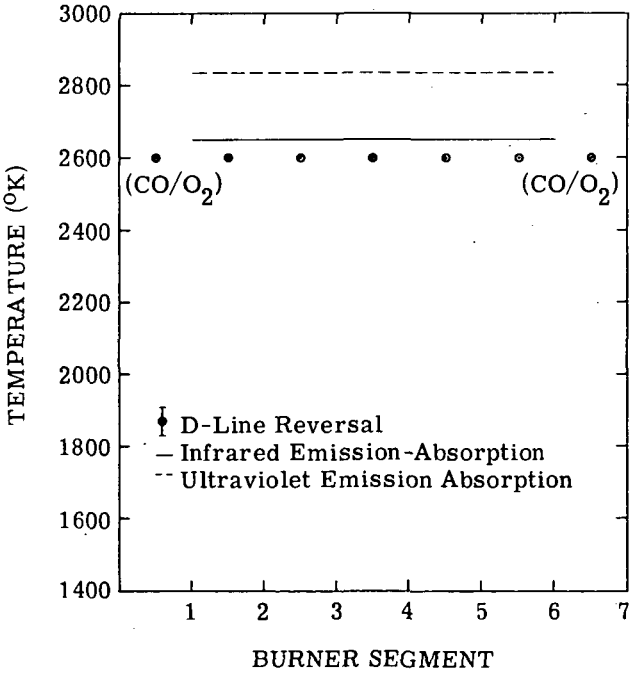

FIGURE 15. TEMPERATURES, PROFILE E, ISOTHERMAL (SHIELDED) IN H_2/O_2 FLAME

4.2. ULTRAVIOLET SPECTRA

The instrumentation for the OH measurements could not easily record on punched cards. Therefore, the data were recorded only on a strip chart and the reduction performed by hand. However, since the lines were isolated and the slit function of the spectrograph approximately triangular, the integrated radiances and equivalent widths could be taken as proportional to the heights of the lines on the charts. Errors caused by this procedure would mostly cancel in the determination of apparent temperature (Eq. 8), provided that the apparent widths of the emission and absorption lines are the same; the remaining errors were of the order of the experimental uncertainty. A more detailed reduction of the absorption spectrum of the isothermal flame was performed for the rotational temperature analysis discussed later. In this case, equivalent widths were obtained with a planimeter.

Figure 16 shows a portion of the absorption spectrum of an isothermal H_2/O_2 flame obtained under the best resolution possible with this instrument. The lines were identified by comparison with the spectra obtained by Kostkowski and Broida [13]. Unfortunately, the energy in emission was not sufficient to be measured with an acceptable signal-to-noise at this 10-μm slit opening. Accordingly, the sets of emission and absorption spectra were obtained with a 25-μm slit opening.

Emission and absorption in the R_2 branch of the $v = 0 \rightarrow 0$ band of OH were measured for the five profiles in H_2/O_2 flames described by Figs. 11 through 15, as they were for the infrared. The unreduced emission and absorption spectra, with the calibration traces superimposed, are presented in Appendix V.

Reduced data, the total radiances, equivalent widths, and apparent temperatures obtained for seven well-isolated lines ($R_2$1, 3, 4, 7, 14, 15, and 20) are presented in Table 3.

4.3. ISOTHERMAL TEMPERATURES

If the infrared and ultraviolet portions of the spectrum are to be useful together for the prediction of temperature profiles, the processes involved must be shown to yield identical temperatures in an isothermal flame. Such a requirement generally means that the processes must be in thermodynamic equilibrium. The emission-absorption temperatures measured for the isothermal flame in the infrared region agreed with the sodium line-reversal temperatures within the overall experimental accuracy. However, as indicated in Table 3 and in Fig. 15, the emission-absorption temperatures measured for this profile in the ultraviolet are approximately 200°K higher, a discrepancy which cannot be explained by radiometric errors in the experimental procedure.

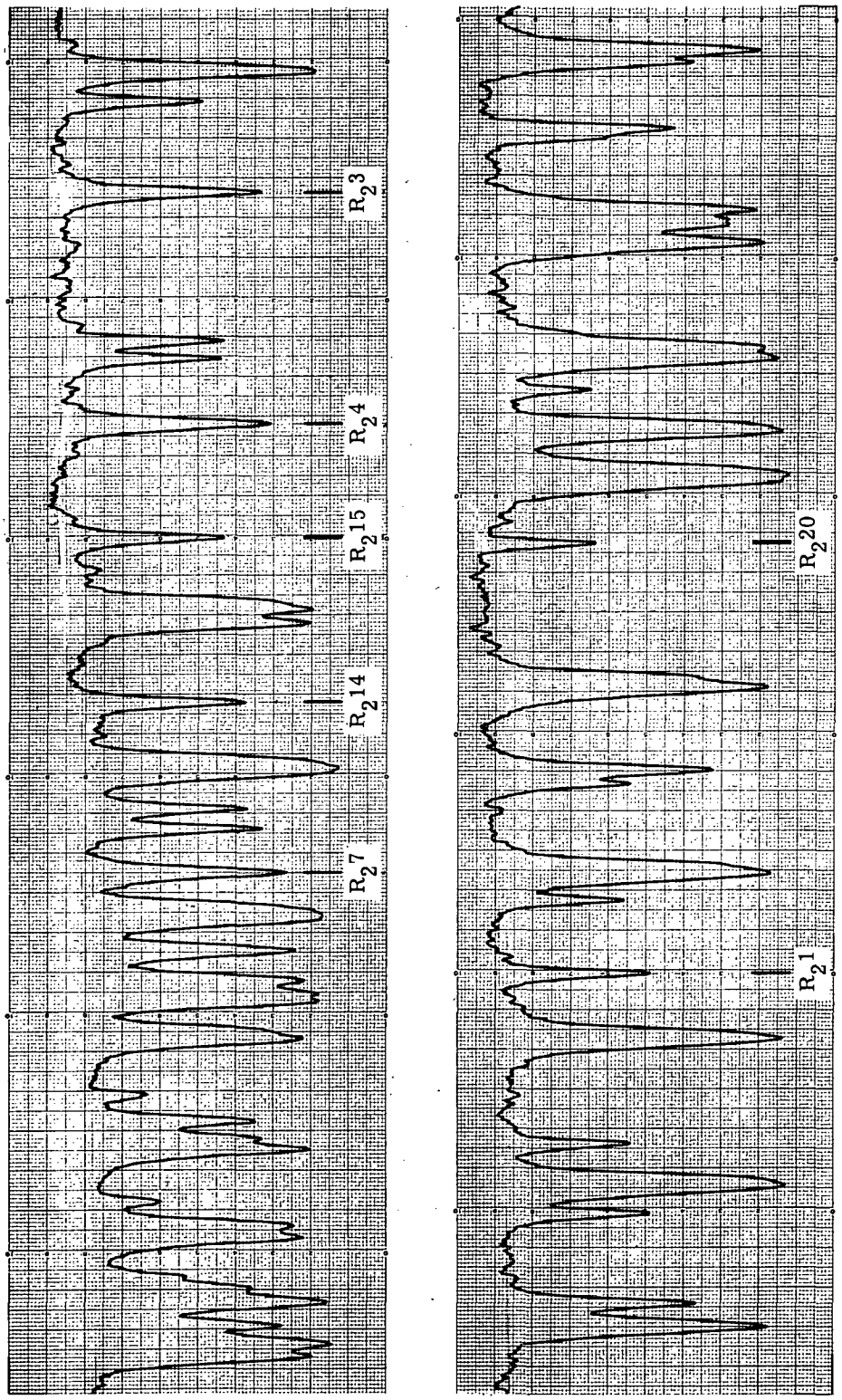

FIGURE 16. ULTRAVIOLET ABSORPTION SPECTRUM OF ISOTHERMAL FLAME

TABLE 3. REDUCED DATA FOR OH LINES*

Line	ν_o	Profile: A L	A W	A T*	B L	B W	B T*	C L	C W	C T*	D L	D W	D T*	E L	E W	E T*
$R_2 1$	32416	0.82	0.306	2820	1.17	0.306	2847	1.64	0.382	2921	3.17	0.538	2938	2.60	0.694	2860
$R_2 3$	32490	1.39	0.517	2769	1.68	0.517	2799	2.75	0.601	2914	4.41	0.813	2927	2.95	0.953	2839
$R_2 4$	32518	1.5	0.678	2763	1.70	0.678	2797	2.73	0.736	2881	4.60	0.983	2917	2.94	1.24	2813
$R_2 7$	32573	1.52	0.590	2767	2.24	0.590	2827	3.35	0.746	2898	5.34	0.983	2939	3.25	1.31	2831
$R_2 14$	32552	1.15	0.372	2796	1.65	0.372	2828	2.61	0.497	2911	3.77	0.701	2945	2.21	0.872	2831
$R_2 15$	32532	1.42	0.371	2826	1.34	0.371	2832	1.86	0.438	2917	3.43	0.619	2949	2.10	0.693	2854
$R_2 20$	32363	0.77	0.152	2940	0.278	0.152	2753	1.07	0.185	2956	0.270	0.348	2974	1.32	0.380	2822

*ν_o = line-center frequency, cm^{-1}

L = integrated line radiance, $\mu W/cm^2$-sr

W = equivalent width, cm^{-1}

T* = apparent temperatures, ^oK

The uncertainty in the radiance calibration (about 25°K) is far too small to account for such a large discrepancy. Also, scattered light and stray light from the first order of the grating were known to be negligible.

One is then tempted to ascribe the high emission levels to an excess population of $^2\Sigma^+$ OH radicals. This would indicate the prescence of a departure from thermal equilibrium and, hence, chemiluminescence in the gases above the reaction zone. A number of authors [14-18] have observed exactly these effects to a very significant extent within and near the reaction zone of premixed flames at atmospheric pressure, presumably caused by radical recombination. Such luminescence might be a possible explanation for the high ultraviolet emission-absorption temperatures observed here.

On the other hand, the reaction zone of the flame in the current experiment, in the center burner segment at least, appeared to be below the slit image. The reaction zone could be seen to begin about 1/16 in. above the burner and to extend as a rather diffuse layer to perhaps 5/32 in. above the end of the burner tubes. The image of the spectrograph and spectrometer slits was located, although imprecisely, above this reaction surface. We estimate that the lower boundary of the slit image was about 1/8 in. above the burner in all cases. The gas velocities were such that the gases took approximately 10^{-3} sec to travel from the bottom of the reaction zone to this lower boundary of the slit image. Most evidence indicates that at atmospheric pressure, the OH should have equilibrated by this time. The slit image was located over the center burner segment during all measurements and, because of the above reasoning, the gas measurements for this segment should have been made in a region where thermodynamic equilibrium was established. However, because of the divergence of the beam between the slit image and the objective lens 20 in. away from the slit image (Item 22 in Fig. 3), portions of the beam passed much closer than 1/8 in. to the burner in the outer segments. We believe that this passage of a fraction of the beam very close to the burner surface is the best explanation for the high emission-absorption temperatures in the ultraviolet. When the beam passes within 1/8 in. of the burner, emission from the reaction zone, including OH chemiluminescene, will be sensed. Because of the imprecision in the slit image position, we estimate that as much as perhaps 10 percent of the beam volume was within or near the reaction zone. However, considering the levels of shemiluminescence observed in [14-18], this percentage does not seem sufficient to explain the high emission values leading to the high emission-absorption temperatures. The emission values are such that about 3.5 times as much OH emission is observed as would be observed from the combustion products at equilibrium at a temperature of 2600°K. It is possible, that, considering the variety of results observed in the entries of [14-18] and considering that the current situation is greatly different from any of the situations described in [14-18], the region of chemiluminescence might extend significantly above the apparent reaction zone so that much

more than 10% of the beam could observe OH chemiluminescence.

The OH absorption values were affected much less by this beam divergence because, although the amount of OH in the reaction zone is above the equilibrium amount, it does not exceed the equilibrium amount by orders of magnitude, and most of it remains in the ground state. Conversely, the emission is governed by the population of the $^2\Sigma^+$ state of OH, which is orders of magnitude greater in the reaction zone than its extremely small value at equilibrium at 2600°K. The infrared measurements are not severely affected by this beam divergence because the vibrational states of H_2O remain near equilibrium even within the reaction zone, although the H_2O concentration is somewhat lower there.

In other experiments where OH chemiluminescence was observed, the rotational temperature of both the $^2\pi$ and the $^2\Sigma$ states of OH were near the flame temperature. To check to see that our measurements concur with the result, an analysis of the rotational structure of the isothermal flame (Profile E) spectra was performed in absorption with the use of Eq. (20). When the same line width for all rotational lines was used, temperatures in absorption near 2570°K were obtained for line widths of 0.03 and 0.05 cm^{-1} (corresponding to values of a equal to 0.3 and 0.5 at 1485°K). The results are shown in Fig. 17a and agree to within the experimental uncertainty with the infrared and sodium line-reversal temperatures. With the values for the line widths obtained from Nadler and Kaskan (shown in Table 2), an unusually low temperature in absorption of 2260°K was obtained (Fig. 17b) which casts further doubt on the applicability of their results to this study. This analysis shows that, while a uniform change in the line half-width of all rotational lines appears to have little effect on the rotational temperature obtained, the assumed variation of line half-width with rotational quantum number appears to have a great effect. The different rotational temperatures obtained illustrate the difficulties in the performance of a rotational temperature analysis when the lines are in the region of square-root growth.

Accordingly, we have ascribed the discrepancy between the ultraviolet emission-absorption temperatures and the infrared and sodium temperature to the inclusion of a region of OH chemiluminescence in part of the beam. It was originally hoped that we would be able to use both the infrared and ultraviolet measurements together in the inversion procedures, but the temperature discrepancies made such a procedure impractical. In the inversion procedures, the ultraviolet and infrared results were each considered separately.

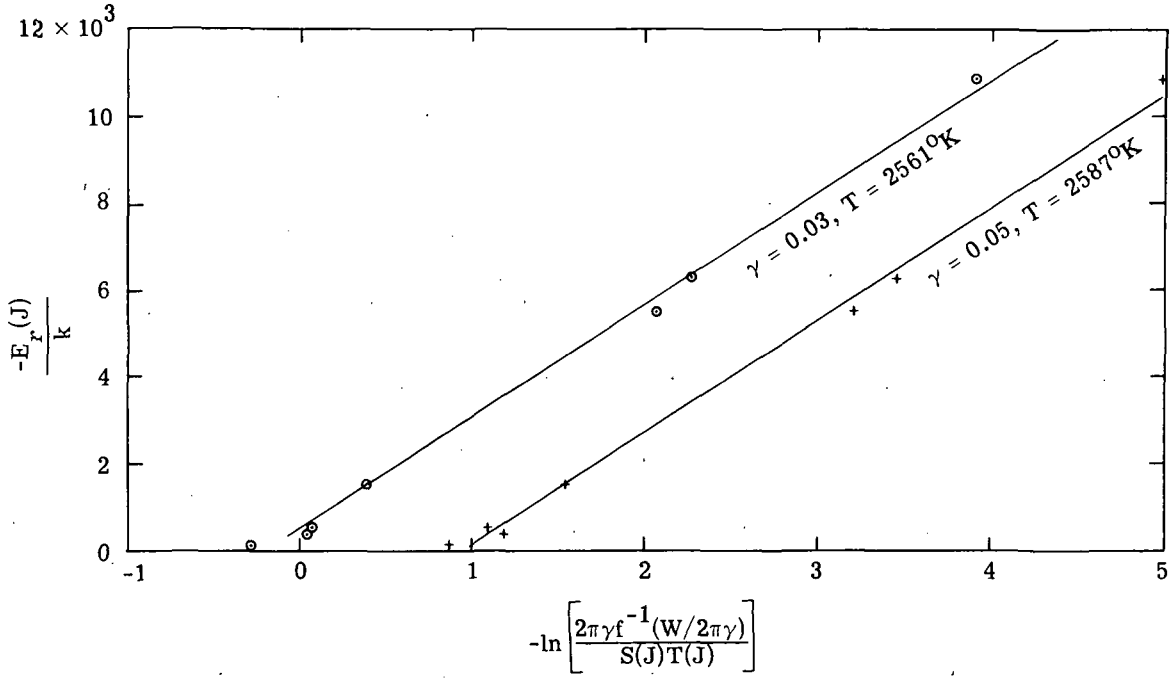

(a) With Constant Line Widths of 0.03 and 0.05 cm^{-1}

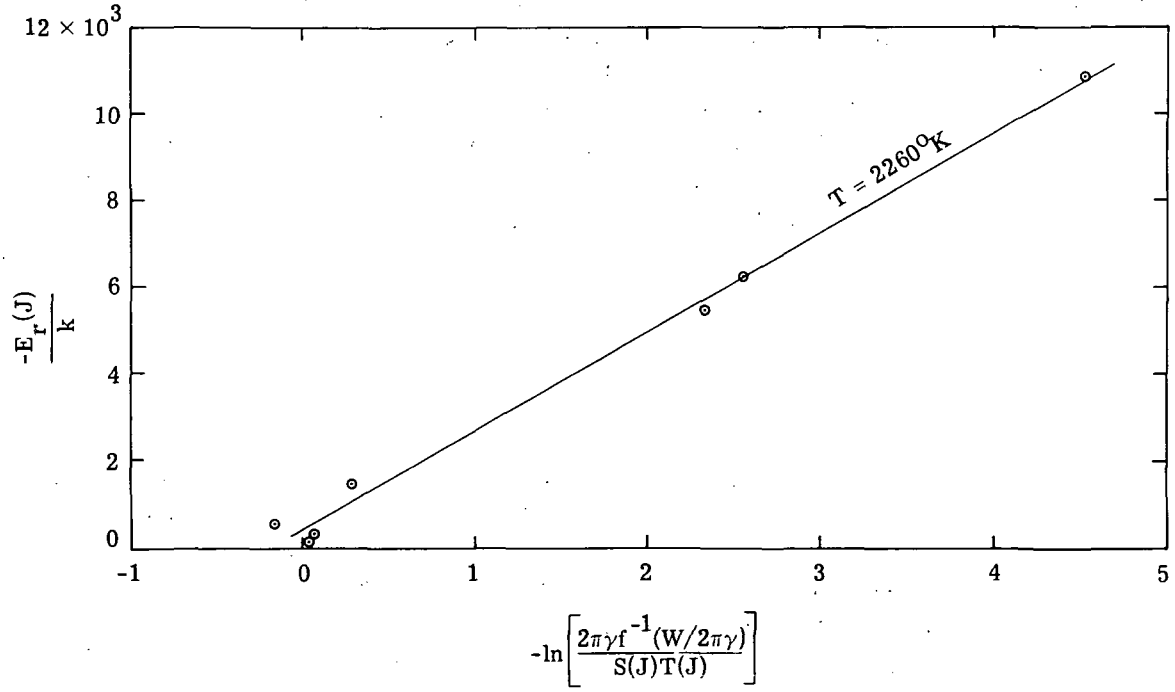

(b) With Line Widths Derived from Nadler and Kaskan [9]

FIGURE 17. RESULTS OF ROTATIONAL TEMPERATURE ANALYSIS OF ISOTHERMAL ABSORPTION SPECTRUM

5

INVERSION PROCEDURES

There are a number of distinct approaches that have variously been utilized for inversion of spectroscopic measurements of flames and hot gases. These could be categorized as being either formal or empirical. Each category encompasses a considerable variation in approach. To accomplish the inversion, a formal approach could be based on either a mathematical operation, such as the Abel transform [12] or on a numerical computation, in which a set of radiative-transfer equations are simultaneously solved. In the latter approach, a set of n equations (e.g., Eq. 4), representing measurements of emission and absorption at n wavelength intervals, could, in principle, be solved to yield profiles in temperature and concentration characterized by a total of n parameters. The problems in performing such calculations and obtaining convergence with real data with finite uncertainties are discussed in the literature.

Recently the empirical approach has been found to be more useful. This approach utilizes auxiliary information to insure convergence in the inversion computation. For example, in the inversion of spectral data obtained with satellite-borne sensors, profiles in atmospheric temperature and water-vapor concentration are rapidly obtained by use of the nominal profiles of a standard atmosphere as a starting point in the iteration [19]. Analogously, determination of temperature and concentration profiles in gas dynamic systems such as combustion or propulsion devices is easier if we have prior knowledge of the general shape of the profiles to be expected. This information is usually available from theoretical gas dynamic considerations. Thus, in the prior study of temperature-profile determination in hot furnace-heated gas samples [1], the inversions were based on the assumption of known profiles, relatively simple in shape, which would usually be characterized by one to three parameters.

In the present study, the same basic approach was taken. However, in the case of flames, both the concentration and temperature profiles were unknown, so that the inversions were more difficult. For this reason, the temperature profiles studied were limited to simple shapes, linear and symmetrical triangular, which could be characterized by two parameters, the maximum and minimum temperatures. Furthermore, because of the nearly linear relationships between the theoretical adiabatic flame temperature and the partial pressures of H_2O (shown in Fig. 18), the same shape could be taken for the profiles in this quantity also. The theoretical temperatures and compositions for adiabatic H_2O, CH_4-O_2 and CO-O_2 flames were obtained from the NASA thermochemistry computer-code [20]; the values are presented in Tables 4-6.

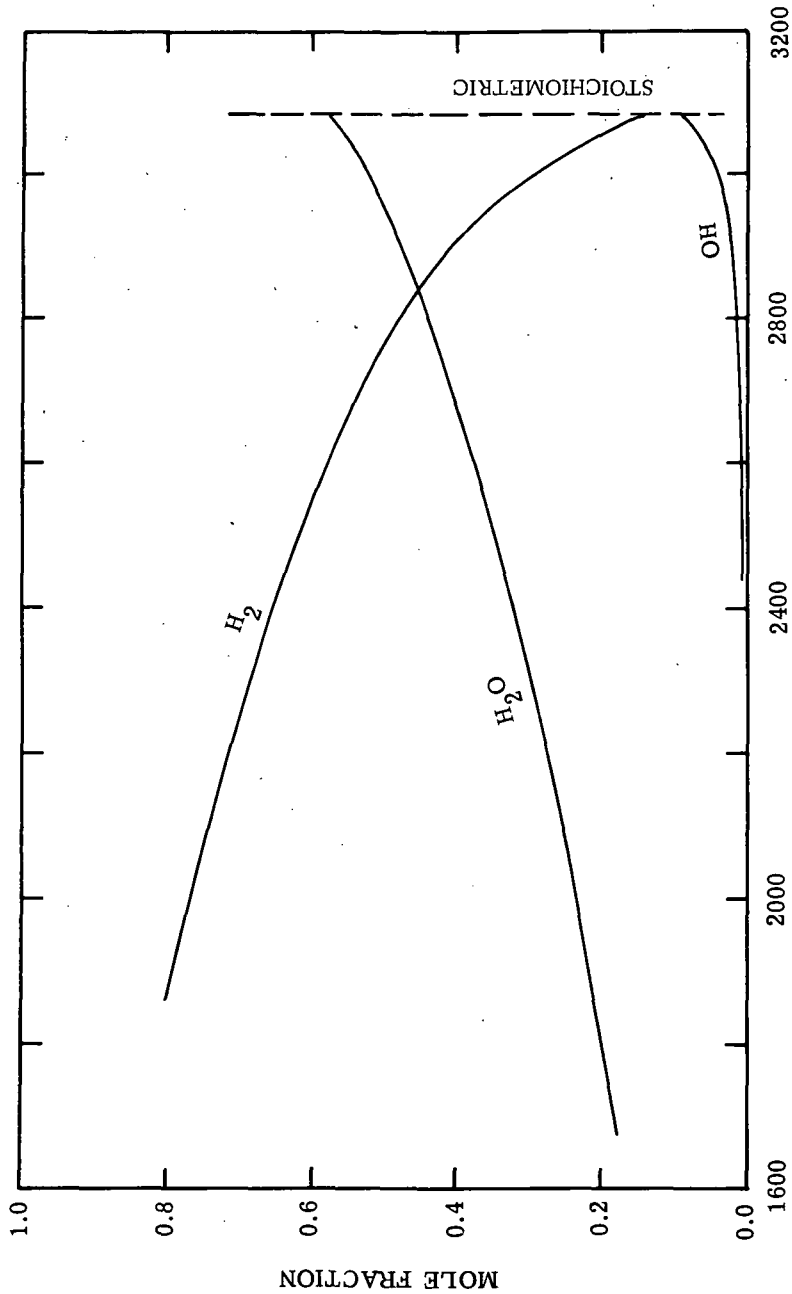

FIGURE 18. COMPOSITION OF ADIABATIC H_2/O_2 FLAME [20]
(FUEL RICH)

TABLE 4. THERMODYNAMIC PROPERTIES OF ADIABATIC H_2/O_2 FLAME

Oxidizer to Fuel Ratio	2.0	4.0	6.0	8.0	10.0
Equivalence Ratio	3.97	1.984	1.323	0.992	0.794
P (atm)	1.0	1.0	1.0	1.0	1.0
T (^{o}K)	2065	2837	3047	3078	3054
Enthalpy (cal/gm)	0.0	0.0	0.0	0.0	0.0
Entropy (cal/gm^{o}K)	8.446	6.080	4.978	4.339	3.921
Average Molecular Weight	6.041	9.649	12.56	14.90	16.82
$(\partial \ln V/\partial \ln P)_T$	-1.001	-1.023	-1.063	-1.077	-1.068
$(\partial \ln V/\partial \ln T)_P$	1.015	1.466	2.246	2.518	2.363
Specific Heat at Constant Pressure (cal/gm^{o}K)	1.661	3.100	4.819	4.771	3.912
Specific Heat Ratio	1.255	1.137	1.115	1.112	1.112
Sonic Velocity (m/sec)	1889	1667	1500	1382	1295
Mole Fractions					
H	0.0021	0.0624	0.0906	0.0765	0.0570
H_2	0.7461	0.4558	0.2507	0.1486	0.0952
H_2O	0.2516	0.4610	0.5585	0.5811	0.5745
O	-	0.0016	0.0156	0.0336	0.0443
OH	0.0001	0.0185	0.0705	0.1070	0.1209
O_2	-	0.0007	0.0140	0.0531	0.1081

TABLE 5. THERMODUNAMIC PROPERTIES OF ADIABATIC CH_4/O_2 FLAME

Oxidizer to Fuel Ratio	1.0	2.0	3.0	4.0	5.0
Equivalence Ratio	3.99	1.995	1.330	0.997	0.798
P (atm)	1.0	1.0	1.0	1.0	1.0
T (^oK)	1039	2618	3031	3053	3018
Enthalpy (cal/gm)	-557.7	-371.8	-278.9	-223.1	-185.9
Entropy (cal/gm^oK)	4.167	3.883	3.473	3.193	2.997
Average Molecular Weight	11.60	15.80	19.21	21.50	23.23
$(\partial \ln V/\partial \ln P)_T$	-1.064	-1.008	-1.057	-1.070	-1.062
$(\partial \ln V/\partial \ln T)_P$	1.954	1.166	2.148	2.415	2.282
Specific Heat at Constant Pressure (cal/gm^oK)	3.262	1.104	2.992	3.194	2.773
Specific Heat Ratio	1.158	1.173	1.115	1.110	1.110
Sonic Velocity (m/sec)	928.7	1271	1209	1145	1095
Mole Fractions					
CO	0.2729	0.2913	0.2153	0.1547	0.1124
CO_2	0.0204	0.0371	0.0840	0.1134	0.1289
H	-	0.0245	0.0645	0.0499	0.0351
H_2	0.6128	0.3542	0.1396	0.0731	0.0447
H_2O	0.0371	0.2880	0.3953	0.3913	0.3708
O	-	0.0002	0.0179	0.0392	0.0479
OH	-	0.0047	0.0630	0.0938	0.0994
O_2	-	0.0001	0.0205	0.0848	0.1608
C(S)	0.0316	-			
CH_4	0.0251	-			

TABLE 6. THERMODYNAMIC PROPERTIES OF ADIABATIC CO/O_2 FLAME

Oxidizer to Fuel Ratio	0.150	0.300	0.450	0.572	0.750
Equivalence Ratio	1.584	1.311	1.119	0.999	0.865
P (atm)	1.0	1.0	1.0	1.0	1.0
T (^{o}K)	2198	2915	2975	2977	2958
Enthalpy (cal/gm)	-820.1	-725.4	-650.4	-599.9	-538.9
Entropy (cal/gm^{o}K)	2.083	2.099	2.094	2.087	2.076
Average Molecular Weight	32.21	34.61	35.16	35.42	35.68
$(\partial \ln V/\partial \ln P)_T$	-1.000	-1.032	-1.052	-1.055	-1.053
$(\partial \ln V/\partial \ln T)_P$	1.000	1.722	2.133	2.204	2.165
Specific Heat at Constant Pressure (cal/gm^{o}K)	0.3195	1.251	1.722	1.795	1.744
Specific Heat Ratio	1.240	1.116	1.108	1.107	1.107
Sonic Velocity (m/sec)	838.6	883.8	882.8	879.4	873.4
Mole Fractions					
CO	0.7374	0.5350	0.4194	0.3491	0.2703
CO_2	0.2626	0.4155	0.4463	0.4553	0.4576
O	-	0.0154	0.0329	0.0409	0.0462
O_2	-	0.0342	0.1015	0.1547	0.2260

Since the H_2-O_2 flames were found to be non-adiabatic, we have included Table 7, also obtained from Ref. 20, which gives the mole fraction of OH for such flames.

Since there were four unknowns, at least four spectral data points were required to accomplish the inversion of the infrared spectral data. One choice would have been four values of the combined emission-absorption spectrum, expressed in the apparent temperature, T*. Such a choice would have preserved consistency with the previous study in which temperature profiles were deduced by matching curves of observed values and band-model predictions of T* as a function of absorptance. In the present study, it was more practical to utilize the emission and absorption data separately at two wavelengths representing fairly high and fairly low optical depths; the frequencies 3100 and 3400 cm^{-1} were selected for this purpose. The values of the maximum and minimum temperature and water partial pressures were adjusted iteratively in calculations using Eqs. (1) and (3) until a best fit was obtained at the selected wavelengths in the emission and absorption spectra. (Actually, values of apparent temperature were used in place of radiance for convenience.) The OH inversion proceeded analogously. Since the lines were well separated, Eqs. (6) and (7) were used for the theoretical predictions with the line strengths given in Table 1. The line widths of Nadler and Kaskan (Table 1) were also used, except where noted.

Initially, it was thought that the flames would be adiabatic, so that there would be a one-to-one correspondence between the local temperature and the mole fraction of OH according to Fig. 18. However, the temperatures determined by the various methods for the isothermal profile, which was set close to a stoichiometric mixture ratio, are considerably lower than the theoretical values, indicating a departure from adiabaticity. This failure to achieve the theoretical flame temperatures indicated that it would no longer be valid to use Fig. 18 to relate the temperature to the OH mole fractions, and hence that the OH-inversion would require four parameters also.

In this case, however, a linear variation in OH pressure over the entire length of the burner would not be reasonable, as the degree of dissociation of H_2O is a steep function of temperature. An alternative four-parameter iteration procedure would have involved compound linear variations as specified by the quantities T_{max}, $P(OH)_{max}$, T_{min}, and X_{min}, where X_{min} represents the distance along the burner at which the pressure of OH is taken to be zero, and T_{min} is the corresponding temperature. However, a continuous variation in X_{min} could not be accommodated because the computation was set up in terms of seven isothermal regions corresponding to the burner segments. Therefore, a different approach was taken to treat the OH spectra.

To determine the OH concentration as a function of temperature, the absorption spectrum of the isothermal flame was examined in detail. The sodium line-reversal

TABLE 7. MOLE FRACTION OF OH FOR NON-ADIABATIC CONDITIONS, H_2-O_2 COMBUSTION AT 1 ATM.

O/F	2.0	4.0	6.0	8.0	10.0
T, °K					
3100	.01990	.04600	.07920	.10980	.12760
3000	.01420	.03370	.06180	.09250	.11030
2900	.00980	.02360	.04560	.07520	.09260
2800	.00650	.01580	.03170	.05910	.07560
2700	.00410	.01010	.02090	.04490	.06010
2600	.00250	.00620	.01310	.03290	.04650
2500	.00150	.00370	.00780	.02340	.03500
2000	.00005	.00011	.00024	.00250	.00510
1500	.00000	.00000	.00000	.00009	.00019
T(adiabatic)	2065	2837	3047	3078	3054
OH (Mole Fraction)	.0001	.0185	.0705	.1070	.1209

temperature, the infrared emission-absorption temperature, and the rotational temperature obtained from an analysis of the relative line intensities all gave temperatures near 2600°K. Thus, it seemed reasonable to assume 2600°K for the vibration-rotation temperature of the flame. By using Eq. (18) with the line intensities of Table 1 and a temperature of 2600°K, an estimate was obtained of the OH concentration required to give the measured equivalent widths for the 7 lines considered. One estimate was obtained when the line widths of Nadler and Kaskan (Table 1) were used, and one estimate was obtained with a uniform line width of 0.04 cm^{-1}. A value for the mole fraction of OH of 0.028 was obtained in both cases. This value is considerably below the OH concentration for a stoichiometric adiabatic flame and considerably above that for an adiabatic flame at 2600°K, further indication of the departure from adiabatic conditions. Reliable experimental oxidizer-fuel ratios could not be obtained, because the fuel control valves could not be calibrated. However, since we were striving for near-maximum temperatures during the isothermal runs, the oxidizer-fuel ratio for these runs would have been slightly less than 8; the value corresponding to the maximum adiabatic temperature. The value obtained from the line strengths for the OH mole fraction, 0.028, compares favorably with the value of 0.033 in Table 7 for 2600°K and an oxidizer-fuel ratio of 8. This agreement also indicates that the majority of the beam passes through a portion of the flame where OH concentration is near its equilibrium value. Table 8 shows the observed equivalent widths for these lines and computed equivalent widths for two OH concentrations and for both choices of line width.

The inversion procedure was applied in the ultraviolet to emission-absorption temperatures which are higher than the vibration-rotation temperature. Because temperatures could not be correlated with mixture ratios it was not possible to use Table 7 to relate temperature to OH concentration, hence the adiabatic curve for OH concentration versus temperature shown in Fig. 18 was modified as follows: To ensure that the OH concentration and emission-absorption temperature predicted by the inversion procedure were consistent with the observed values in the isothermal flame, the theoretical curve of P(OH) versus T shown in Fig. 18 was shifted to the left to coincide with the values T ≈ 2835°K and P(OH) = 0.028atm; i.e., the effect of flame cooling is assumed to be independent of the flame temperature and the discrepancy in OH temperature. This procedure yielded a new curve representing a one-to-one correspondence of OH partial pressure with ultraviolet emission-absorption temperature (Fig. 19). (In retrospect, a preferable procedure would have involved a set of high-resolution absorption spectra for isothermal shielded flames at various temperatures.)

This inversion, then, proceeded like the inversion for the infrared data. A pair of lines $R_2 1$ and $R_2 4$, were selected to represent large and small optical depths, respectively. The values of maximum and minimum temperatures (and the corresponding OH concentrations from Fig. 19) were iteratively adjusted in calculations in which Eqs. (6)

TABLE 8. EXPERIMENTAL AND THEORETICAL VALUES OF THE EQUIVALENT WIDTH OF OH LINES IN ISOTHERMAL FLAME AT 2600°K

Line	Observed Equivalent Width (cm^{-1})	Calculated Equivalent Width (cm^{-1})			
		Line Half-Width = 0.04 cm^{-1}		Line Half-Widths from Table 1	
		P(OH) = 0.055	P(OH) = 0.02	P(OH) = 0.055	P(OH) = 0.02
$R_2 1$	0.675	0.887	0.529	0.965	0.580
$R_2 3$	1.05	1.55	0.933	1.46	0.880
$R_2 4$	1.33	1.77	1.07	1.57	0.945
$R_2 7$	(1.46)*	2.04	1.23	1.82	1.09
$R_2 14$	0.863	1.31	0.785	1.39	0.843
$R_2 15$	0.797	1.16	0.695	1.24	0.733
$R_2 20$	0.374	0.532	0.309	0.715	0.400

* Questionable value caused by slight overlap by adjacent line.

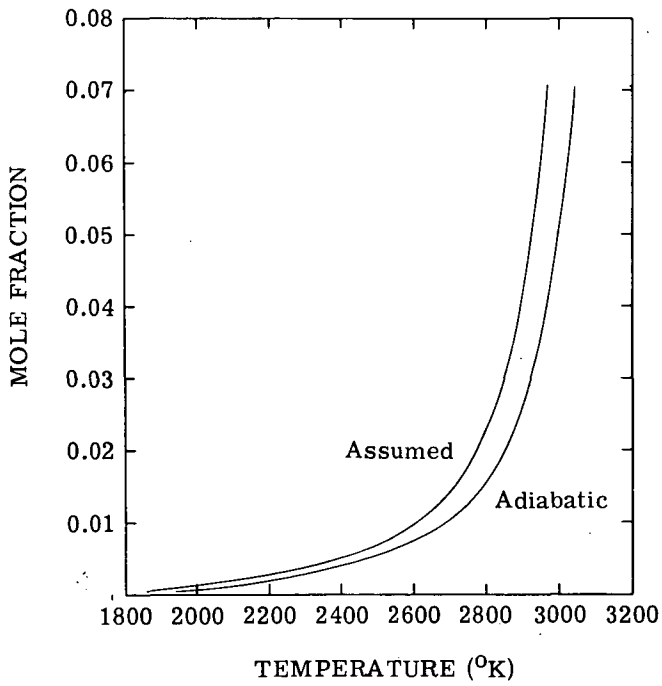

FIGURE 19. MOLE FRACTION OF OH AS A FUNCTION OF TEMPERATURE

and (7) were used. Essentially two temperatures have appeared in the analysis to this point, the rotational-vibrational value measured by three methods and the electronic value measured by ultraviolet emission-absorption spectroscopy. In performing this iteration, one must now choose between the two values. If nonequilibrium effects are occurring, Eq. (5) is no longer valid, and the interpretation of the emission spectrum becomes more difficult. However, since we have ascribed the high ultraviolet temperature to the inclusion of only a small region where non-equilibrium effects are present, we have performed the inversion, using Eq. (5), based on the ultraviolet emission-absorption temperatures. This provides inversion results which agree with the measured integrated radiances.

By this means, we expected to obtain temperature profiles from a simple two-parameter fit of the integrated radiances for these two lines, letting the equivalent widths fall where they may. However, after a few iterations, it became obvious that because of the very steep gradient in OH partial pressure, no information could be obtained about the lower temperature regions in the flame. Test cases for each of the profiles, A through D, showed that a change of $100^{\circ}K$ in the minimum temperature would yield a negligible change in the values of the integrated radiances and equivalent widths of the two lines. The results of these calculations, in effect, yielded only values for the maximum temperatures. Clearly, the experimental study of temperature measurements by OH emission and absorption indicate that they can contribute only to the determination of the maximum temperature.

At the beginning of the present study, the intention was to utilize the results of the above four- and two-parameter fitting procedures as the starting point for a second approximation to the temperature profile. This approximation would have been characterized by 14 parameters, in correspondence with the 7 segments of the burner. For this purpose, 7 wavelengths in the 3100- to 3700-cm^{-1} region would have been selected for the infrared inversion, and 7 well isolated OH lines for the ultraviolet, as specified in Table 2. An iterative calculation, similar to that proposed by Smith [19], would have been employed. However, limitations in time and funds did not permit the inclusion of this analysis.

6

TEMPERATURE-PROFILE DETERMINATIONS

6.1. INFRARED

The temperature profiles obtained from the inversions of the infrared spectra when the procedures detailed in the preceding section were used are shown in Figs. 11 through 14. The results are in qualitative agreement with the temperature profiles measured directly by the line-reversal apparatus. As the iterations proceeded, the convergence upon the temperature and concentration profiles representing the best fits to the observed spectra became quite slow. For expedience, the iterations were terminated when the calculated apparent temperatures and absorptances reasonably matched the observed values. The resultant best-fit conditions are summarized in Table 9. For profiles A through C, the observed and calculated values of T^* and α agreed to within $25^{\circ}K$ and 0.02 at the two selected frequencies. However, the convergence for profile D was much slower, and the calculations were terminated sooner. It was perfectly clear, however, that the results would not have been appreciably altered by further iterations. Therefore, the discrepancies in the temperature profiles as determined from the infrared spectra and the D-line observations remain to be explained. For the linear profiles, the greater differences occur at the lower temperature. (Recall that profiles A and B were achieved by merely rotating the burner 180°.) On the other hand, for the triangular profiles, C and D, the larger discrepancies occur at the higher temperatures.

The reason for this effect is not at all obvious. However, there are several possible sources of error:

(1) As mentioned in a preceding section, the D-line reversal measurement was affected by the addition of the cooling tubes to the top of the burner and the consequent raising of the optical path to a height at which some of the mixing region might have been colored with sodium. It was observed that the reversal did not occur consistently with perfect blending of the D-lines into the background continuum, indicating some variation in temperature along the path.

(2) In the iterative spectral radiance and absorptance calculations made with the bandmodel, the mixing region at each end of the burner was not considered to avoid complicating the inversion procedure. Absorption in the cool mixing region would most affect calculations in which the higher temperatures are closer to the observer. It is felt that this probably accounts for the poor fit of the observed and calculated values of T^* and α shown in Table 9 for profile D.

TABLE 9. COMPARISON OF INFRARED SPECTRAL DATA AND BEST-FIT CALCULATIONS

Profile	T_{max} (°K)	T_{min} (°K)	P_{max} for H_2O (atm)	P_{min} for H_2O (atm)	ν (cm^{-1})	T* (°K)		α	
						Observed	Calculated	Observed	Calculated
A	2700	1540	0.55	0.25	3100	2275	2278	0.095	0.105
					3400	2100	2113	0.275	0.276
B	2725	1625	0.55	0.25	3100	2360	2338	0.090	0.107
					3400	2260	2284	0.265	0.268
C	2800	1700	0.60	0.30	3100	2340	2320	0.105	0.114
					3400	2190	2214	0.300	0.287
D	2800	1700	0.60	0.30	3100	2480	2447	0.125	0.128
					3400	2310	2375	0.310	0.296

(3) Another shortcoming in the calculation procedure involved mixing of flames from the adjacent burners. The calculations were made under the assumption that the optical path consisted of seven isothermal sections, each the width of a burner segment; inclusion of mixing effects between sections would have considerably complicated the analysis. During the iterative calculations, it was obvious that the absorptance at both frequencies, 3100 and 3400 cm^{-1}, depended strongly on the average H_2O concentration and only showed weak response to moderate variations in the concentration profile. This is consistent with the rather slow variation of H_2O concentration with temperature, which, in turn, governs the variation in spectral absorption coefficient. However, the resultant H_2O-concentration profiles shown in Table 10, although they are accurate to no more than 10%, are clearly higher than the corresponding theoretical values shown in Fig. 18. This tends to substantiate the conclusion that the flames were not adiabatic.

6.2. ULTRAVIOLET

The maximum temperatures resulting from the inversions of the OH emission-absorption spectra are also shown on Figs. 11 through 14. Clearly, to display the complete profile of the final iteration would make no sense as the uncertainty at the lower end would be enormous. However, the values used, as given in Table 10, are probably realistic, since the calculated and observed equivalent widths are in fair agreement.

The values of the maximum temperatures so determined are considerably higher than those deduced from the infrared inversions, to a degree comparable to the differences noted in the direct emission-absorption measurements (Fig. 15). This is by no means coincidental, since the OH pressure-temperature relationship is based on this very data.

TABLE 10. COMPARISON OF ULTRAVIOLET SPECTRAL DATA AND BEST-FIT CALCULATIONS

Profile	T_{max} (^{o}K)	T_{min}* (^{o}K)	P_{max} for OH (atm)	Line	L (μW/cm^2-sr) Observed	L (μW/cm^2-sr) Calculated	W (cm^{-1}) Observed	W (cm^{-1}) Calculated
A	2900	1600	0.043	$R_2 1$	0.82	0.93	0.306	0.450
				$R_2 4$	1.50	1.40	0.678	0.763
B	2860	1600	0.033	$R_2 1$	1.17	1.07	0.306	0.409
				$R_2 4$	1.70	1.82	0.678	0.694
C	2940	1700	0.060	$R_2 1$	1.64	1.70	0.382	0.488
				$R_2 4$	2.73	2.56	0.736	0.831
D	2940	1700	0.060	$R_2 1$	3.17	3.03	0.538	0.648
				$R_2 4$	4.60	5.01	0.983	1.092

* Highly uncertain

7

CONCLUSIONS AND RECOMMENDATIONS

As a result of the current experimental program, it appears that, in the infrared region at least, temperature profiles in flames can be measured by emission-absorption spectroscopy in the same manner as the hot gases of the previous study [Ref. 1]. The uncertainties in the temperatures deduced during the current series of measurements were approximately 30° to 50°K while the temperature uncertainty in the earlier program was about 10°K.

An error analysis was undertaken which considered the temperature differences (2600°K versus 1200°K) and absorption differences (~ 1.0 versus ~ 0.3) between the current work and the earlier work. This analysis indicates that with similar experimental accuracies in the two programs, an uncertainty in temperature between three and six times as great should be expected for this program as compared to the previous program. Hence, the experimental uncertainties of the two programs are probably of the same order.

An additional uncertainty existed in this program which was not present in the earlier program: the sodium line-reversal measurements were made farther from the reaction zone than the infrared measurements, far enough so that mixing had begun to affect the sodium line temperature. Corrections for this were applied as shown in Fig. 5. However, the correction was small ($\sim 35^{\circ}$K), so that after the correction was applied, the residual error in the sodium reversal measurements was probably significantly smaller than the other uncertainties.

Thus, the infrared emission-absorption technique for spectral inversion is applicable to flames as well as to hot gases which exhibit a wide range of temperatures. The parametric inversion of infrared spectra should be capable of providing temperature and water-vapor profiles as reliable as the general profile shapes that are provided.

On the other hand, it does not appear that the emission absorption technique in the ultraviolet OH band will be quite as useful in flames as the infrared region because, within the reaction zone, the electronic states of OH are very substantially out of equilibrium with the kinetic temperature of the gas and substantial chemiluminescence is occurring [Refs. 14-18]. Thus, the temperatures measured in the reaction zone by emission-absorption in the OH band will be significantly higher than the kinetic temperature. It is our opinion that, in the current program, a portion of the beam viewed the reaction zone, a condition which led to higher emission-absorption temperatures in the ultraviolet than in the infrared. If the measurements in the current program had been

made somewhat further above the burner face, (where the temperatures would have been perhaps 50°K lower) this anomaly would not have appeared. Further experiments are required to test this hypothesis. However, the existence of nonequilibrium in the OH radicals places fundamental limitations on the regions in which emission-absorption probing by use of OH radiation is reliable. In particular, the use of this technique in and near combustion zones would not yield reliable results. Unfortunately, the sensing of combustion-zone temperatures constitutes an important set of potential uses for such techniques, since it is highly desirable to sense temperatures in at least the higher temperature regions by short wavelength emission.

Because of the very rapid variation of the equilibrium OH concentration with temperature, a disproportionately large fraction of the OH emission (and absorption) originates in the hottest portions of the flame. The result of this condition is that, in the inversion of the OH data to obtain temperatures, while the temperature of the hotter portions of the flame can be accurately extracted, the extraction of the temperature of the cooler portions is subject to very substantial uncertainty. This difference indicates that the OH radiation is best suited for the extraction of the maximum temperature of a gas having large temperature variations, and the infrared or other techniques should be used to extract the temperatures of the cooler regions.

It is desirable to sense temperatures in at least the higher temperature regions of a gas flow from the short wavelength emission primarily because of the greater sensitivity of the Planck function to temperature at shorter wavelengths. However, if regions are to be included in which nonequilibrium of the OH is a possibility, the use of an emission-absorption technique in the OH band should probably be abandoned. Other techniques in the ultraviolet should be investigated as possible means of temperature inversion in nonisothermal flames. Temperature inversion based on the relative intensity of the rotational lines within a band has been highly developed for isothermal paths (as used in this report) and perhaps could be generalized to yield temperature profiles across nonisothermal paths. However, such techniques will sacrifice much of the potential advantage of the short wavelength region, since the absolute emission values, the source of the potentially superior accuracy of the ultraviolet region when equilibrium is present, must be discarded where nonequilibrium exists. Furthermore, lack of knowledge of accurate transition probabilities and line widths limit the accuracy of rotational line analyses. It seems that ultraviolet line-of-sight probing techniques that are not based upon emission-absorption will not be substantially more accurate than infrared measurements and will be at least as difficult to perform experimentally.

Accordingly, future efforts should be directed toward a delineation of those regions and conditions in which temperature inversion by OH emission-absorption spectrometry is valid (i.e., where OH chemiluminescence is not significant). The various entries of

Refs. [14-18] describe observations of various degrees of chemiluminescence, all of which indicate OH nonequilibrium, within and near a reaction zone, and then downstream decay to complete equilibrium. However, the spatial extent of the chemiluminescence varies in the different cases, depending on the reactants and the flame conditions. The spatial extent is not known in general and, as indicated by the current work, could possibly be more extensive for diffusion flames than for premixed flames. Thus, it seems that a more complete study of the conditions under which substantial chemiluminescence of the OH molecule occurs must be carried out. This study could begin by probing an atmospheric pressure, H_2-O_2, diffusion flame of the type used in the present study with both sodium and lithium line-reversal measurements and OH emission-absorption measurements. Such a study would allow the determination of various translational and OH rotational temperatures and OH $^2\Sigma^+$ population throughout the flame. The results would indicate the regions in the burner flame where OH chemiluminescence is important and hence provide information whereby the currently obtained, high emission-absorption temperatures in the ultraviolet could be explained. Further theoretical studies would still be required (besides the results in Refs. [14-18]) to attempt to generalize the conditions governing OH chemiluminescence. The results of this study would provide a means for determining whether a particular physical situation or region would yield OH chemiluminescence, and thus a means for deciding whether OH emission-absorption measurements with their potentially better temperature accuracy would be worthwhile for temperature probing in that region.

Uncertainty in the temperature determined for a burner segment from the OH measurements was strongly dependent on the OH content and hence temperature in that segment. The accuracy of the ultraviolet temperature determination is variable along the line of sight. An additional analytical study should be performed to determine a method by which ultraviolet and infrared emission absorption measurements can be combined so that the accuracy of the temperature profile all along the line of sight is maximized.

Appendix I
A BAND MODEL FORMULATION FOR VERY NONUNIFORM PATHS

I.1. INTRODUCTION

The particular band model used for the research described in this report was developed at Willow Run Laboratories [1, 2], and was originally formulated in terms of a nearly-weak or a nearly-strong (NW-NS) line approximation. A simple procedure for interpolation between the two approximations provided for intermediate optical depths. Applications of this band model in its original form yielded anomalous results; at some frequencies, the calculated values of apparent radiance with atmospheric absorption exceeded those for the hot source alone. Reasons for these inconsistencies were determined and corrections made. In the body of the report, we presented both results of the use of the modified band model and the requirements for a more complex interpolation procedure. The purpose of this appendix is to present the details of the revised formulation of the model, which represents a closer approximation to the exact equation of transfer than the original model, or comparable ones which have been based on the Curtis-Godson approximation.

The rationale in the development of the new model can be illustrated by considering the growth of a single, collision-broadened spectral line along a nonisothermal path. Once the formulation for such a single line is developed, it is carried over essentially unchanged to the case of a random band of overlapping lines.

The solution of the equation of transfer which describes the radiance of a single, isolated, spectral line from a general nonisothermal source under the conditions of local thermodynamic equilibrium, negligible scattering, and no significant source of radiation behind the gas, is

$$L_\nu(\nu) = \int_0^{X_L} L_\nu^*(\nu, X) k(\nu - \nu_o, X) \exp\left[-\int_0^X k(\nu - \nu_o, X')\, dX'\right] dX \qquad (21)$$

where X is the optical depth (mass per unit cross-sectional area) coordinate along the line of sight through the gas. $L_\nu^*(\nu, X)$, the blackbody spectral radiance, is a function of frequency, or equivalently wave-number, ν, and temperature, $T = T(X)$; T in turn, is a function of the position along the line of sight through the gas. The spectral absorption coefficient of the single line being considered, $k(\nu - \nu_o, X)$, is a function of the spectral distance from the line center, $\nu - \nu_o$, and the optical depth coordinate along the path, X. $L_\nu(\nu)$ is the spectral radiance of the gaseous source at wave-number ν resulting from the single spectral line. X_L is the total optical depth of the gaseous source. The total radiance from the line is obtained by integration over all frequencies:

$$L = \int_{-\infty}^{\infty} \int_{0}^{X_L} L_\nu^*(\nu, X) k(\nu - \nu_o, X) \exp\left[-\int_0^X k(\nu - \nu_o, X')\, dX'\right] dX\, d(\nu - \nu_o) \tag{22}$$

If we introduce the transmittance, defined as

$$\tau(\nu - \nu_o, X) \equiv \exp\left[-\int_0^X k(\nu - \nu_o, X')\, dX'\right] \tag{23}$$

and interchange the order of integration, assuming that $L_\nu^*(\nu, X)$ does not vary significantly over the frequency region involved, the equation for L can be written:

$$L = -\int_0^{X_L} L_\nu^*(\nu_o, X) \frac{d}{dX}\left[\int_{-\infty}^{\infty} \tau(\nu - \nu_o, X)\, d(\nu - \nu_o)\right] dX \tag{24}$$

The equivalent width, W, is defined as

$$W(X) = 1 - \int_{-\infty}^{\infty} \tau(\nu - \nu_o, X)\, d(\nu - \nu_o) \tag{25}$$

so that the expression for L becomes

$$L = \int_0^{X_L} L_\nu^*(\nu_o, X) \frac{dW}{dX}\, dX \tag{26}$$

Since W is only a function of X, the above equation can be written

$$L = \int_0^{W(X_L)} L_\nu^*(\nu_o, X)\, dW(X) \tag{27}$$

If we divide the path into N approximately isothermal elements, the expression for L becomes

$$L \cong \sum_{i=1}^{N} L_{\nu,i}^* [W(X_i) - W(X_{i-1})] \tag{28}$$

where X_i is the optical path from the observer to the far boundary of the i-th isothermal element and $W(X_i)$ is the equivalent width corresponding to that path.

Calculation of the values of $W(X_i)$ shows that, in general, the integrals over X and $\nu - \nu_o$ are not separable for nonisothermal paths. To allow such separation, an approximation for the variation of the line shape along the path is usually made. The Curtis-Godson approximation

is most commonly used for this purpose [21, 22, 23]. Another, is the nearly-weak, nearly-strong line approximation [1]. The purpose of both approximations is the separation of the integrals over X and $\nu - \nu_o$ and the replacement of the nonisothermal path with an equivalent isothermal path. Both yield satisfactory values of W(X) for many cases, especially when the temperature and concentration variations are not too large.

In the evaluation of Eq. (28), the accuracy of the integration depends not so much on the accuracy of the values of W(X), but on the accuracy of differences between values of W(X), i.e., on the derivative of W with respect to X. However, an expression which is a reasonable approximation for W will not always yield a reasonable approximation to dW/dX. To illustrate this, we will compute the derivative of W with respect to X, using both the Curtis-Godson approximation and the NW-NS approximation.

First it is necessary to obtain an expression for the equivalent width of a collision-broadened line in an isothermal path. The absorption coefficient in this case is

$$k(\nu - \nu_o, X') = \frac{S(X')}{\pi} \frac{\gamma(X')}{\gamma^2(X') + (\nu - \nu_o)^2} \tag{29}$$

where S is the line strength and γ its half-width. Upon substitution into Eq. (23) specialized to an isothermal path, and with the use of Eq. (25) the following expression for W is obtained after some reduction [20]:

$$W(X) = 2\pi\gamma \cdot f(x) \tag{30}$$

where f is the Ladenburg-Reiche function.

$$f(x) \equiv xe^{-x}[J_0(ix) - iJ_1(ix)] \tag{31}$$

and $x = \frac{SX}{2\pi\gamma}$ is the dimensionless optical depth. J_0 and J_1 are Bessel functions of the first kind, of order 0 and 1 respectively. Tables of f(x) are found in the literature [25, 26].

I.2. CURTIS-GODSON APPROXIMATION

We have used the form of the Curtis-Godson approximation described by Goody [21]. It is a method in which the equivalent width of an absorption line as viewed through a nonisothermal path can be approximated by the equivalent width through some corresponding isothermal path. The approximation involves the definition of an equivalent average half-width and line strength for the path extending from the observer to some point, X, in the path.

$$S_e(X) = \frac{\left[\int_0^X S(X')\, dX'\right]}{X} \tag{32}$$

(equation continued)

and

$$\gamma_e(X) = \frac{\int_0^X \gamma(X')S(X')\,dX'}{\int_0^X S(X')\,dX'}$$

The denominator in the nonisothermal absorption coefficient (Eq. 29), is taken to be independent of X', of the form, $\gamma_e^2(X) + (\nu - \nu_o)^2$, so that

$$\int_0^X k(\nu - \nu_o, X')\,dX' = \frac{\gamma_e(X)S_e(X)X}{\pi\left[\gamma_e^2(X) + (\nu - \nu_o)^2\right]} \tag{33}$$

From this, it follows that

$$W(X) = 2\pi\gamma_e(X)f(x) \tag{34}$$

where x, the dimensionless optical depth, is now defined as

$$x(X) \equiv \frac{\int_0^X S(x')\,dX'}{2\pi\gamma_e(X)} \tag{35}$$

Equation (34) can now be used to investigate the behavior of dW/dX in a nonisothermal gas. If we differentiate (34) and make use of (32),we get

$$\frac{dW}{dX} = S(X)\left\{\frac{df(x)}{dx}\left[2 - \frac{\gamma(X)}{\gamma_e(X)}\right] + \frac{f(x)}{x}\left[\frac{\gamma(X)}{\gamma_e(X)} - 1\right]\right\} \tag{36}$$

The variation with optical depth X can be mapped into a variation with dimensionless optical depth, x, and Eq. (36) rewritten as

$$\frac{1}{S(X)}\frac{dW}{dX} = \left\{\frac{df(x)}{dx}\left[2 - \frac{\gamma}{\gamma_e}(x)\right] + \frac{f(x)}{x}\left[\frac{\gamma}{\gamma_e}(x) - 1\right]\right\} \tag{37}$$

We can now place physical limitations on $[1/S(X)](dW/dX)$. At X = 0, the quantity $[1/S(X)](dW/dX)$ must be unity corresponding to the region of linear growth for small optical depths. It must also be less than one at larger optical depths as the square root region is approached; and, finally, it must remain non-negative for all x, so that the equivalent width continues to grow as x increases. The variation of $[1/S(X)](dW/dX)$ in Eq. (37) is shown in Fig. 20 as a function of x with γ/γ_e as a parameter. γ/γ_e is the ratio of the half-width at x to its average value taken over all the path before it. For $\gamma/\gamma_e < 2$, the function is well behaved, but not for

$\gamma/\gamma_e > 2$. In the latter case the function becomes larger than one for intermediate values of x, indicating a rate of equivalent-width increase greater than that in the linear region.*

I.2. NEARLY-WEAK, NEARLY-STRONG LINE APPROXIMATION

This approximation, like the Curtis-Godson approximation, defines an average for the line half-width. However, this average is fixed for the path in question and is defined as the average over the total path, X_L:

$$\gamma_{eL} = \frac{\int_0^{X_L} \gamma(X')S(X')\,dX'}{\int_0^{X_L} S(X')\,dX'} \tag{38}$$

Then the dimensionless optical depth is defined as:

$$\bar{x}(X) = \frac{1}{2\pi\gamma_{eL}} \int_0^X S(X')F(X')\,dX' \tag{39}$$

F(X') is a function which must be unity in the NW approximation and γ/γ_{eL} in the NS approximation [5]. A form must be chosen for the variation of F(X') so that it produces a reasonable transition between the two approximations for intermediate optical depths. The equivalent width is given again as

$$W(X) = 2\pi\gamma_{eL} f(\bar{x}) \tag{40}$$

If we take the derivative of Eq. (40 for the NW approximation we obtain

$$\frac{dW}{dX} = S(X)\frac{df(\bar{x})}{d\bar{x}} \tag{41}$$

and for the NS approximation, we obtain

$$\frac{dW}{dX} = S(X)\frac{\gamma(X)}{\gamma_{eL}}\frac{df(\bar{x})}{d\bar{x}} \tag{42}$$

The values for $[1/S(X)]\,(dW/dX)$ (according to Eqs. 41 and 42) are shown in Fig. 21. It can be seen that the NW approximation never becomes physically unrealistic, i.e., $[1/S(X)](dW/dX) \geq 1$;

*These errors, mentioned by Goody [21], are treated in detail by Drayson [22]. However their analyses dealt only with the absorption (or equivalent width). On the other hand, Walshaw and Rodgers [26] analyzed the effect of the Curtis-Godson approximation on the derivative of transmittance with optical depth, for several band models.

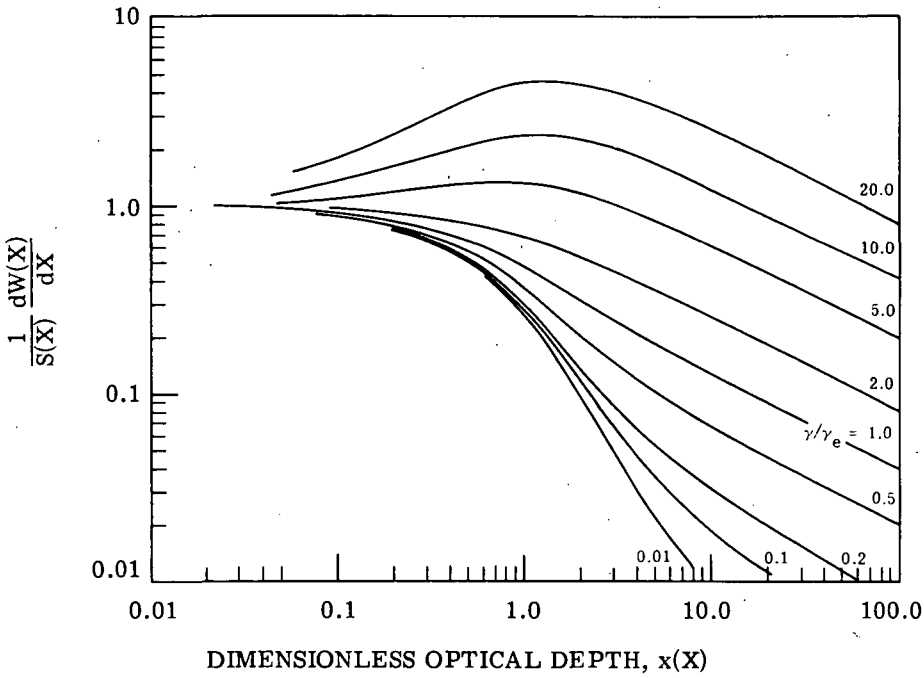

FIGURE 20. EQUIVALENT-WIDTH DERIVATIVE IN THE CURTIS-GODSON APPROXIMATION

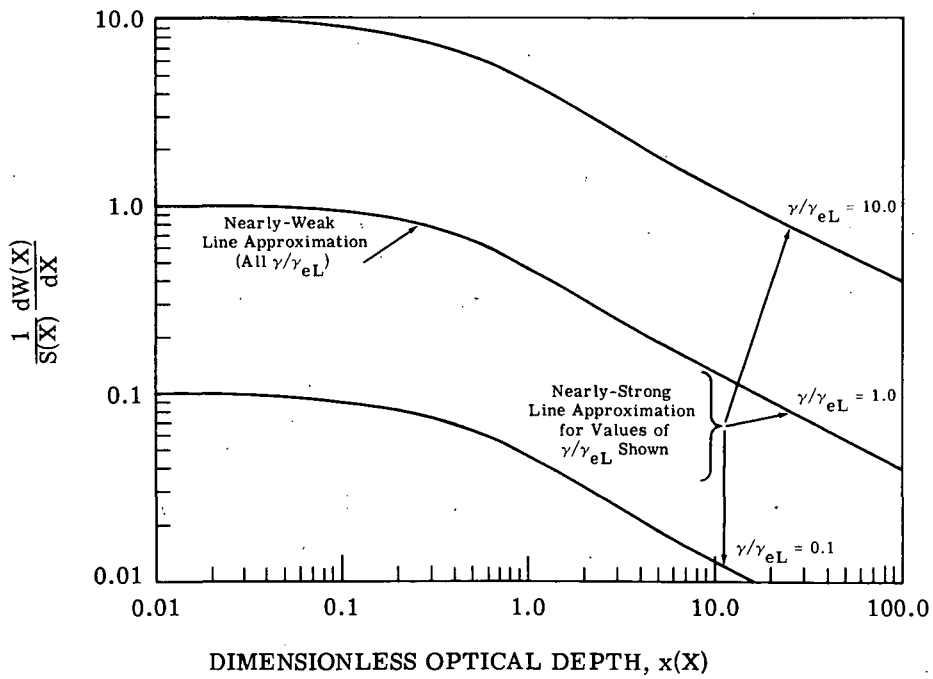

FIGURE 21. EQUIVALENT-WIDTH DERIVATIVE IN THE NEARLY-WEAK AND NEARLY-STRONG LINE APPROXIMATIONS

however, for the NS approximation, the quantity $[1/S(X)](dW/dX)$ becomes greater than one at small values of $\bar{x}$ for $\frac{\gamma(X)}{\gamma_{eL}} > 1$. This is accounted for by the proper choice of F(X'). However, we are left with no information upon which to base F(X') at this stage.

It appears that neither the NW-NS approximation (unless F(X) is accurately specified) nor the Curtis-Godson approximation give sufficiently accurate values for dW/dX over the full range of optical depths and for all possible values of γ/γ_e. On the other hand, it should be noted that the anomalies and errors in the curves for (1/S)(dW/dX) as given by the Curtis-Godson approximation are not serious as long as γ/γ_e never exceeds a value of about two. This condition exists [21, 22, 27] for most atmospheric paths but not for highly nonhomogeneous paths. For example, hot products of combustion viewed through long atmospheric paths yield values of γ/γ_e as large as 20 (Appendix III).

To obtain a more acceptable expression for dW/dX, consider the growth of an isolated spectral line. The equivalent width is given exactly by

$$W(X) = 1 - \int_{-\infty}^{\infty} \exp\left[-\int_0^X k(\Delta\nu, X')\,dX'\right] d(\Delta\nu) \tag{43}$$

and its derivative, in terms of a Lorentz profile, by

$$\frac{dW}{dX} = \frac{1}{\pi}\int_{-\infty}^{\infty} \frac{S(X)\gamma(X)}{\gamma^2(X) + (\Delta\nu^2)} \exp\left[-\frac{1}{\pi}\int_0^X \frac{S(X')\gamma(X')}{\gamma^2(X') + (\Delta\nu)^2}\,dX'\right] d(\Delta\nu) \tag{44}$$

where $\Delta\nu = \nu - \nu_o$. In the original treatment of the Curtis-Godson and the NW-NS approximations, the separation of frequency-dependent and path-dependent variables was accomplished by substitution of an effective value, γ_e, in both parts of the integrand. The only difference in our treatment from previous treatments is that we will use such an approximation only in the exponential term. Thus, in terms of $\gamma_e = \gamma_e(X)$ defined by Eq. (32) and x defined by Eq. (35), Eq. (44) becomes

$$\frac{dW}{dX} = \frac{1}{\pi}\int_{-\infty}^{\infty} \frac{S(X)\gamma(X)}{\gamma^2(X) + (\Delta\nu)^2} \exp\left[-2x\gamma_e(X)\frac{\gamma_e(X)}{\gamma_e^2(X) + (\Delta\nu)^2}\right] d(\Delta\nu) \tag{45}$$

This is equivalent to making a Curtis-Godson substitution in the expression for the derivative of W, rather than in the expression for W itself. The process of taking a derivative after an approximation has been made is reversed, a treatment which should be inherently better than the techniques described earlier for the calculation of radiances. This new approximation can be compared to the previous two if dW/dX is considered as the limiting value of the contribution

to W from a small element of path, ΔX, viewed through the path ahead of it. In the previous two approximations, the line shape of the element ΔX and the path in front of it are both given by the line shape for the equivalent, homogeneous path. In the current approximation we assumed that the element ΔX has its true line shape, while the path in front of it has an equivalent homogeneous shape. Equation (45), checked against the exact relation (Eq. 44), for a two-layer, nonisothermal path, has been found to be very accurate. Further investigation of its accuracy is to be the subject of future work. It would be possible to fully develop a procedure for treating isolated Lorentz lines. However, our interest is ultimately in a random band model which treats the average of many lines.

I.3. BAND-MODEL CONSIDERATIONS

The calculation of an average spectral radiance at the boundary of a radiating body of gas, in a frequency interval encompassing a number of rotational lines, is represented by the relation

$$\overline{L}_\nu = \int_0^\infty g(\nu' - \nu) L_\nu(\nu')\, d\nu' \tag{46}$$

where $g(\nu, \nu')$ is an averaging function (e.g., the slit function of a spectrometer of moderate resolution, such as those which produce original absorption spectra from which band-model parameters are extracted). The exact spectral radiance, L_ν, is given by the equation of transfer, Eqs. (21) and (23). Thus, Eq. (46) can be written

$$\overline{L}_\nu = \int_0^\infty g(\nu' - \nu) \int_1^{\tau(X_L)} L_\nu^*(\nu, \tau')\, d\tau'\, d\nu' \tag{47}$$

where τ is the perfectly resolved transmittance, and the primes denote variables of integration.

The order of integration in Eq. (47) can be inverted, and when frequency intervals are small enough that the Planck function is essentially constant, the result is the band-model expression:

$$\overline{L}_\nu(\nu) = \int_1^{\overline{\tau}(X_L)} L_\nu^*(\nu, \overline{\tau}')\, d\overline{\tau}' \tag{48}$$

where

$$\overline{\tau}(\nu) = \int_0^\infty g(\nu' - \nu)\tau(\nu')\, d\nu' \tag{49}$$

Thus, $\bar{\tau}$ is seen to be the spectral transmittance measured by a conventional instrument or calculated by a band-model.

Equation (49) can be evaluated to obtain the average spectral radiance, $\bar{L}_\nu$, by first computing $\bar{\tau}$ at a number of points along the path. The blackbody radiance is then represented as a function of $\bar{\tau}$, and integrated numerically over $\bar{\tau}$, with, for instance, the use of a simple summation. The various band models in current use, including those based on the Curtis-Godson approximation and the present model in its original form, do yield values for the transmittance with an accuracy sufficient for most engineering applications. However, as for the case of isolated lines, Eq. (49) involves a differentiation of the expression for $\bar{\tau}$ with respect to the optical path. Differentiation, of course, accentuates errors and uncertainties; in the isolated line case presented above, the derivative of the equivalent width exhibited the error. Therefore, an expression which yields reasonable values for $\bar{\tau}$ will not necessarily yield reasonable values for $d\bar{\tau}$ and, hence, for $\bar{L}_\nu$. It was necessary, therefore,to develop an expression for $\bar{\tau}$ which has a derivative which will yield more realistic values of the difference in transmittance with a specified incremental increase in physical path.

The transmittance for a band of spectral lines with some overlapping can be expressed as [21]

$$\bar{\tau} = \exp(\bar{\tau}_n - 1) \tag{50}$$

where $\bar{\tau}_n$ is the transmittance for an equivalent band of well-isolated nonoverlapping lines. Differentiation of Eq. (50) with respect to the optical depth, X, yields

$$\frac{d\bar{\tau}}{dX} = \bar{\tau}\frac{d\bar{\tau}_n}{dX} \tag{51}$$

which indicates that, with a reasonably accurate value for $\bar{\tau}$, the accuracy of $d\bar{\tau}/dX$ depends directly on the accuracy of $d\bar{\tau}_n/dX$.

In our current work, we have used the NW-NS approximation exclusively and at this point our consideration is limited to this model to find specification of the function F(X') which yields accurate values of a transmittance derivative. For the NW-NS approximation [5]

$$\bar{\tau}_n = \beta_{eL} f(\bar{x}) \tag{52}$$

where the argument of the Ladenburg-Reiche function is, in this case ,

$$\bar{x}(X) = \frac{1}{\beta_{eL}}\int_0^X \bar{k}(X')\left[\frac{\beta(X')}{\beta_{eL}}\right]^{\eta(X')} dX' \tag{53}$$

in which $\bar{k} = \bar{k}(\nu, T)$ is the first band-model parameter, the average absorption coefficient, identified as the average line strength to spacing ratio, and $\beta = \beta(\nu, T)$ is the second band-model parameter, the line-overlap factor, identified as 2π times the average line width to spacing ratio. The effective value β_{eL} is defined analogously to γ_{eL} for the case of a single line:

$$\beta_{eL} = \frac{\int_0^{X_L} \bar{k}(X')\beta(X')\,dX'}{\int_0^{X_L} \bar{k}(X')\,dX'} \tag{54}$$

$F(X')$ has here been replaced by $[\beta(X')/\beta_{eL}]^{\eta(X')}$, a suitable functional form for $F(X')$. Here η is an interpolation parameter between the nearly weak and nearly strong approximations, varying from 0 for the nearly weak to 1 for the nearly strong.

In an earlier study [5], an investigation of the form for η is described. As a result of that study, several reasonably useful empirical forms for η were determined. However, the information used to make these determinations was not sensitive enough to values of η to provide accurate information about its form. One of these empirical forms is:

$\eta = 0$ for $\bar{x} < 1$
$\eta = (\bar{x} - 1)/9$ for $1 \le x \le 10$
$\eta = 1$ for $\bar{x} > 10$

This appears to make η a function of $\bar{x}$ rather than X', and the determination of $\bar{x}$ appears as an iterative procedure. However, in practice the integral for $\bar{x}$ is evaluated by a summation, and a value for η for a particular term is determined from the value for $\bar{x}$ calculated from the sum of the preceding terms. Thus, η is uniquely defined for each X'.

Differentiation of Eq. (52) and utilization of Eq. (54) yields

$$\frac{d\bar{\tau}_n}{dX} = \frac{df}{d\bar{x}}\left[\frac{\beta(X)}{\beta_{eL}}\right]^{\eta(X)}\bar{k}(x) \tag{55}$$

which shows that the derivative of $d\bar{\tau}_n/dX$ varies with the absorption coefficient (as would be expected), the derivative of the function $f(\bar{x})$, and the local values of $\beta(X)$ and $\eta(X)$. The physical significance of Eq. (55) can be seen in Fig. 22, a normalized plot of $-(1/\bar{k})\,d\bar{\tau}_n/dX$ versus x, with β/β_{eL} as a parameter. In the limit, as $x \to 0$, the band model reduces to a linear growth law, so that $-(1/\bar{k})\,d\bar{\tau}_n/dX$ approaches unity. This function must be less than unity for all values

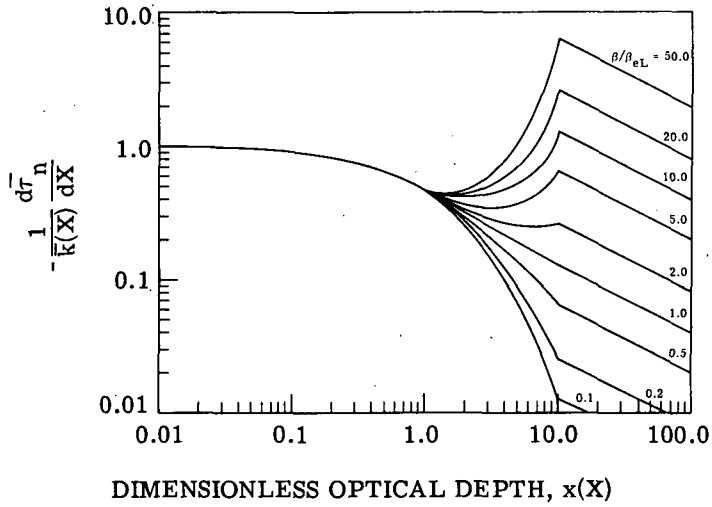

FIGURE 22. TRANSMITTANCE DERIVATIVE IN THE ORIGINAL BAND MODEL

of X greater than zero, as the square root growth law becomes operative. However, Fig. 3 shows that the empirical specifications for η do not conform to this requirement for certain values of β/β_{eL} and $\bar{x}$, an inconsistency analogous to that shown earlier for isolated line growth. $d\bar{\tau}_n/dx$ is correctly given by [21]

$$\frac{d\bar{\tau}_n}{dX} = -\frac{1}{\delta} \cdot \frac{d\bar{W}}{dX} \tag{56}$$

where $\bar{W}$ is an average equivalent width and δ is an average line spacing in the spectral interval under consideration. For lines of equal strength and width, after some rearrangement, Eqs. (56) and (45) yield

$$\frac{d\tau_n}{dX} = -\frac{1}{\pi}\int_{-\infty}^{\infty} \frac{\bar{k}(X)\beta(X)}{\beta^2(X) + (2\pi\Delta\nu/\delta)^2} \exp\left[-2x\beta_e(X)\frac{\beta_e(X)}{\beta_e^2(X) + (2\pi\Delta\nu/\delta)^2}\right] d\left(\frac{2\pi\Delta\nu}{\delta}\right) \tag{57}$$

where x denotes the dimensionless optical depth as defined in Eq. (35) and used in Eq. (45). Rewritten in terms of the two bandmodel parameters,

$$x = \frac{\int_0^X \bar{k}(X')\,dX'}{\beta_e(X)} \tag{58}$$

where $\beta_e(X)$ is the average value of the second band-model parameter over the path from the observer to the point X, similar to the definition of $\gamma_e(X)$ in Eq. (32)

$$\beta_e(X) = \frac{\int_0^X \bar{k}(X')\beta(X')\,dX'}{\int_0^X \bar{k}(X')\,dX'} \tag{59}$$

The distinction between β_{eL} (a constant determined over the whole path), defined in Eq. (54) and $\beta_e(X)$ (a function of X, the optical depth coordinate) should be noted.

The change of variables $\tan\theta/2 = 2\pi(\Delta\nu/\beta_e\delta)$ and a trigonometric substitution yields

$$-\frac{1}{\bar{k}(X)} \cdot \frac{d\bar{\tau}_n}{dX} = \frac{2}{\pi}\frac{\beta}{\beta_e}\int_0^{\pi} \frac{\exp\left[-x(1+\cos\theta\right]}{\left[\left(\frac{\beta}{\beta_e}\right)^2 + 1\right] + \left[\left(\frac{\beta}{\beta_e}\right)^2 - 1\right]\cos\theta}\,d\theta \tag{60}$$

Equation (60) has been integrated numerically; the results are plotted in Fig. 23, as $-(1/\bar{k})d\bar{\tau}_n/dX$ versus x; $\beta(X)/\beta_e(X)$ is the parameter. The resulting curves exhibit none of the anomalies seen in Fig. 22; the curve for $\beta/\beta_e = 1$ is identical in both figures.

The interpolation parameter, η, can now be evaluated by equating Eqs. (60) and (55). These two equations involve different sets of variables, i.e., Eq. (60) is given in terms of x and $\beta_e(X)$, and Eq. (55) is given in terms of $\bar{x}$ and β_{eL}. The relationship between $\bar{x}$ and x is complex and depends on η, $\beta_e(X)$ and β_{eL} in an integral form. Furthermore, although x is a unique function of the optical path extending from 0 to X, $\bar{x}$ is not a unique function in the same sense, since it depends on the path between X and X_L through β_{eL} as well. Such dependence is not physically realistic but appears as an integral part of the NW-NS approximation. In determining a form for η, this dependence must be accounted for so that the computed value of $(1/\bar{k})(d\tau_n/dX)$ is unique despite the nonunique character of $\bar{x}$, although this is very difficult to insure, except for certain types of paths. In particular, if β differs significantly from its average value, β_{eL}, in only a very small portion of the optical path, then the contribution from that portion of the path to the integral defining $\bar{x}$ is negligible compared to the contributions from the remainder of the path. In this case, the following approximate relation holds:

$$\int_0^X \bar{k}(X')\left[\frac{\beta(X')}{\beta_{eL}}\right]^{\eta(X')} dX' \simeq \int_0^X \bar{k}(X')\,dX'$$

The above restriction also implies that

$$\beta_e(X) = \text{constant} = \beta_{eL}$$

and that

$$x \simeq \bar{x}$$

Thus, if $\beta_e(X)$ is not a strong function of X and if large variations in $\beta(X)$ are allowed in very small fractions of the optical path only, values for η can be found in terms of $\bar{x}$ and β/β_{eL} (except for $\beta/\beta_{eL} = 1$ where η is indeterminate). The resultant values of η are shown in Fig. 24. Use of these values in Eq. (55) will insure that the derivative $d\bar{\tau}/dX$ will equal that given by Eq. (60). For convenience in application, we made simple analytical approximations to the curves of Fig. 24 by fitting them with functions as follows:

$$\eta(\bar{x}, \beta/\beta_e) = \frac{\bar{x} + A_1(\beta/\beta_e)}{\bar{x} + A_2(\beta/\beta_e)} \qquad (61)$$

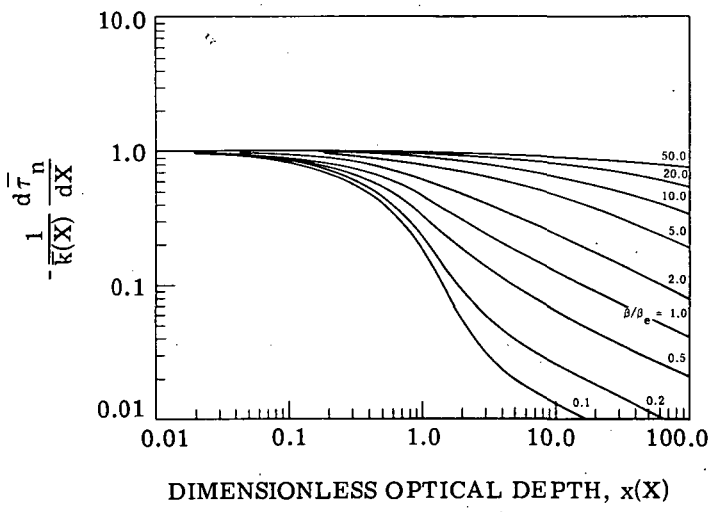

FIGURE 23. TRANSMITTANCE DERIVATIVE IN THE MODIFIED BAND MODEL

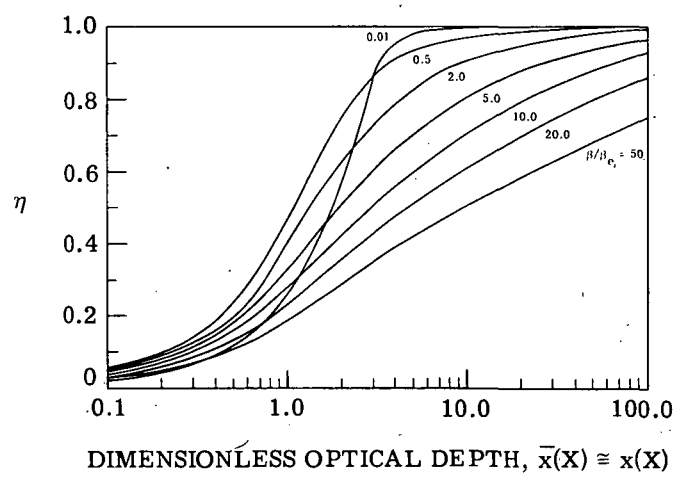

FIGURE 24. INTERPOLATION PARAMETER AS A FUNCTION OF OPTICAL DEPTH AND LINE-OVERLAP FACTOR

$$\eta(\bar{x}, \beta/\beta_e) = \frac{\bar{x}A_3(\beta/\beta_e)}{A_5(\beta/\beta_e) + \bar{x}A_4(\beta/\beta_e)} \tag{62}$$

For any particular instance, the choice between Eqs. (61) and (62) is made on the basis of the quantity

$$A_5(\beta/\beta_e) = 1 + 0.185\,\beta/\beta_e \tag{63}$$

If $\bar{x} > E$, Eq. (61) is used; otherwise Eq. (62) is used. Values for A_1, A_2, A_3, and A_4 are tabulated in Table 11. Values of $d\bar{\tau}_n/dX$ obtained when the values in Table 11 are used in place of the values shown for η in Fig. 5 are sufficiently accurate for most applications of this band-model.

The limitation on the variation of $\beta(X)$ and $\beta_e(X)$ mentioned earlier is not as severe as it might first appear. For instance, in cases where a relatively small hot gaseous source is to be viewed through a long, cool path, the value of β is almost invariant over the whole atmospheric path which contains the largest part of the optical path. Only in the relatively small portion of the path comprising the hot gaseous source does β vary substantially.

The introduction of an interpolation parameter has little physical basis and is not the only way Eq. (60) could be introduced into a computational procedure. An alternative method for use of the above results would be the direct application of Eq. (60) into a band-model computer code. The resultant values of $d\bar{\tau}_n/dX$ could then be used in Eq. (51), if $\bar{\tau}_n$ in Eq. (50) is evaluated in terms of x and $\beta_e(X)$. Such a procedure would eliminate the need for a distinction between the NW and NS approximations and, therefore, eliminate an interpolation procedure. Unfortunately, when Eq. (60) is used, an analytic form for the solution of the integral is not easily obtained. Although a solution has been obtained in the form of an infinite series, this represents little improvement over a table of numerical values. Whether there would be a net gain in computational efficiency remains to be seen. However, a direct application of Eq. (60) might be expected to be somewhat more satisfactory because the restriction on the variation of $\beta_e(X)$ compared to β_{eL} required in the evaluation of η would not be needed. This alternative mode of the band-model formulation is one of the subjects of a continuing investigation.

In summary, we have shown how both the Curtis-Godson approximation and the NW-NS approximation can introduce anomalies into the radiance computed over a highly nonisothermal path for an isolated spectral line. The application of a Curtis-Godson approximation to the expression for the equivalent-width gradient along the path produced a formulation yielding greatly improved radiance values which exhibit no anomalies. In the generalization to a random band model, the expression concerning the equivalent-width gradient has been used to obtain an interpolation between the nearly-weak and nearly-strong approximations valid for that band model.

The most important result presented herein is the form of the transmittance gradient given in Eq. (60). It is the basis of a computational procedure for computing the radiance from highly nonisothermal gaseous sources. This procedure yields significant improvements over previously used techniques. It has been shown to be a better approximation than those more commonly used and yields physically realistic results for all values of the path and band-model parameters.

TABLE 11. COEFFICIENTS TO BE USED IN EQS. (61) AND (62)

β/β_e	A_1	A_2	A_3	A_4
0	-0.68	-0.35	0.55	0.07
2	-0.37	0.62	0.71	0.43
5	0.60	3.15	0.90	0.79
10	3.19	9.25	1.15	1.30
20	9.10	22.8	1.63	2.26
50	29.1	67.1	2.78	4.56
100	105	209	4.05	7.09

Appendix II
COMPARISON OF THE MODIFIED BAND MODEL WITH OBSERVED HOT GAS SPECTRA

The measured spectra in Figs. 25 through 30 are those of furnace-heated gas samples, 60-cm long, obtained in the previous study [1]. We obtained the band-model predictions (the less detailed spectra in each figure) using Eqs. (1) and (2), modified as indicated in Appendix I.

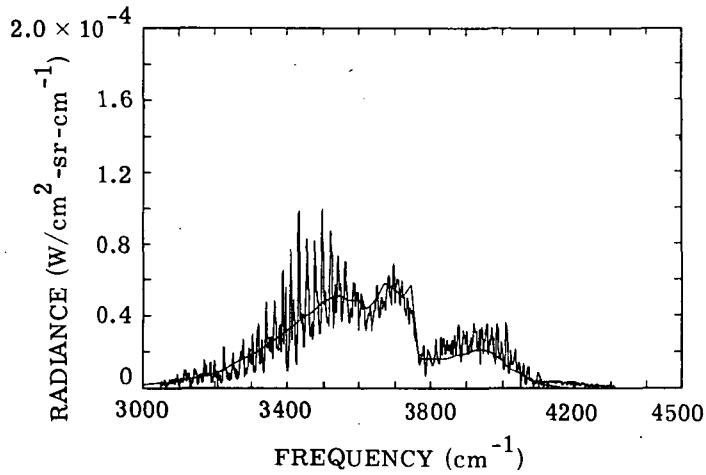

FIGURE 25. SPECTRAL RADIANCE, RUN 10216807. Gas: $H_2O/CO_2/N_2$; P = 57, 28, 675 mm; temperature (^oK) = 378, 537, 723, 958, 1127, 1158, 990, 752, 555, 383.

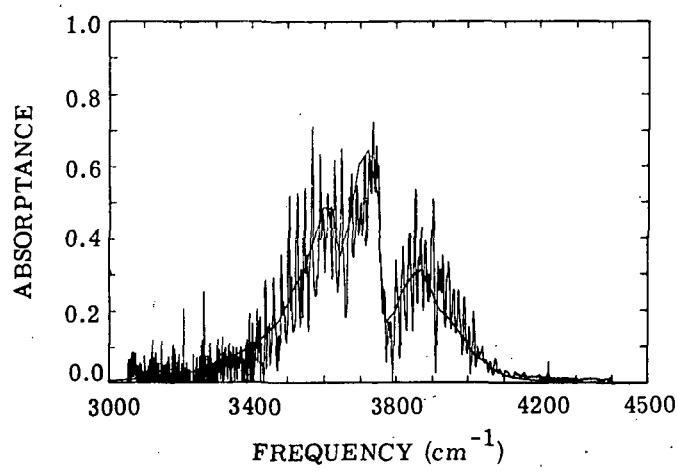

FIGURE 26. SPECTRAL ABSORPTANCE, RUN 10216807. Gas: $H_2O/CO_2/N_2$; P = 57, 28, 675 mm; temperature (^oK) = 378, 537, 723, 958, 1127, 1158, 990, 752, 555, 383.

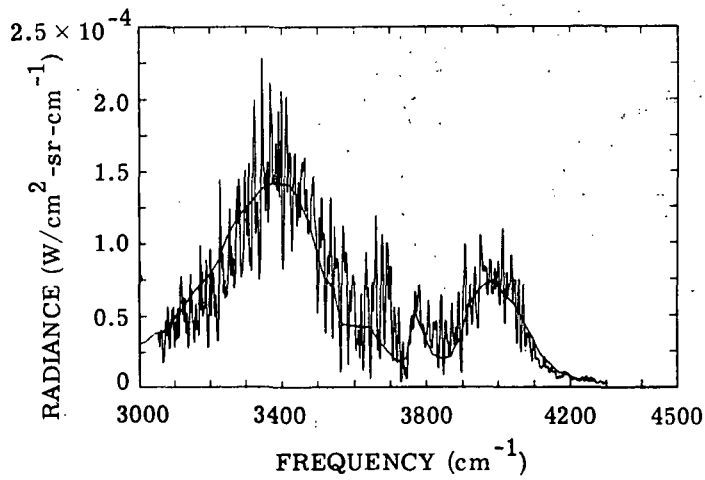

FIGURE 27. SPECTRAL RADIANCE, RUN 10216811. Gas: H_2O; P = 670 mm; temperature (^oK) = 382, 537, 723, 953, 1128, 1160, 990, 751, 558, 389.

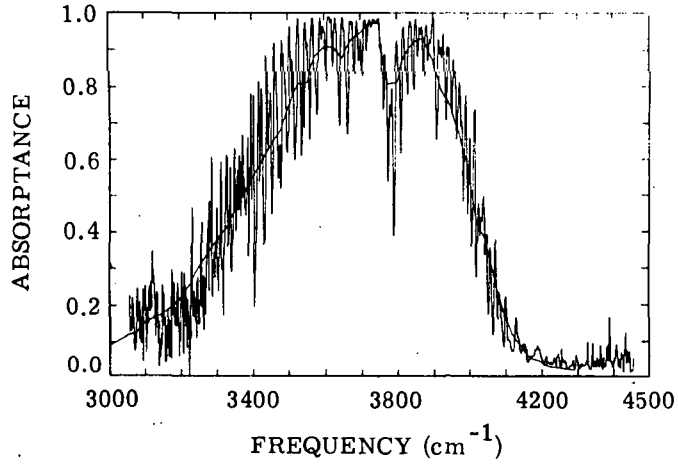

FIGURE 28. SPECTRAL ABSORPTANCE, RUN 10216811.
Gas: H_2O; P = 670 mm; temperature (^oK) = 382, 537, 723, 953, 1128, 1160, 990, 751, 558, 389.

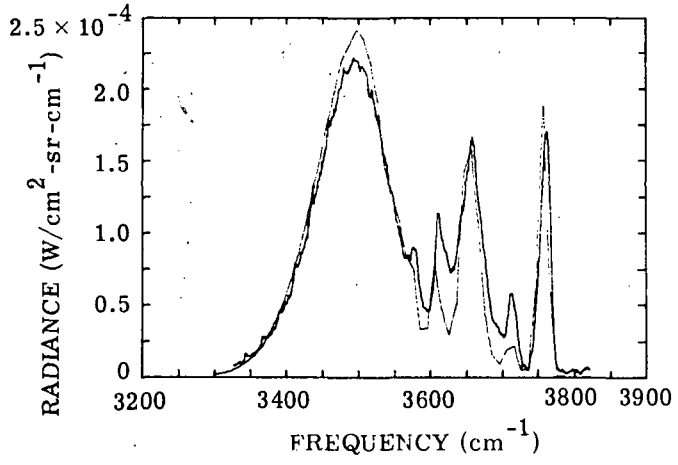

FIGURE 29. SPECTRAL RADIANCE, RUN 10216812.
Gas: CO_2; P = 760 mm; temperature (^oK) = 386, 528, 719, 953, 1130, 1160, 979, 737, 541, 387.

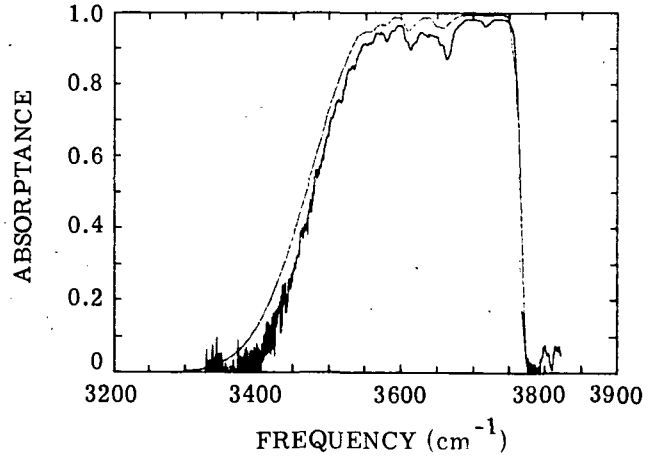

FIGURE 30. SPECTRAL ABSORPTANCE, RUN 10216812.
Gas: CO_2; P = 760 mm; temperature (^oK) = 386, 528, 719, 953, 1130, 1160, 979, 737, 541, 387.

Appendix III
CALCULATION OF RADIATION FROM HOT H_2O AND CO_2 VIEWED THROUGH A COOL INTERVENING ATMOSPHERE

There are a number of engineering problems requiring quantitative calculations of the thermal emission from hot water vapor and carbon dioxide, viewed through atmospheric paths in which these species also appear as absorbers. In recent years, molecular band models, originally developed for atmospheric transmission calculations, have been extended to handle the case of inhomogeneous bodies of hot gases which emit as well as absorb. This appendix is concerned with their further extension to the case of a hot body of gas imbedded in a cool atmosphere, treated as a single radiative-transfer problem. The computational method is illustrated by a comparison of predicted and observed spectra in the 2.7-μm region for a small methane-oxygen flame.

The arrangements for the illustrative experiment were as follows: the flames were generated with a multiple-diffusion burner originally built for hydrogen-fluorine combustion [11]; it operated equally well with methane and oxygen. The burner was installed in the sample beam of the double-beam spectrometer described in [1]. An auxiliary system of mirrors, two diagonals and a sphere, provided for measurements of spectral radiance and absorptance of the flame viewed directly and through a 10.32-m path of ambient air; with the flame extinguished, the absorptance of the atmospheric path alone could also be measured. The observed spectral radiance in the 2.7-μm region of a stoichiometric CH_4/O_2 flame with and without an intervening atmospheric absorption are shown in Fig. 31. The extreme wings of the flame emission band, comprised primarily of lines originating from higher rotational levels, are relatively unattenuated, in contrast with the central region in which the low temperature atmospheric absorption is encountered. This characteristic shape for a a vibration-rotation band of a highly nonisothermal path is perfectly analogous to the familiar shape of a self-reversed spectral line under corresponding conditions.

For the band-model calculations, a flame model, similar to that used in [11], consisted of an isothermal core and a mixing region in which temperature and the concentration of the combustion products decreased parabolically, as the result of dilution with ambient air, as shown in Fig. 32. However, in this case, recombination of two dissociated species, H_2O and CO_2, had to be accounted for. In order to avoid a detailed equilibrium calculation for all species concentrations at each local value of temperature in the mixing region, the assumption was made that the reactions occur independently:

$$1/2H_2 + OH \rightleftharpoons H_2O \tag{64}$$

$$1/2O_2 + CO \rightleftharpoons CO_2 \tag{65}$$

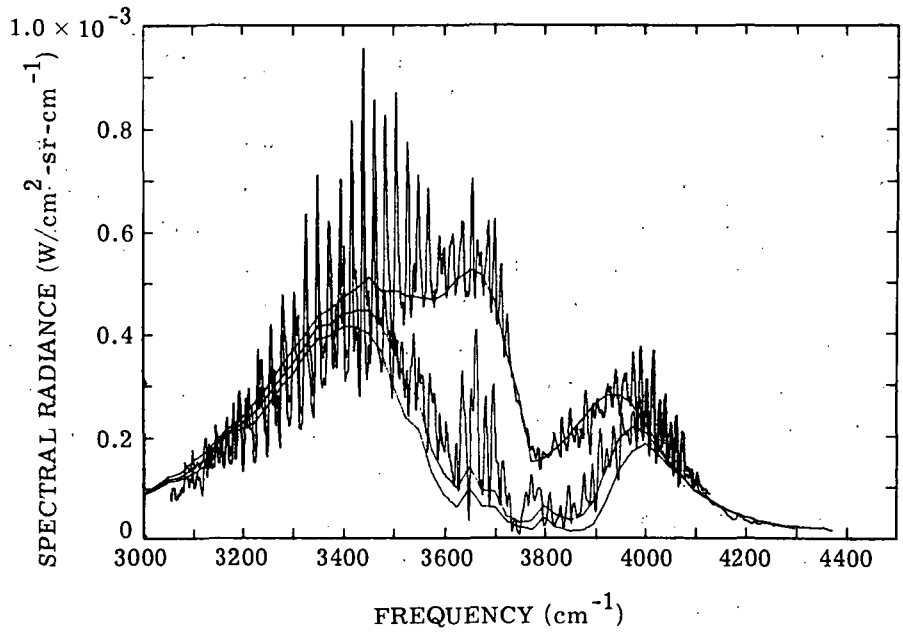

FIGURE 31. OBSERVED AND PREDICTED SPECTRA FOR A 2.5-cm DIAMETER CH_4/O_2 FLAME VIEWED DIRECTLY AND THROUGH A 10-m PATH. The smoother curves are the band-model predictions; the upper curve is the flame alone; the lower curve is the flame and atmospheric path; the middle is the product of flame radiance and atmospheric transmittance which have been calculated separately.

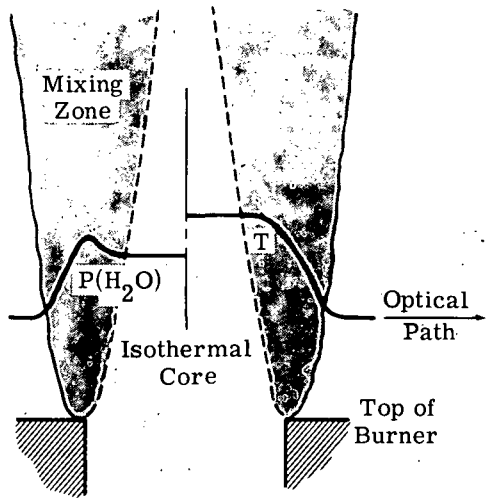

FIGURE 32. MODEL FOR FLAME STRUCTURE

This permitted the approximations $P(OH) \approx 2P(H_2)$ and $P(CO) \approx 2P(O_2)$ which, combined with the definitions for the equilibrium constants and the over-all reaction equation, provided the relations

$$P(H_2O) = 0.667 - 3[K_1 P(H_2O)/2]^{2/3} \tag{66}$$

$$P(CO_2) = 0.333 - 3[K_2 P(CO_2)/2]^{2/3} \tag{67}$$

Equations (66) and (67) were solved numerically at each temperature, with values for the equilibrium constants, $K = K(T)$, given in [27].

As inputs to the flame model, the core temperature, T_c, was taken as that measured in the center of a comparable CH_4/O_2 flame by a sodium line-reversal technique; the core radius r_c/R was evaluated in accordance with the well-known properties of turbulent mixing of jets discharging into a quiescent medium [28]. The resultant values, $T_c = 2800^{\circ}K$ and $r_c/R = 0.74$, were then used in the band-model calculations of the spectral radiance of the flame viewed directly and through the atmospheric path. The resultant band-model predictions, shown in Fig. 31 as the upper and lower smooth curves, compare favorably with the observed spectra.

Also shown in this figure, the middle smooth curve is the product of the flame radiance and atmospheric transmittance calculated separately. This procedure is incorrect in principle, since an atmospheric transmittance factor, calculated with such a band-model formulation (or for that matter determined experimentally by conventional techniques), refers to the attenuation of a spectrally continuous source. In this case, the hot gaseous source is spectrally discontinuous, with a high degree of correlation in spectral line content with that of the absorbing atmosphere. Hence, except for spectral regions in which lines are so close as to completely overlap, the application of an atmospheric transmittance factor, so determined, results in an overestimate of the radiance at a distant point. For the relatively short atmospheric path in the example shown, the two methods yield results that do agree to within the experimental error of the measurements. However, these effects become more pronounced at longer ranges. To illustrate, a set of calculations was made for the spectral radiance of a hypothetical source 1 m in diameter with a parabolic profile varying from $1200^{\circ}K$ in the center to $300^{\circ}K$ at the boundary, and a corresponding composition profile based on a reasonable mixture of combustion products of methane in air, observed at ranges of 10, 100, and 1000 m through a standard sea-level atmosphere at 50% relative humidity. The results are shown in Fig. 33, in which the upper curves are the radiance spectra of the hot source with no atmospheric absorption; the lower and middle curves are the apparent radiances at the indicated ranges, respectively calculated by the correct and incorrect procedure. It is clear that in selected spectral bandpasses, the apparent radiance would be lower by an order of magnitude or more than the product of the actual radiance and atmospheric transmittance.

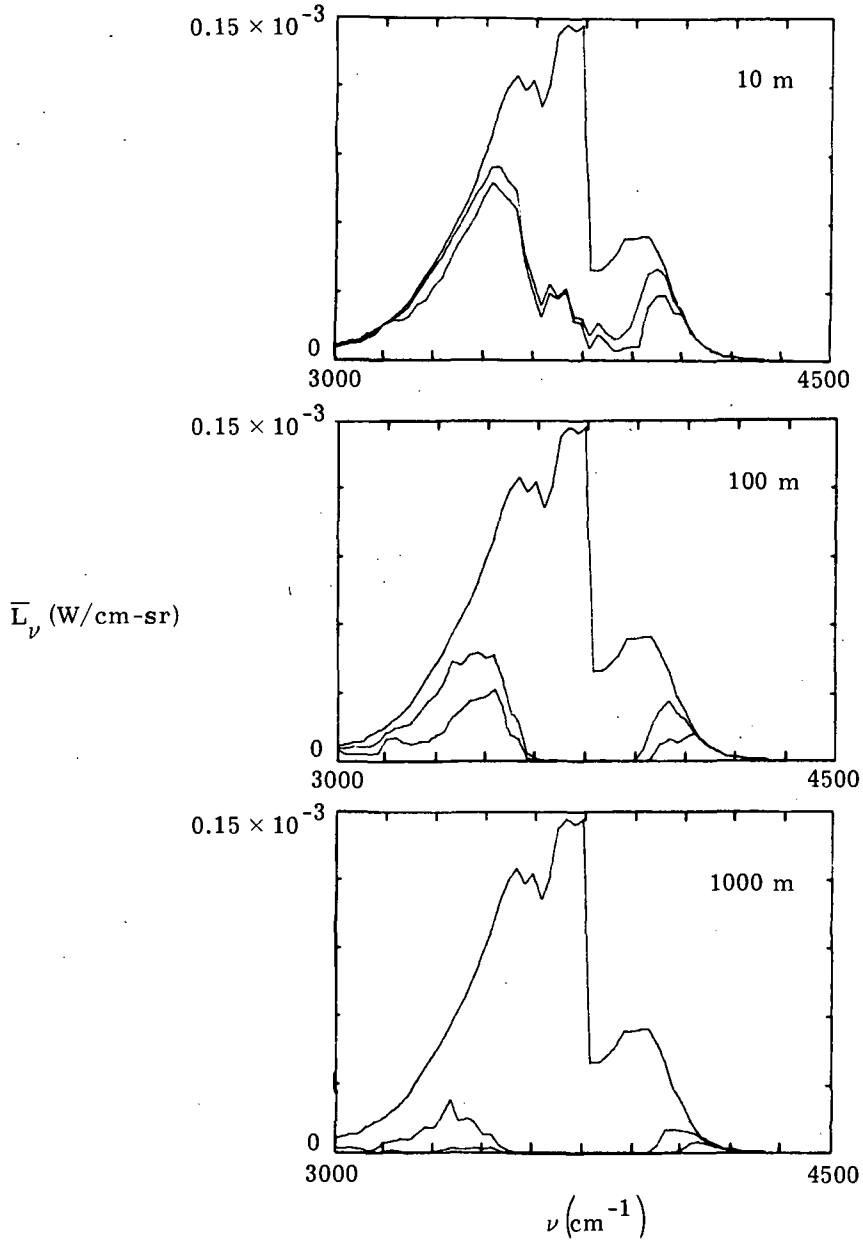

FIGURE 33. APPARENT SPECTRAL RADIANCE OF A HOT SOURCE VIEWED THROUGH VARIOUS ATMOSPHERIC PATHS. The upper curves represent the hot source alone; the lower curves represent the combined hot source and atmospheric path; the middle curves show the product of the hot source radiance and atmospheric transmittance which have been calculated separately.

This appendix indicates the importance of the proper treatment of the apparent radiance distribution or spectral radiant intensities of distant hot combustion-product sources viewed through the atmosphere. The hot-gas band model developed under this and preceding contracts does provide a basis for such treatment, and is currently in use in various studies of rocket and jet-engine exhaust radiation.

Appendix IV
BAND-MODEL PARAMETERS FOR LOW TEMPERATURES

The values of the band-model parameters in this study were extracted from the General Dynamics tabulations [4]. These parameters were determined from the analysis of spectral absorptances of isothermal samples of hot gases and are reasonably reliable throughout the temperature range of the original measurements. However, the tabulations were extended down to 300°K by extrapolation. When these values were used in the present band model for the estimation of transmittances in atmospheric paths at some wavelengths, the results were in considerable disagreement with calculations made with the atmospheric transmission models and parameters described by Anding [29].

Since the latter have been demonstrated to be reliable over large ranges of atmospheric paths, horizontal and slant, the parameters in the hot gas band model were adjusted until a satisfactory agreement was achieved. Figure 34 shows the results of this adjustment for a 29.2-km slant path through a standard atmosphere; the path parameters are listed in Table 12. Figure 35 shows a comparison of the two models applied to a path which has the same temperature and pressure profiles, but which is shorter by a factor of 100.

TABLE 12. PATH PARAMETERS IN THE HOT GAS BAND MODEL

Distance (cm)	Temperature (°K)	$P(H_2O)$ (atm)	$P(CO_2)$ (atm)	$P(N_2)$ (atm)
0	288.0	0.956E-2	0.32E-3	1.0
2.92E5	281.7	0.676E-2	0.277E-3	0.886
5.86E5	275.2	0.399E-2	0.252E-3	0.785
8.7E5	268.7	0.244E-2	0.222E-3	0.693
1.17E6	266.2	0.155E-2	0.195E-3	0.609
1.462E6	255.7	0.612E-3	0.171E-3	0.535
2.93E6	223.3	0.117E-4	0.063E-3	0.199

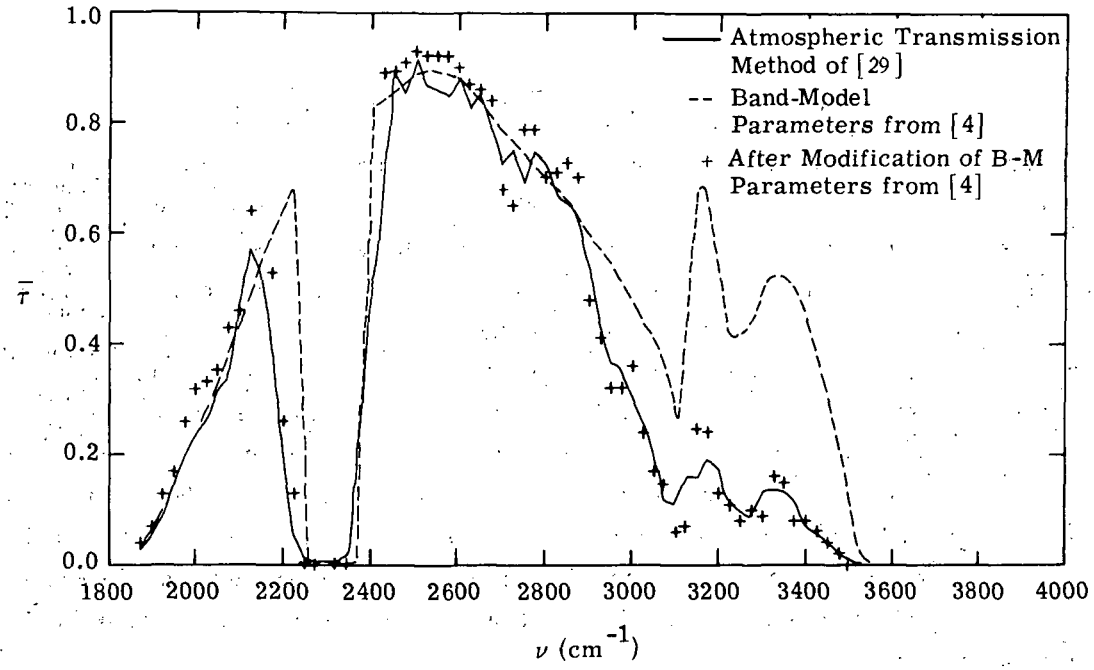

FIGURE 34. TRANSMITTANCES FOR A 29.3-km ATMOSPHERIC PATH

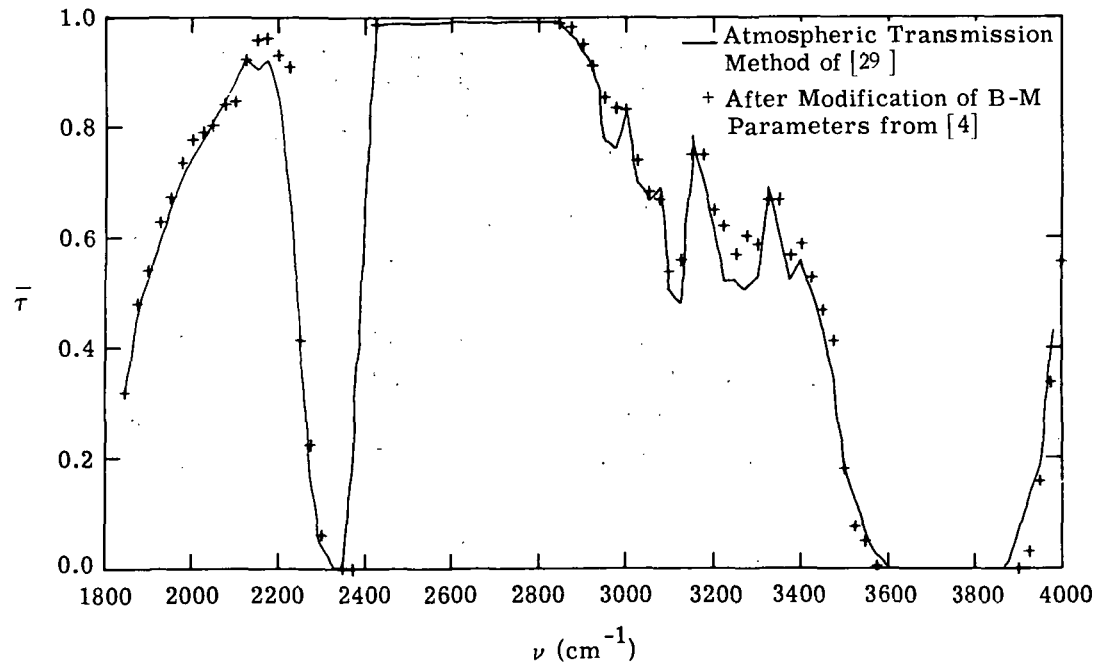

FIGURE 35. TRANSMITTANCES FOR A 0.293-km ATMOSPHERIC PATH

Appendix V
ULTRAVIOLET EMISSION AND ABSORPTION SPECTRA

In Figs. 36 through 40 ultraviolet emission and absorption spectra are shown that were obtained for the 5 burner profiles (shown in Figs. 10 through 15). On all absorption curves, the absorption zero is determined from the local position of the trace between lines, and full absorption is taken to be the lower limit of the chart. On emission spectra, emission zero is the lower limit of the chart. The radiance calibration curve shown on each emission trace is the trace obtained from the corresponding observation of the spectral radiance standard lamp. The calibration curve shown must be divided by the calibration gain factor shown on each emission spectrum in order for the emission spectrum and the calibration curves to be comparable. (The radiance of the standard lamp was always much less than the radiance of the flame in the OH lines.) The radiance values of the standard lamp as determined by NBS, interpolated to the frequencies of the seven OH lines considered are given in Table 13. In the data reduction, these values were reduced by a factor of 0.92 to account for reflection losses in the lens between the lamp and the measurement system.

TABLE 13. SPECTRAL RADIANCE VALUES FOR THE SPECTRAL RADIANCE STANDARD LAMP

Line	Frequency (cm^{-1})	Spectral Radiance ($\mu W/cm^2\text{-}sr\text{-}cm^{-1}$)
$R_2 1$	32415.5	0.349
$R_2 3$	32489.5	0.337
$R_2 4$	32517.6	0.333
$R_2 7$	32572.6	0.324
$R_2 14$	32551.7	0.327
$R_2 15$	32531.8	0.331
$R_2 20$	32363.5	0.358

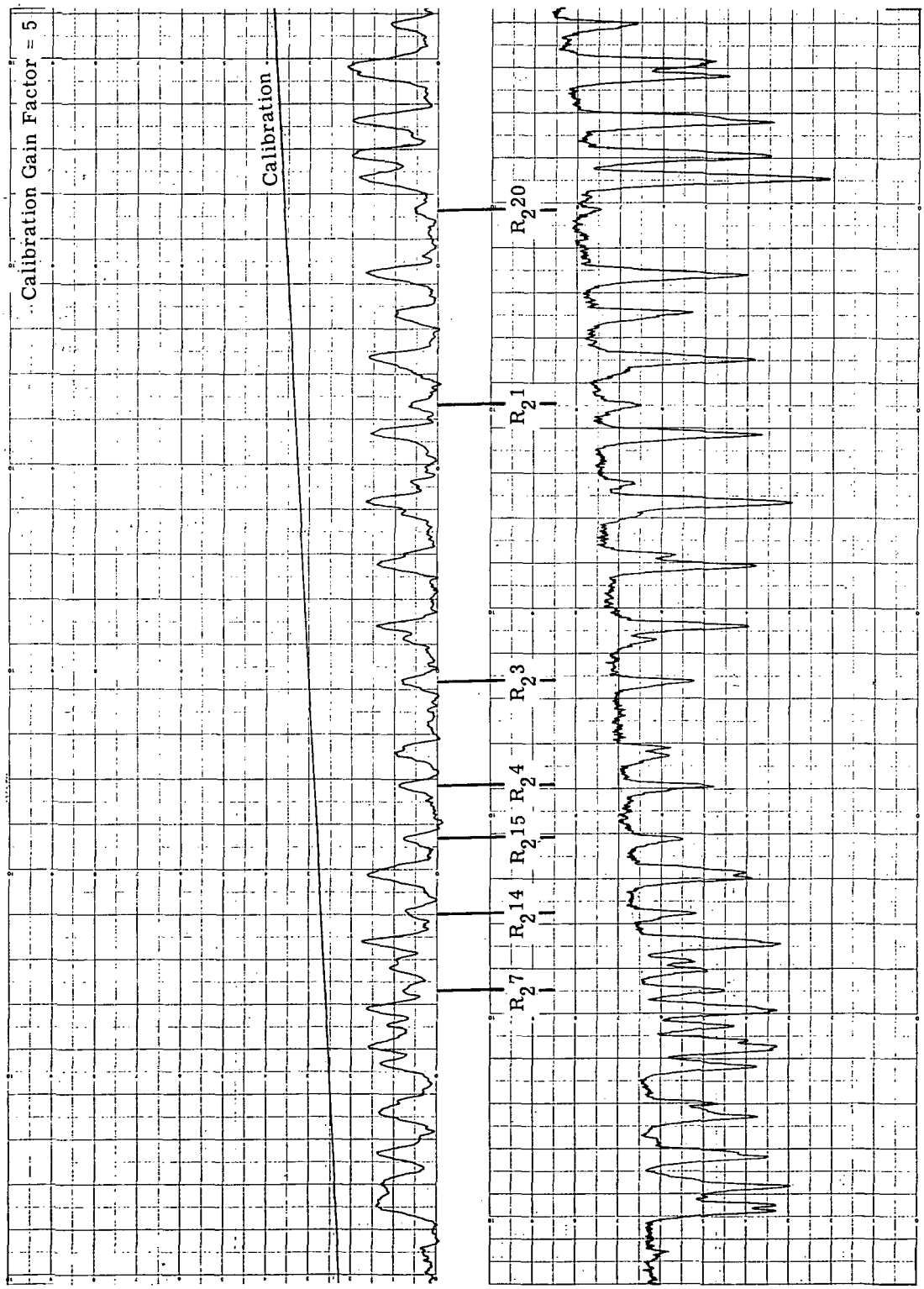

FIGURE 36. ULTRAVIOLET SPECTRA, PROFILE A: LINEAR (HOT THROUGH COLD)

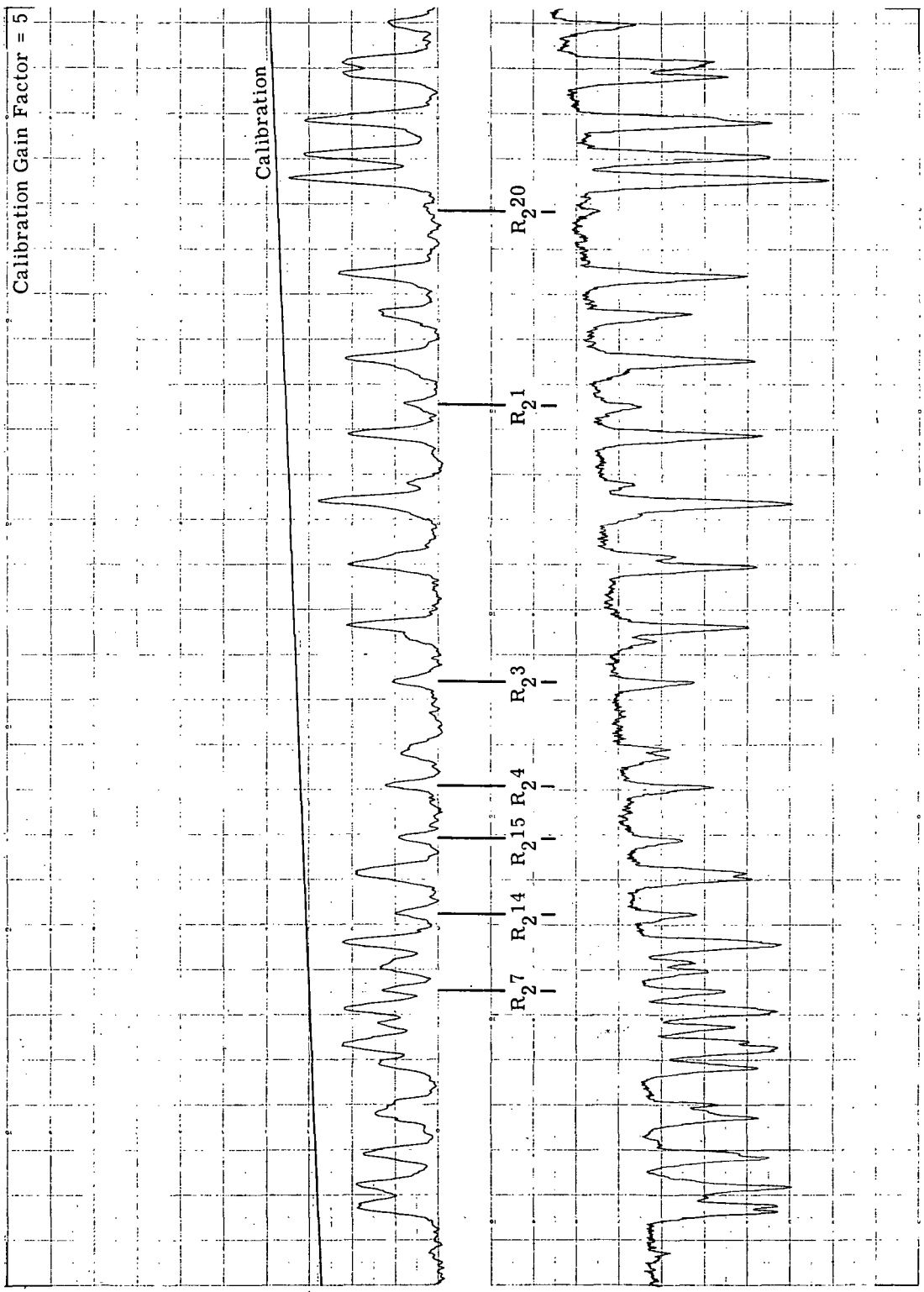

FIGURE 37. ULTRAVIOLET SPECTRA, PROFILE B: LINEAR (COLD THROUGH HOT)

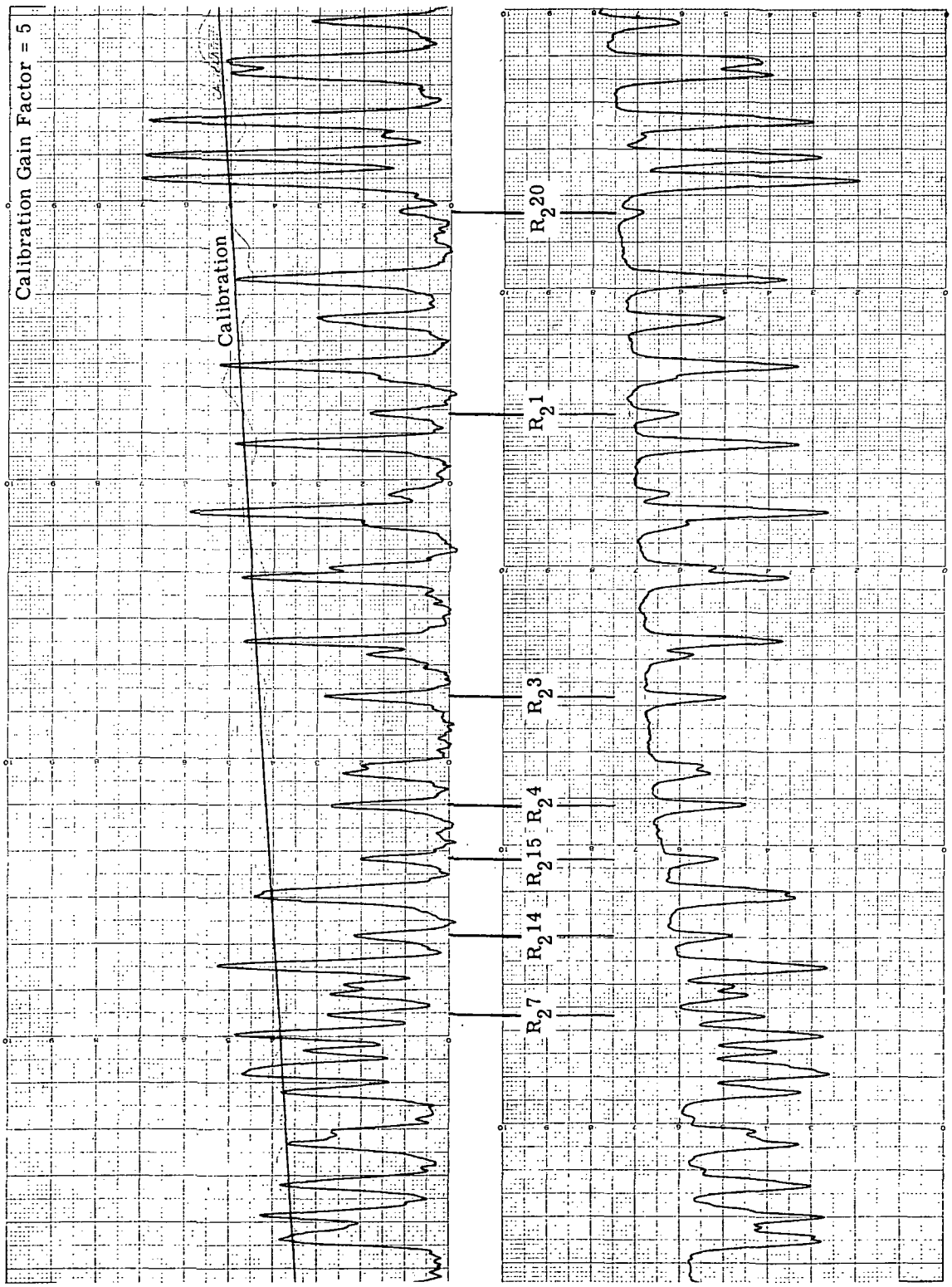

FIGURE 38. ULTRAVIOLET SPECTRA, PROFILE C: TRIANGULAR (HOT CENTER)

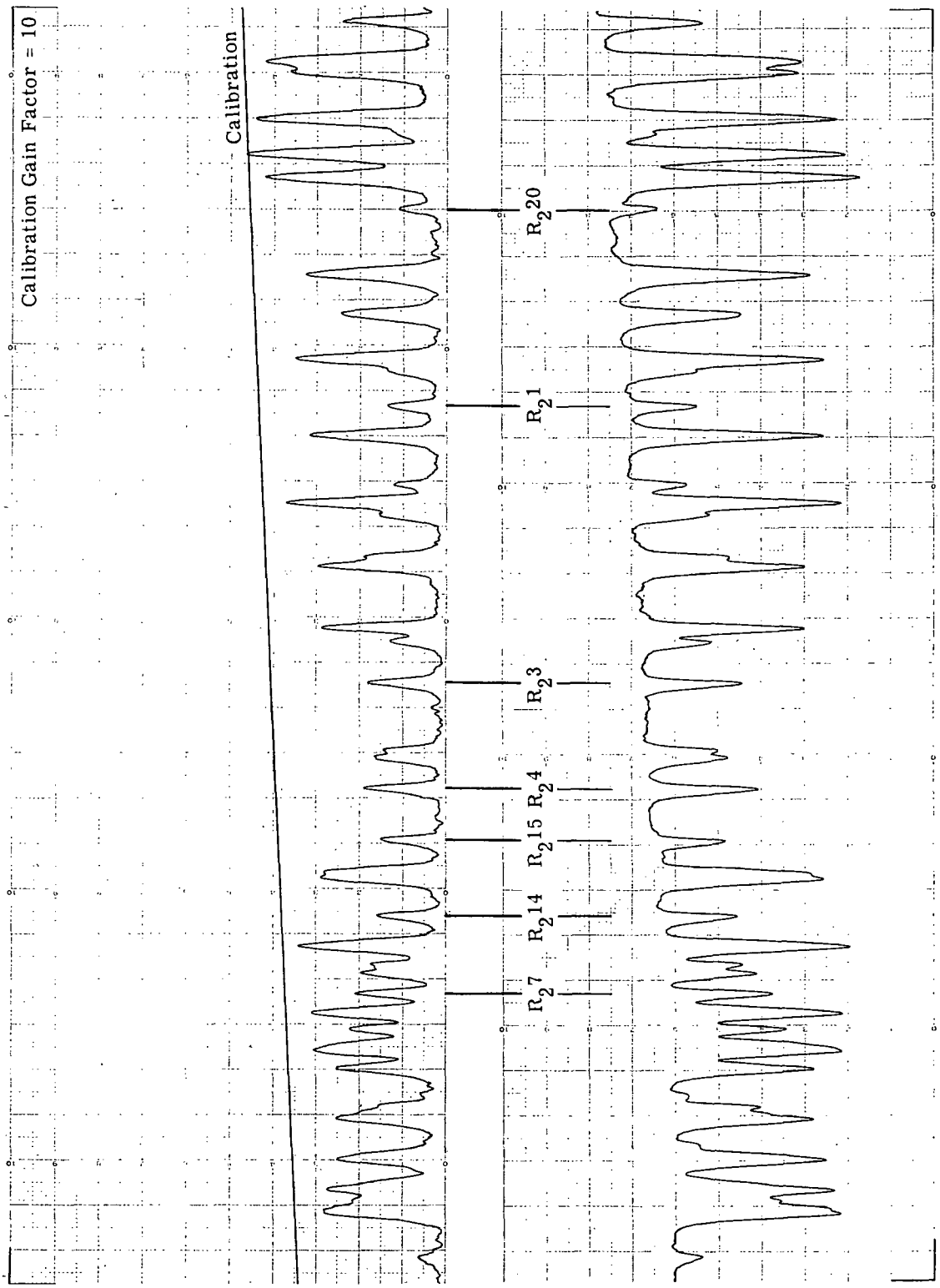

FIGURE 39. ULTRAVIOLET SPECTRA, PROFILE D: TRIANGULAR (COLD CENTER)

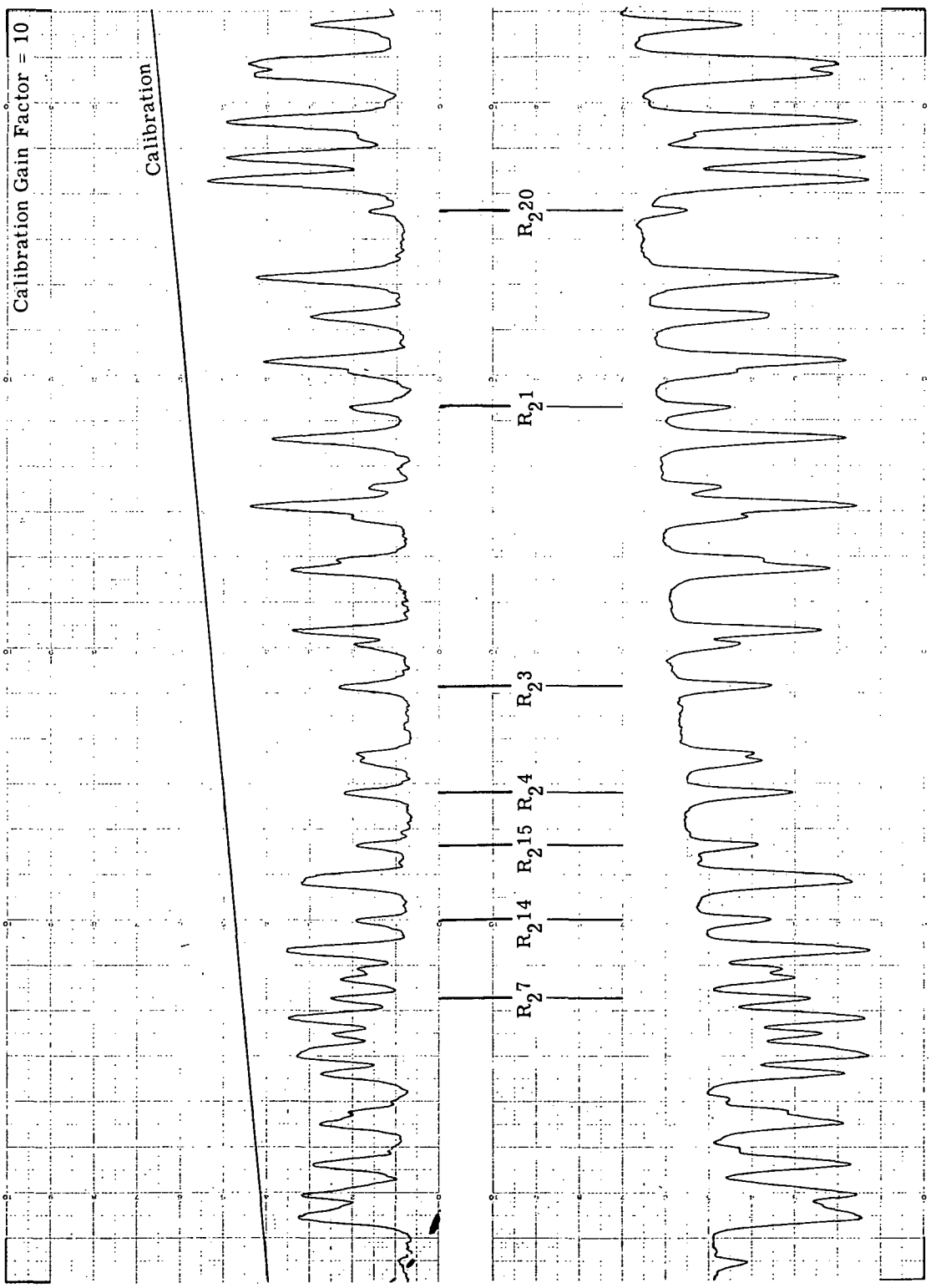

FIGURE 40. ULTRAVIOLET SPECTRA, PROFILE E: ISOTHERMAL

REFERENCES

1. F. S. Simmons, H. Y. Yamada, and C. B. Arnold, Measurement of Temperature Profiles in Hot Gases by Emission-Absorption Spectroscopy, NASA CR-72491, April 1969.

2. F. S. Simmons, "Band Models for Nonisothermal Radiating Gases," Appl. Opt., Vol. 5, p. 1801; Vol. 6, 1967, p. 1423.

3. A. Goldman, "On Simple Approximations to the Equivalent Width of a Lorentz Line," J. Quant. Spectros. Rad. Transf., Vol. 8, 1968, p. 829.

4. C. B. Ludwig, et.al., Study on Exhaust Plume Radiation Predictions, NASA CR-61233, 1968; see also GD/Convair Reports, DBE66-017, -001a, 1966.

5. F. S. Simmons, "Radiances and Equivalent Widths of Lorentz Lines for Non-isothermal Paths," J. Quant. Spectros. Rad. Transf., Vol. 7, 1967, p. 111.

6. G. H. Dieke and H. M. Crosswhite, "The Ultraviolet Bands of OH," J. Quant., Spectros. Rad. Transf., Vol. 2, 1962, p. 97.

7. D. M. Golden, et. al., "Experimental Oscillator Strength of OH, $^2\Sigma^+ \rightarrow {}^2\pi$ by a Chemical Method," J. Chem. Phys., Vol. 39, 1963, p. 3034.

8. R. C. M. Learner, "The Influence of Vibration-Rotation Interaction on Intensities in the Electronic Spectra of Diatomic Molecules," Proc. Roy. Soc., Vol. A 269, 1962, p. 311.

9. M. Nadler and W. E. Kaskan, "Collisional Broadening of OH $^2\Sigma^+ \rightarrow {}^2\pi$ Lines in Flames," J. Quant. Spectros. Rad. Transf., Vol. 10, 1970, p. 25.

10. H. Y. Yamada, "Total Radiances and Equivalent Widths of Isolated Spectral Lines with Combined Doppler and Collision-Broadened Profiles," J. Quant. Spectros. Rad. Transf., Vol. 8, 1968, p. 1463.

11. F. S. Simmons, "Infrared Spectroscopic Study of Hydrogen Fluorine Flames," AIAA J., Vol. 5, 1967, p. 778.

12. F. S. Simmons, "Spectroscopic Pyrometry of Gases, Flames and Plasmas," ISA Trans., Vol. 2, 1963, p. 168.

13. H. Kostkowski and H. P. Broida, "Spectral Absorption Method for Determining Population Temperatures in Hot Gases," JOSA, Vol. 46, 1956, p. 246.

14. W. G. Zinman and S. I. Bogdan, "Influence of Vibration-Rotation Temperature Determined from an Electronic OH Transition," Journ. of Chem. Phys., 40, 1964, p. 588.

15. P. J. Th. Zeegers and C. Th. J. Alkemade, "Chemiluminescence of OH Radicals and K. Atoms by Radical Recombination of Flames," Tenth Symposium (International) on Combustion, p. 21, The Combustion Institute, 1965.

16. E. C. Hinck, T. F. Seamans, M. Vanpee, and H. G. Wolfhard, "The Nature of OH Radiation in Low Pressure Flames," Tenth Symposium (International) on Combustion, p. 21, The Combustion Institute, 1965.

17. W. E. Kaskan, "Hydroxyl Concentrations in Rich Hydrogen-Air Flames Held on a Porous Burner," Combustion of Flame, 2, 1958, p. 229.

18. W. E. Kaskan, "Abnormal Excitation of OH in $H_2/O_2/N_2$ Flames," Journ. Chem. Phys., 31, 1959, p. 944.

19. W. L. Smith, "Iterative Solution of the Radiative Transfer Equation for the Temperature and Absorbing Gas Profile of an Atmosphere," Appl. Opt., Vol. 9, 1970, p. 1993.

20. S. Gordon and B. J. McBride, "Computer Program for Calculation of Complex Chemical Equilibrium Compositions, Rocket Performance, Incident and Reflected Shocks, and Chapman-Jouguet Detonations," NASA-SP-273, 1971.

21. R. M. Goody, Atmospheric Radiation. I: Theoretical Basis, Oxford Calander Press, 1964.

22. S. R. Drayson, "Atmospheric Transmission in the CO_2 Bands Between 12 μ and 18 μ," Appl. Opt., Vol. 5, 1966, p. 385.

23. A. C. Codgley, "Radiative Transport of Lorentz Lines in Nonisothermal Gases," J. Quant. Spectros. Rad. Transf., Vol. 10, 1970, p. 1065.

24. S. S. Penner, Quantitation Molecular Spectroscopy and Gas Emissivities, Addison-Wesley, Reading, 1959.

25. F. S. Simmons, Infrared Spectroscopic Study of Hydrogen-Fluorine Flames, II: Analytical Procedures, Report No. 4613-123-T, Willow Run Laboratories of the Institute of Science and Technology, The University of Michigan, Ann Arbor, March 1966.

26. C. D. Walshaw and C. D. Rodgers, "The Effect of the Curtis-Godson Approximation on the Accuracy of Radiative Heating Rate Calculation," Roy. Met. Soc. Quart. J., Vol. 89, 1963, p. 122.

27. A. G. Gaydon and H. G. Wolfhard, Flames, Their Structure, Radiation and Temperature, Chapman and Hall, Ltd., London, 1960, p. 295.

28. S. I. Pai, Fluid Dynamics of Jets, Van Nostrand Co., New York, 1954.

29. D. Anding, Band-Model Methods for Atmospheric Slant-Path Molecular Absorption, Report No. 7142-21-T, Willow Run Laboratories of the Institute of Science and Technology, The University of Michigan, Ann Arbor, February 1967.

DISTRIBUTION LIST

Addressee

NASA Lewis Research Center
21000 Brookpark Road
Cleveland, Ohio 44135
ATTN: Report Central Office
MS 5-5 (1)

NASA Lewis Research Center
21000 Brookpark Road
Cleveland, Ohio 44135
ATTN: Technology Utilization Office
MS 3-19 (1)

NASA Lewis Research Center
21000 Brookpark Road
Cleveland, Ohio 44135
ATTN: Library
MS 60-3 (2)

NASA Lewis Research Center
21000 Brookpark Road
Cleveland, Ohio 44135
ATTN: Fluid Systems Components
Division MS 5-3 (1)

NASA Lewis Research Center
21000 Brookpark Road
Cleveland, Ohio 44135
ATTN: W. L. Stewart
MS 77-2 (1)

NASA Lewis Research Center
21000 Brookpark Road
Cleveland, Ohio 44135
ATTN: J. Howard Childs
MS 60-4 (1)

NASA Lewis Research Center
21000 Brookpark Road
Cleveland, Ohio 44135
ATTN: H. Ellerbrock
MS 60-4 (1)

Addressee

NASA Lewis Research Center
21000 Brookpark Road
Cleveland, Ohio 44135
ATTN: Robert R. Hibbard
MS 302-1 (1)

NASA Scientific and Technical Information Facility
P. O. Box 33
College Park, Maryland 20740
ATTN: NASA Representative
RQT-2448 (6)

FAA Headquarters
800 Independence Avenue, S. W.
Washington, D. C. 20553
ATTN: Brigadier General
J. C. Maxwell (1)

FAA Headquarters
800 Independence Avenue, S. W.
Washington, D. C. 20553
ATTN: F. B. Howard/ SS120 (1)

NASA Headquarters
600 Independence Avenue, S. W.
Washington, D. C. 20546
ATTN: N. F. Rekos (RAP) (1)

Department of the Army
U. S. Army Aviation Material Laboratory
Fort Eustis, Virginia 23604
ATTN: John White (1)

Headquarters
Wright-Patterson AFB, Ohio 45433
ATTN: J. L. Wilkins SESOS (2)

Addressee

AFAPL (APTC)
Wright-Patterson AFB, Ohio 45433
ATTN: Lt. D. H. Quick (1)

Air Force Office of Scientific Research
1400 Wilson Blvd.
Arlington, Virginia 22209
ATTN: SREP (1)

Defense Documentation Center (DDC)
Cameron Station
5010 Duke Street
Alexandria, Virginia 22314 (1)

Department of the Navy
Bureau of Naval Weapons
Washington, D. C. 20025
ATTN: Robert Brown RAPP14 (1)

Department of the Navy
Bureau of Ships
Washington, D. C. 20360
ATTN: G. L. Graves (1)

NASA-Langley Research Center
Langley Station
Technical Library
Hampton, Virginia 23365
ATTN: Mark R. Nichols (1)

NASA-Langley Research Center
Langley Station
Technical Library
Hampton, Virginia 23365
ATTN: John V. Becker (1)

United States Air Force
Aero Propulsion Laboratory
Building 18D, Room 119
Wright-Patterson AFB, Ohio 45433
ATTN: Robert E. Henderson (1)

Addressee

United States Air Force
Cambridge Research Center
Electronics Research Center
L. G. Hanscom Field
Bedford, Massachusetts 01730
ATTN: Library (1)

United Aircraft Corporation
Pratt and Whitney Aircraft
400 Main Street
East Hartford, Connecticut 06108
ATTN: G. Andreini (2)

United Aircraft Corporation
Pratt and Whitney Aircraft Division
400 Main Street
East Hartford, Connecticut 06108
ATTN: Library (1)

United Aircraft Research
East Hartford, Connecticut 06027
ATTN: Library (1)

Allison Division of GMC
Department 8894, Plant 8
P. O. Box 894
Indianapolis, Indiana 46206
ATTN: J. N. Barney (1)

Allison Division of GMC
Department 8894, Plant 8
P. O. Box 894
Indianapolis, Indiana 46206
ATTN: G. E. Holbrook (1)

Allison Division of GMC
Department 8894, Plant 8
P. O. Box 894
Indianapolis, Indiana 46206
ATTN: Library (1)

Addressee

Northern Research and Eng. Corp.
219 Vassar Street
Cambridge, Massachusetts 02139
ATTN: K. Ginwala (1)

General Electric Company
Flight Propulsion Division
Cincinnati, Ohio 45215
ATTN: J. W. McBride H-44 (1)

General Electric Company
Flight Propulsion Division
Cincinnati, Ohio 45215
ATTN: C. Danforth H-32 (1)

General Electric Company
Flight Propulsion Division
Cincinnati, Ohio 45215
ATTN: Technical Inf. Center
N-32 (1)

General Electric Company
1000 Western Avenue
West Lynn, Massachusetts 01905
ATTN: Dr. C. W. Smith Library
Bldg. 2-40M (1)

Curtiss-Wright Corporation
Wright Aeronautical Division
Wood-Ridge, New Jersey 07075
ATTN: S. Lombardo (1)

Curtiss-Wright Corporation
Wright Aeronautical Division
Wood-Ridge, New Jersey 07075
ATTN: G. Provenzale (1)

Air Research Manufacturing Co.
402 South 36th Street
Phoenix, Arizona 85034
ATTN: Robert O. Bullock (1)

Addressee

Air Research Manufacturing Company
9851 Sepulveda Blvd.
Los Angeles, California 90009
ATTN: Dr. N. Van Le (1)

AVCO Corporation
Lycoming Division
550 South Main Street
Stratford, Connecticut 06497
ATTN: Claus W. Bolton (1)

AVCO Corporation
Lycoming Division
550 South Main Street
Stratford, Connecticut 06497
ATTN: Charles Kuintzle (1)

International Harvester Company
Solar Division
2200 Pacific Highway
San Diego, California 92112
ATTN: P. A. Pitt (1)

International Harvester Company
Solar Division
2200 Pacific Highway
San Diego, California 92112
ATTN: Mrs. L. Walper (1)

George Derderian AIR 53622 B
Department of the Navy
Bureau of Navy
Washington, D. C. 20360 (1)

The Boeing Company
Missile and Information Systems Div.
224 N. Wilkinson Street
Dayton, Ohio 45402
ATTN: Warren K. Thorson (1)

Addressee

North American Rockwell Corp.
Rocketdyne Division
Canoga Park, California 91305
ATTN: W. Herget (1)

The Southwest Center for Advanced Studies
P. O. Box 30365
Dallas, Texas 75230
ATTN: Gilbert N. Plass (1)

Aerojet-General Corporation
Sacramento, California 95809
ATTN : M. S. Nylin (1)

Aerojet-General Corporation
Sacramento, California 95809
ATTN: Library (1)

New England Materials Lab., Inc.
35 Commerical Street
Medford, Massachusetts 02155
ATTN: Allan S. Bufferd (1)

Cornell Aeronautical Laboratory
4455 Genesee Street
Buffalo, New York 14204 (1)

Marquardt Corporation
16555 Saticoy Street
Van Nuys, California 91406 (1)

Thompson Ramo Wooldridge
7209 Platt Avenue
Cleveland, Ohio 44104 (1)

ARO, Incorporated
Arnold Air Force Station,
Tennessee 37389 (1)

S. C. Fiorello
Aeronautical Engine Laboratory
Naval Air Engineering Center
Philadelphia, Pa. 19112 (1)

Addressee

Aerospace Research Laboratory
Wright-Patterson AFB, Ohio 45433
ATTN: Dr. R. G. Dunn (1)

NASA-MSFC
Aero-Astrodynamics Laboratory
Huntsville, Alabama 35812
ATTN: Werner K. Dahm (1)

General Dynamics/Convair
Space Science Laboratory
San Diego, California 92112
ATTN: C. B. Ludwig (1)

Barnes Engineering Company
30 Commerce Road
Stamford, Connecticut 06904
ATTN: Mrs. Belle B. Shipe (1)

University of Massachusetts
School of Engineering
Amherst, Ma. 01002
ATTN: Dr. H. C. Mongia (1)

Purdue University
School of Mechanical Eng.
Lafayette, Indiana 47907
ATTN: Mr. R. Viskanta (1)

Lothar Klein
287 Schenk Avenue
Great Neck, New York 11021 (1)

Teledyne, CAE
1330 Laskey Road
Toledo, Ohio 43601
ATTN: Technology Information Ctr. (1)

Washington State University
College of Engineering
Research Division
Pullman, Washington 99163
ATTN: D. Pratt (1)

Addressee

Fluidyne Engineering Corporation
5900 Olson
Memorial Highway
Minneapolis, Minnesota 55422
ATTN: J. Frame (1)

The University of Tennessee
Space Institute
Tullahoma, Tennessee 37388
ATTN: Dr. G. W. Braun (1)

NASA-Lewis Research Center
21000 Brookpark Road
Cleveland, Ohio 44135
ATTN: Donald Buchele
MS 77-1 (30)